

خدمات أكاديمية

كفاءات وطنية

معايير عالمية

دراسة  
للإستشارات والدراسات والترجمة

UNIVERSITY

drasah 1 | 00966555026526

00966560972772

www.drasah.com | info@drasah.com

# خدماتنا



توفير المراجع العربية والأجنبية



التحليل الاحصائي وتفسير النتائج

الاستشارات الأكاديمية



جمع المادة العلمية

الترجمة المعتمدة



 drasah1

 Info@drasah.com

 00966555026526

 00966560972772

 drasah.com



# دراسة

للاستشارات والدراسات والترجمة



تواصل معنا



00966555026526

00966560972772



متواجدون على مدار الساعة



**Investigation of Cationic-based Gemini Surfactants at Air-Water and  
Air-Solid Interfaces**

**By**

**Ahmad Sami Suleiman Abo-shunnar**

**Supervisor**

**Ala'a Fakhri Eftaiha**

**Associate Professor**

**Co-supervisor**

**Abdussalam Kayed Qaroush**

**Associate Professor**

**Submitted in Partial Fulfillment of the Requirements for the master's  
degree in Chemistry**

**Faculty of Graduate Studies**

**The Hashemite University**

**Zarqa-Jordan**

**August 4<sup>th</sup>, 2022**

## Abstract

### Investigation of Cationic-based Gemini Surfactants at Air-Water and Air-Solid Interfaces

By

**Ahmad Sami Suleiman Abo shunnar**

**Supervisor**

**Ala'a Fakhri Eftaiha**

**Associate Professor**

**Co-supervisor**

**Abdussalam Kayed Qaroush**

**Associate Professor**

Surfactants are renowned for being the main component of various commercial products. The increasing consumption of those products raised a worldwide concern about their environment impact and made exploiting more ecofriendly materials with superior performance a desire for a wide range of chemical, pharmaceutical and food industries.

In this research area, a lot of attention has been paid to ammonium and imidazolium based gemini surfactants (GSs) in the bulk solution and at the interface. On the contrary, further studies are needed to understand pyridinium based GSs at the air-water or air-solid interfaces. In this master thesis, we synthesized, identified and investigated the interfacial properties of nicotinic acid-based GS and their imidazolium counterpart experimentally and theoretically.

Our results showed that the stability of nicotinic acid based conventional surfactant monolayers was dependent on the head group charge as demonstrated by the  $\pi$ -A isotherm measurements, where the maximum surface pressure was decreased from *ca.* 35 mN/m in the case of the nicotinate ester to 2 mN/m once compared with the pyridinium correspondent. The corresponding GSs monolayers were stable with maximum surface pressure values to  $\sim$  58 mN/m. Moreover, imidazolium based GSs resulted in a more expanded film. The morphology of the surfactants films measured at air-water and air-solid interfaces indicated that the spacer identity played a crucial role in surfactant self-assembly, where the three lobed structures in the case of the ethylene spacer were turned into more complex domains for the *p*-xylylene based GS.

The miscibility of the nicotinate ester and the corresponding GS with palmitic acid (PA) were evaluated using excess Gibbs free energy of mixing. The PA was miscible with nicotinate over all composition with slight positive energy values, while the PA/GS mixtures showed large positive excess energy values. These results were supported by density functional theory calculations.

## الملخص

دراسة توائم مركبات الاملاح الموجبة ذات الفعالية السطحية على الواجهات المائية والصلبة

إعداد

أحمد سامي سليمان ابو شنار

المشرف

علاء فخري أفتيحة

أستاذ مشارك

المشرف المشارك

عبد السلام كايد قرعوش

أستاذ مشارك

تشتهر المواد ذات النشاط السطحي بكونها المكون الرئيسي للعديد من المنتجات التجارية. حيث ان الاستهلاك المتزايد لهذه المواد شكل اهتماماً واسعاً بسبب الأثر البيئي، مما يجعل اللجوء لمواد صديقة للبيئة ذات فاعلية متفوقة مرغوباً فيه، لاستخدامها في مجالات واسعة مثل الصناعات الكيميائية والصيدلانية والغذائية.

وفي مجال البحث العلمي، فقد تم إيلاء الكثير من الاهتمام لتوائم المواد ذات النشاط السطحي المكونة من الأمين والإيميدازول موجب الشحنة سواء في المحاليل أو على الواجهات السطحية. ومع ذلك، فما زال هناك حاجة إلى اجراء مزيد من الدراسات لفهم المركبات القائمة على البيريدين موجب الشحنة على واجهتي الهواء-الماء وكذلك الهواء-الصلب. في هذه الأطروحة، قمنا بتصنيع توائم المركبات ذات النشاط السطحي القائمة على حمض النيكوتينيك ونظيرتها من الإيميدازول موجب الشحنة والتحقق منها، ودراسة خصائصها السطحية تجريبياً ونظرياً.

لقد اظهرت قياسات الضغط السطحي مع المساحة عند ثبات درجة الحرارة أن استقرار الطبقة الأحادية للمواد ذات النشاط السطحي المكونة من حمض النيكوتينيك تعتمد على شحنة المجموعة الرأسية، حيث ان القيمة القصوى للضغط السطحي انخفضت من قرابة 35 م ن/م في حالة الاستير نيكوتينيت إلى حوالي 2 م ن/م لمركب البيريدين المشحون، وعلى النقيض من ذلك، اظهرت توائم المركبات استقرار الطبقات الأحادية خاصتها وبقيم ضغط سطحي تصل الى 58 م ن/م، علما ان توائم المركبات المكونة من الإيميدازول المشحون اظهرت تكوين طبقات ذات مساحة كبيرة. اما بخصوص طبوغرافية أفلام المواد اعلاه، فقد تم فحصها على الواجهات المائية والصلبة المقابلة للهواء، واطهرت النتائج أن طبيعة الفاصل تؤثر بشكل كبير في الترتيب التلقائي، حيث كون المركب المحتوي على الإيثيلين اشكالا من ثلاث حلقات تطورت الى اشكال أكثر تعقيدا في حالة البارازيلينين.

تم تقييم مدى امتزاج استر النيكوتين وتوائم المواد مع زيت النخيل الحمضي باستخدام الطاقة الحرة الزائدة لجيبس، وأظهرت النتائج أن مكونات الخليط الأول قابل للامتزاج مع انحراف إيجابي طفيف لقيم الطاقة، في حين اشارت قيم الطاقة الموجبة الى عدم امتزاج لزيت النخيل الحمضي وتقوم المركب المقابل. وقد دعمت هذه النتائج باستخدام حسابات نظرية الكثافة الوظيفية.

## Table of Contents

Examination Committee .....	II
Authorization .....	III
Dedication .....	IV
Acknowledgment .....	V
List of Symbols and Abbreviations.....	VI
List of Figures .....	IX
List of Schemes.....	XII
Abstract.....	XIV
Chapter 1 .....	1
1.1 Surfactants.....	1
1.2 Pyridinium-based GSs.....	3
1.3 Imidazolium-based GSs .....	7
1.4 Insoluble Surfactant Monolayers .....	9
1.5 Langmuir and Langmuir-Blodgett Trough.....	11
1.6 Brewster Angle Microscopy (BAM).....	11
1.7 Atomic Force Microscopy (AFM) .....	12
1.8 Research Objectives .....	13
Chapter 2.....	15
2.1 Nicotinic acid-Based CS/GS .....	15
2.1.1 Activation of Nicotinic Acid (NA, <b>1</b> ) .....	17
2.1.2 Synthesis of Hexadecyl Nicotinate (NA-C <sub>16</sub> , <b>4</b> ).....	18
2.1.3 Synthesis of 1-ethyl-3-((hexadecyloxy)carbonyl)pyridin-1-ium bromide (Et-NA <sup>+</sup> -C <sub>16</sub> •Br, <b>7</b> ) .....	21
2.1.4 Synthesis of 1,1'-(ethane-1,2-diyl)bis(3-((hexadecyloxy)carbonyl)pyridin-1-ium) bromide (S <sub>E</sub> (NA <sup>+</sup> -C <sub>16</sub> ) <sub>2</sub> •2Br, <b>8</b> ) .....	23
2.1.5 Synthesis of 1,1'-(butane-1,4-diyl)bis(3-((hexadecyloxy)carbonyl)pyridin-1-ium) bromide (S <sub>B</sub> (NA <sup>+</sup> -C <sub>16</sub> ) <sub>2</sub> •2Br, <b>11</b> ) .....	26
2.1.6 Synthesis of 1,1'-(1,4-phenylenebis(methylene))bis(3-((hexadecyloxy)carbonyl) pyridin-1-ium) bromide (S <sub>X</sub> (NA <sup>+</sup> -C <sub>16</sub> ) <sub>2</sub> •2Br, <b>12</b> ) .....	29
2.2 Imidazolium-based Surfactants .....	32

2.2.1 Synthesis of 1-Hexadecylimidazole ( <b>14</b> ).....	32
2.2.2 Synthesis of 3,3'-(ethane-1,2-diyl)bis(1-hexadecyl-imidazol-3-ium) bromide ( <b>S<sub>E</sub>(Im<sup>+</sup>-C16)<sub>2</sub>•2Br, 15</b> ) .....	35
2.2.3 Synthesis of 3,3'-(butane-1,4-diyl)bis(1-hexadecyl-imidazol-3-ium) bromide ( <b>S<sub>B</sub>(Im<sup>+</sup>-C16)<sub>2</sub>•2Br, 16</b> ) .....	39
2.2.4 Synthesis of 3,3'-(1,4-phenylenebis(methylene)) bis (1-hexadecyl-imidazole-3-ium-bromidee) ( <b>S<sub>X</sub>(Im<sup>+</sup>-C16)<sub>2</sub>•2Br, 17</b> ) .....	41
2.3 Instruments.....	44
2.4 Chemicals.....	44
Chapter 3.....	45
3.1 Abstract .....	45
3.2 Introduction .....	45
3.3 Results and Discussion.....	48
3.4 Experimental .....	60
3.4.1 Chemicals.....	60
3.4.2 $\pi$ -A isotherm measurements and LB film depositions.....	61
3.4.3 BAM measurements.....	61
3.4.4 AFM measurements.....	61
3.4.5 CMC measurements.....	62
3.5 Conclusion.....	62
3.6 Acknowledgment .....	62
Chapter 4.....	63
References.....	64
Appendix.....	77
الملخص.....	81

## List of Figures

<b>Figure 2.1.</b> ATR-FTIR spectra of <b>1</b> (blue trace), and <b>2</b> (black trace). .....	17
<b>Figure 2.2.</b> <sup>1</sup> H NMR spectra of <b>1</b> (black trace, <b>S</b> <sub>1</sub> : solvent = DMSO- <i>d</i> <sub>6</sub> ), <b>2</b> ( blue trace, <b>S</b> <sub>2</sub> : solvent = D <sub>2</sub> O). .....	18
<b>Figure 2.3.</b> ATR-FTIR spectra of <b>2</b> (blue trace), and <b>4</b> (black trace). .....	19
<b>Figure 2.4.</b> <sup>1</sup> H NMR spectra of <b>2</b> (green trace, <b>S</b> <sub>1</sub> : solvent = D <sub>2</sub> O), <b>3</b> (red trace) and <b>4</b> (black trace, <b>S</b> <sub>2</sub> : solvent = CDCl <sub>3</sub> ).....	20
<b>Figure 2.5.</b> <sup>13</sup> C NMR spectra of <b>2</b> (green trace, in = D <sub>2</sub> O), <b>3</b> (red trace) and <b>4</b> (black trace, <b>S</b> : solvent = CDCl <sub>3</sub> ).....	20
<b>Figure S2.6.</b> ATR-FTIR spectra of the surfactants <b>4</b> (blue trace), and <b>7</b> (black trace).....	22
<b>Figure S2.7.</b> <sup>1</sup> H NMR spectra of <b>4</b> (green trace), <b>5</b> (red trace) and <b>7</b> (black trace), <b>S</b> : solvent = CDCl <sub>3</sub> , <b>X</b> = ACN.....	22
<b>Figure S2.8.</b> <sup>13</sup> C NMR spectra of <b>4</b> (green trace), <b>5</b> (red trace) and <b>7</b> (black trace), <b>S</b> : solvent = CDCl <sub>3</sub> . .....	23
<b>Figure 2.9.</b> ATR-FTIR spectra of <b>4</b> (blue trace), and <b>8</b> (black trace) .....	24
<b>Figure 2.10.</b> <sup>1</sup> H NMR spectra of <b>4</b> (green trace), <b>6</b> (red trace, <b>S</b> <sub>1</sub> : solvent = CDCl <sub>3</sub> ) and <b>8</b> (black trace, <b>S</b> <sub>1</sub> : solvent = CDCl <sub>3</sub> , <b>S</b> <sub>2</sub> : solvent = EtOD, 3:2 (v/v) <b>X</b> = Et <sub>2</sub> O) .....	25
<b>Figure 2.11.</b> <sup>13</sup> C NMR spectra of <b>4</b> (green trace), <b>6</b> (red trace, <b>S</b> <sub>1</sub> : solvent = CDCl <sub>3</sub> ) and <b>8</b> (black trace, <b>S</b> <sub>1</sub> : solvent = CDCl <sub>3</sub> , <b>S</b> <sub>2</sub> : solvent = EtOD, 3:2 (v/v)) .....	25
<b>Figure 2.12.</b> ATR-FTIR spectra of <b>4</b> (blue trace), and <b>11</b> (black trace). .....	27
<b>Figure 2.13.</b> <sup>1</sup> H NMR spectra of <b>4</b> (green trace), <b>9</b> (red trace) and <b>11</b> (black trace), <b>S</b> : solvent = CDCl <sub>3</sub> . .....	28
<b>Figure 2.14.</b> <sup>13</sup> C NMR spectra of <b>4</b> (green trace), <b>9</b> (red trace) and <b>11</b> (black trace), <b>S</b> : solvent = CDCl <sub>3</sub> . .....	28
<b>Figure 2.15.</b> ATR-FTIR spectra of <b>4</b> (blue trace), <b>12</b> (black trace). .....	30
<b>Figure 2.16.</b> <sup>1</sup> H NMR spectra of <b>4</b> (green trace), <b>10</b> (red trace) and <b>12</b> (black trace), <b>S</b> : solvent = CDCl <sub>3</sub> . .....	31
<b>Figure 2.17.</b> <sup>13</sup> C NMR spectra of <b>4</b> (green trace), <b>10</b> (red trace) and <b>12</b> (black trace), <b>S</b> : solvent = CDCl <sub>3</sub> . .....	31

<b>Figure 2.18.</b> ATR-FTIR spectra of <b>13</b> (blue trace), and <b>14</b> (black trace). .....	34
<b>Figure 2.19.</b> <sup>1</sup> H NMR spectra of <b>3</b> (green trace, in CDCl <sub>3</sub> ), <b>13</b> (red trace) and <b>14</b> (black trace), <b>S</b> = DMSO- <i>d</i> <sub>6</sub> , <b>X</b> =H <sub>2</sub> O.....	34
<b>Figure 2.20.</b> <sup>13</sup> C NMR spectra of <b>3</b> (green trace, <b>S</b> <sub>1</sub> = CDCl <sub>3</sub> ), <b>13</b> (red trace) and <b>14</b> (black trace), <b>S</b> <sub>2</sub> = DMSO- <i>d</i> <sub>6</sub> . .....	35
<b>Figure 2.21.</b> ATR-FTIR spectra of <b>14</b> (blue trace), and <b>15</b> (black trace). .....	37
<b>Figure 2.22.</b> <sup>1</sup> H NMR spectra of <b>6</b> (green trace, in CDCl <sub>3</sub> ), <b>14</b> (red trace, <b>S</b> = DMSO- <i>d</i> <sub>6</sub> , <b>X</b> = H <sub>2</sub> O), and <b>15</b> (black trace, in CDCl <sub>3</sub> ).....	37
<b>Figure 2.23.</b> <sup>13</sup> C NMR spectra of <b>6</b> (green trace, in CDCl <sub>3</sub> ), <b>14</b> (red trace, <b>S</b> = DMSO- <i>d</i> <sub>6</sub> ), and <b>15</b> (black trace, in CDCl <sub>3</sub> ).....	38
<b>Figure 2.24.</b> ATR-FTIR spectra of <b>14</b> (blue trace), and <b>16</b> (black trace). .....	40
<b>Figure 2.25.</b> <sup>1</sup> H NMR spectra of <b>9</b> (green trace, in CDCl <sub>3</sub> ), <b>14</b> (red trace), and <b>16</b> (black trace), <b>S</b> = DMSO- <i>d</i> <sub>6</sub> , <b>X</b> = H <sub>2</sub> O.....	40
<b>Figure 2.26.</b> <sup>13</sup> C NMR spectra of <b>9</b> (green trace, <b>S</b> <sub>1</sub> = CDCl <sub>3</sub> ), <b>14</b> (red trace), and <b>16</b> (black trace), <b>S</b> <sub>2</sub> = DMSO- <i>d</i> <sub>6</sub> .....	41
<b>Figure 2.27.</b> ATR-FTIR spectra of <b>14</b> (blue trace), and <b>17</b> (black trace). .....	42
<b>Figure 2.28.</b> <sup>1</sup> H NMR spectra of <b>10</b> (green trace, <b>S</b> <sub>1</sub> = CDCl <sub>3</sub> ), <b>14</b> (red trace, <b>S</b> <sub>2</sub> = DMSO- <i>d</i> <sub>6</sub> , <b>X</b> <sub>1</sub> = H <sub>2</sub> O), and <b>17</b> (black trace, <b>S</b> <sub>1</sub> = CDCl <sub>3</sub> , <b>X</b> <sub>2</sub> = ACN). .....	43
<b>Figure 2.29.</b> <sup>13</sup> C NMR spectra of <b>10</b> (green trace, <b>S</b> <sub>1</sub> = CDCl <sub>3</sub> ), <b>14</b> (red trace, <b>S</b> <sub>2</sub> = DMSO- <i>d</i> <sub>6</sub> ), and <b>17</b> (black trace, <b>S</b> <sub>1</sub> = CDCl <sub>3</sub> ).....	43
<b>Figure 3.1.</b> $\pi$ -A isotherms of conventional and gemini surfactants comprised of <b>A</b> . Nicotinate and <b>B</b> . Imidazolium head group(s). .....	51
<b>Figure 3.2.</b> $\pi$ -A isotherms of: <b>A</b> . PA/NA-C <sub>16</sub> ; <b>B</b> . PA/S <sub>x</sub> (NA <sup>+</sup> -C <sub>16</sub> ) <sub>2</sub> •2Br mixed monolayers measured on Milli-Q water subphase at 25 °C. The data including 2:1 and 1:2 mixtures are presented in Figure S34, Supporting Information.....	52
<b>Figure 3.3.</b> $\Delta G_{ex\pi}$ of binary mixtures comprised of: <b>A</b> . PA/NA-C <sub>16</sub> ; <b>B</b> . PA/S <sub>x</sub> (NA <sup>+</sup> -C <sub>16</sub> ) <sub>2</sub> •2Br measured as a function of monolayer composition at different surface pressure .....	54
<b>Figure 3.4.</b> DFT-optimized structures of <i>homo</i> - and <i>hetero</i> -pair (with hydrated head groups using PCM model) of: <b>A</b> . carboxylic acid, <b>B</b> . nicotinate ester, <b>C</b> . protonated nicotinate, <b>D</b> . S <sub>x</sub> (NA <sup>+</sup> -C <sub>2</sub> ) <sub>2</sub> , <b>E</b> . carboxylic acid: nicotinate ester, <b>F</b> . carboxylic acid: protonated nicotinate, <b>G</b> . carboxylic acid: S <sub>x</sub> (NA <sup>+</sup> -C <sub>2</sub> ) <sub>2</sub> . Interaction energy values in kcal mol <sup>-1</sup> are given below structures.....	55

<b>Figure 3.5.</b> BAM images (50 $\mu\text{m}$ x 50 $\mu\text{m}$ ) measured at $\pi = 7$ mN/m of: <b>A.</b> Et- $\text{NA}^+\text{-C}_{16}\cdot\text{Br}$ , <b>B.</b> NA- $\text{C}_{16}$ , <b>C.</b> $\text{S}_{\text{E}}(\text{NA}^+\text{-C}_{16})_2\cdot 2\text{Br}$ , <b>D.</b> $\text{S}_{\text{B}}(\text{NA}^+\text{-C}_{16})_2\cdot 2\text{Br}$ , <b>E-G.</b> $\text{S}_{\text{X}}(\text{NA}^+\text{-C}_{16})_2\cdot 2\text{Br}$ (The last two images were acquired at $\pi = 15$ and 24 mN/m, respectively) and <b>H.</b> PA.....	56
<b>Figure 3.6.</b> AFM height images measured at $\pi = 7$ mN/m of: <b>A.</b> Et- $\text{NA}^+\text{-C}_{16}\cdot\text{Br}$ , <b>B.</b> NA- $\text{C}_{16}$ , <b>C.</b> $\text{S}_{\text{E}}(\text{NA}^+\text{-C}_{16})_2\cdot 2\text{Br}$ , <b>D.</b> $\text{S}_{\text{B}}(\text{NA}^+\text{-C}_{16})_2\cdot 2\text{Br}$ ; <b>E.</b> $\text{S}_{\text{X}}(\text{NA}^+\text{-C}_{16})_2\cdot 2\text{Br}$ and <b>F.</b> PA. ....	58
<b>Figure 3.7.</b> BAM and the corresponding AFM images of: <b>A.</b> 3:1, <b>B.</b> 1:1, and <b>C.</b> 1:3 PA/(NA- $\text{C}_{16}$ ) mixed monolayers obtained at $\pi = 7$ mN/m.....	59
<b>Figure 3.8.</b> AFM height images and the corresponding BAM measured at $\pi = 7$ mN/m of: <b>A.</b> 3:1 PA/ $\text{S}_{\text{X}}(\text{NA}^+\text{-C}_{16})_2\cdot 2\text{Br}$ , <b>B.</b> 1:1 PA/ $\text{S}_{\text{X}}(\text{NA}^+\text{-C}_{16})_2\cdot 2\text{Br}$ , and <b>C.</b> 1:3 PA/ $\text{S}_{\text{X}}(\text{NA}^+\text{-C}_{16})_2\cdot 2\text{Br}$ . The estimated domain thickness relative to the pinhole defect is around 1.3 nm. ....	60
<b>Figure A.1.</b> Surface tension ( $\gamma$ , mN/m) versus $\log C$ of Et- $\text{NA}^+\text{-C}_{16}\cdot\text{Br}$ . The CMC was determined at the intersection of the linear regression fits. The applied concentrations were in the mM range. ....	77
<b>Figure A.2.</b> DFT-optimized structures (in the gas phase) of PA, NA and $\text{Im}^+$ -based conventional and gemini surfactants including molecular height, length ( $\text{\AA}$ ) and cross-sectional area ( $\text{\AA}^2$ ). ....	78
<b>Figure A.3.</b> Surface tension ( $\gamma$ , mN/m) versus $\log C$ of: <b>A.</b> $\text{Im}^+\text{-C}_{16}\cdot\text{Cl}$ , <b>B.</b> $\text{S}_{\text{E}}(\text{Im}^+\text{-C}_{16})_2\cdot 2\text{Br}$ , <b>C.</b> $\text{S}_{\text{B}}(\text{Im}^+\text{-C}_{16})_2\cdot 2\text{Br}$ and <b>D.</b> $\text{S}_{\text{X}}(\text{Im}^+\text{-C}_{16})_2\cdot 2\text{Br}$ . The CMC was determined at the intersection of the linear regression fits. The applied concentrations were in the mM range.....	79
<b>Figure A.4.</b> <b>A.</b> Isothermal compressibility plots of $\text{S}(\text{NA}^+\text{-C}_{16})_2\cdot 2\text{Br}$ , <b>B.</b> The isothermal compressional moduli of $\text{S}(\text{NA}^+\text{-C}_{16})_2\cdot 2\text{Br}$ as a function of surface pressure in comparison with DPPC.....	79
<b>Figure A.5.</b> $\pi$ -A isotherms of: <b>A.</b> PA/NA- $\text{C}_{16}$ ; <b>B.</b> PA/ $\text{S}_{\text{X}}(\text{NA}^+\text{-C}_{16})_2\cdot 2\text{Br}$ mixed monolayers measured on Milli-Q water subphase at 25 $^{\circ}\text{C}$ .....	80

### List of Schemes

<b>Scheme 1.1.</b> A schematic illustration of: <b>A.</b> Conventional surfactant (CS), <b>B.</b> Gemini surfactant (GS). The blue circle and the zigzag represent the head group, and the tail, respectively. ....	1
<b>Scheme 1.2.</b> The chemical structure of <b>A.</b> Polyoxymethylene (30)4-(1,1,3,3-tetramethyl butyl) phenyl ether (Triton X-305); <b>B.</b> Sodium p-dodecyl benzene sulfonate (SDBS); <b>C.</b> Cetyltrimethylammonium bromide (CTMAB) and <b>D.</b> Dipalmitoylphosphatidylcholine (DPPC). ....	2
<b>Scheme 1.3.</b> <b>A.</b> The chemical structure of pyridine; <b>B.</b> The orbital diagram of the pyridine nitrogen and <b>C.</b> Resonance contributors for pyridine. ....	4
<b>Scheme 1.4.</b> The chemical structure of selected pyridinium based GSs. <b>A.</b> 1,1'-dialkyl-4,4'-bispyridinium; <b>B.</b> 1,1'-dialkyl-4,4'-alkylenebispyridinium; <b>C.</b> 1,1'-dialkyl-2,2'-alkylenebispyridinium; <b>D.</b> 1,1'-((ethane-1,2-diylbis(sulfanediyl))bis(alkane-1,2-diyl))bis(pyridin-1-ium); <b>E.</b> 1,1'-alkylenebis(2-alkylpyridin-1-ium); <b>F.</b> 3,3'-((2,3-dihydroxysuccinyl)bis(azanediyl))bis(1-hexadecylpyridin-1-ium); <b>G.</b> 1,1'-(1,4-phenylenebis(methylene)) bis(3-stearamidopyridin-1-ium) or 1,1'-[poly(oxyethylene)]bis(3-stearamidopyridin-1-ium).....	5
<b>Scheme 1.5.</b> The chemical structure of: <b>A.</b> NA; <b>B.</b> NA-ester and <b>C.</b> Representative NA based GSs. ....	7
<b>Scheme 1.6.</b> The chemical structure of: <b>A.</b> Imidazole and <b>B.</b> Imidazolium cation and their resonance structures (Joule & Mills, 2010). ....	8
<b>Scheme 1.7.</b> The chemical structure of selected imidazolium GSs. <b>A.</b> 1,1'-(alkane-1,4-diyl)bis(3-alkyl-1H-imidazol-3-ium) and <b>B.</b> 3,3'-((alkane-1,5-diylbis(sulfanediyl))bis(alkane-2,1-diyl))bis(1-methyl-1H-imidazol-3-ium). ....	9
<b>Scheme 1.8.</b> A hypothetical $\pi$ -A isotherm that shows the most the characteristic features of an insoluble surfactant monolayer. $A$ ( $\text{\AA}^2/\text{molecule}$ ) is calculated using the following equation: $A_{\text{trough}}McNAV$ , where the trough area is in $\text{\AA}^2$ , $M$ is the surfactant molecular weight (g/mol), $c$ is concentration (g/L), $NA$ is Avogadro's number (molecule/mol) and $V$ is the spreading volume of solution (L) (Michael C. Petty, 1996). ....	10
<b>Scheme 1.9.</b> A graphical illustration of a Langmuir/LB trough. This Figure has been redrawn from the work of R. F. de Oliveira <i>et al.</i> (de Oliveira, de Barros, & Ferreira, 2017). ....	11
<b>Scheme 1.10.</b> An illustration of BAM principle. This Figure has been redrawn from the work of T. Kaercher <i>et al.</i> (Kaercher, Hönig, & Möbius, 1993) .....	12

<b>Scheme 1.11. A.</b> Schematic illustration of AFM, <b>B.</b> presentation of tip movement in contact and tapping mode. This Figure has been redrawn from the work of Bert Voigtländer (Voigtländer, 2019). .....	13
<b>Scheme 1.12.</b> The chemical structure of A. NA-ester; B. Quaternized NA-ester; C and D. The proposed architectures of NA and imidazolium GSs, respectively. ....	14
<b>Scheme 2.1.</b> Schematic representation for the synthesis of the ester-bonded, pyridine(ium)-based conventional; hexadecyl nicotinate (NA-C <sub>16</sub> , <b>4</b> ) and 1-ethyl-3-((hexadecyloxy)carbonyl)pyridin-1-ium bromide Et-(NA <sup>+</sup> -C <sub>16</sub> •Br, <b>7</b> ) as well as GSs; <b>SE</b> : Ethylene spacer ( <b>SE</b> (NA <sup>+</sup> -C <sub>16</sub> ) <sub>2</sub> •2Br, <b>8</b> ). <b>SB</b> : Butylene spacer( <b>SB</b> (NA <sup>+</sup> -C <sub>16</sub> ) <sub>2</sub> •2Br, <b>11</b> ). <b>SX</b> : Xylenylene spacer ( <b>SX</b> (NA <sup>+</sup> -C <sub>16</sub> ) <sub>2</sub> •2Br, <b>12</b> ). ....	16
<b>Scheme 2.2.</b> Deprotonation of NA ( <b>1</b> ) by KOH in MeOH. ....	17
<b>Scheme 2.3.</b> The synthesis of the nicotinate ester, NA-C <sub>16</sub> ( <b>4</b> ). ....	19
<b>Scheme 2.4.</b> The synthesis of the charged conventional surfactant, Et-NA <sup>+</sup> -C <sub>16</sub> •Br ( <b>7</b> ). ....	21
<b>Scheme S2.5.</b> The synthesis of the ethylene-based GS, <b>S<sub>E</sub></b> (NA <sup>+</sup> -C <sub>16</sub> ) <sub>2</sub> •2Br ( <b>8</b> ). ....	24
<b>Scheme 2.6.</b> The synthesis of butylene-based GS, <b>S<sub>B</sub></b> (NA <sup>+</sup> -C <sub>16</sub> ) <sub>2</sub> •2Br ( <b>11</b> ). ....	26
<b>Scheme 2.7.</b> The synthesis of p-xylenyl-based GS, <b>S<sub>X</sub></b> (NA <sup>+</sup> -C <sub>16</sub> ) <sub>2</sub> •2Br ( <b>12</b> ). ....	29
<b>Scheme 2.8.</b> Schematic representation for the synthesis of the imidazolium-based GSs; <b>SE</b> : Ethylene spacer ( <b>S<sub>E</sub></b> (Im <sup>+</sup> -C <sub>16</sub> ) <sub>2</sub> •2Br, <b>15</b> ). <b>SB</b> : Butylene spacer ( <b>S<sub>B</sub></b> (Im <sup>+</sup> -C <sub>16</sub> ) <sub>2</sub> •2Br, <b>16</b> ). <b>Sx</b> : Xylenylene spacer ( <b>S<sub>X</sub></b> (Im <sup>+</sup> -C <sub>16</sub> ) <sub>2</sub> •2Br, <b>17</b> ). ....	32
<b>Scheme 2.9.</b> The synthesis of 1-Hexadecylimidazole <b>14</b> . ....	33
<b>Scheme 2.10.</b> The synthesis of the ethylene-based GS, <b>S<sub>E</sub></b> (Im <sup>+</sup> -C <sub>16</sub> ) <sub>2</sub> •2Br ( <b>15</b> ). ....	36
<b>Scheme 2.11.</b> The synthesis of butylene-based GS, <b>S<sub>B</sub></b> (Im <sup>+</sup> -C <sub>16</sub> ) <sub>2</sub> •2Br ( <b>16</b> ). ....	39
<b>Scheme 2.12.</b> The synthesis of p-xylenylene-based GS, <b>S<sub>X</sub></b> (Im <sup>+</sup> -C <sub>16</sub> ) <sub>2</sub> •2Br ( <b>17</b> ). ....	42
<b>Scheme 3.1.</b> Schematic illustration of a positively charged GS. The physiochemical properties of these surfactants depend on the flexibility/rigidity of the spacer, the length of the tails and the chemical identity of the headgroups. ....	46
<b>Scheme 3.2.</b> The chemical structure of: <b>A.</b> Pyridine-3-carboxylic acid (Nicotinic acid, NA; R = -H)/Hexadecyl nicotinate (NA-C <sub>16</sub> ; R = -C <sub>16</sub> H <sub>33</sub> ), <b>B.</b> 1-ethyl-3-((hexadecyloxy)carbonyl)pyridin-1-ium bromide Et-NA <sup>+</sup> -C <sub>16</sub> •Br, <b>C.</b> 1,1'-(spacer)bis(3-((hexadecyloxy)carbonyl)pyridin-1-ium) bromide (S(NA <sup>+</sup> -C <sub>16</sub> ) <sub>2</sub> •2Br), <b>D.</b> 3,3'-(spacer)bis(1-hexadecyl-1H-imidazol-3-ium) bromide (S(Im <sup>+</sup> -C <sub>16</sub> ) <sub>2</sub> •2Br), <b>E.</b> 1-hexadecyl-3-methyl-1H-imidazol-3-ium chloride (Me-Im <sup>+</sup> -C <sub>16</sub> •Cl) and <b>F.</b> Palmitic acid (PA). ....	48

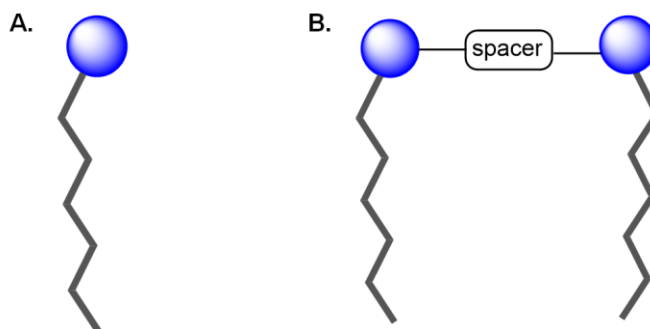
## Chapter 1

### Introduction

#### 1.1 Surfactants

**Surface Active Agents** or surfactants are molecules comprised of a hydrophilic head and a hydrophobic tail (**Scheme 1.1A**). This unique structure makes surfactants capable to reduce surface tension upon adsorption at interfaces, and to form sub-surface aggregates (Bengt Kronberg, 2014) (Fredric M. Menger, 2002).

Surface tension ( $\gamma$ ) represents the work associated with the creation of additional liquid surface to overcome cohesive interactions between bulk molecules. Thermodynamically, it is defined as the change in Gibbs free energy ( $G$ ) as a function of area ( $\sigma$ ) at constant temperature, pressure, and composition:  $(\partial G / \partial \sigma)_{T,P,N} = \gamma$ . Generally, surfactants tend to adsorb at the air-water interface, pointing out their hydrocarbon chains towards the vapor phase, thus reducing the surface free energy with increasing their concentration, which is ceased as surfactant form micelles at critical micellar concentration (CMC), where the hydrocarbon chains congregate inside aggregates and the polar head groups face the aqueous phase.



**Scheme 1.1.** A schematic illustration of: **A.** Conventional surfactant (CS), **B.** Gemini surfactant (GS). The blue circle and the zigzag represent the head group, and the tail, respectively.

Surfactants are classified into four types based on the head group chemical structure as **1)** non-ionic, with a polar head that is not electrically charged as alcohols (Lisunova, Lebovka, Melezhyk, & Boiko, 2006); **2)** anionic, such as sulfonates, phosphates, and carboxylates (Ma, Boyd, & Drummond, 2006); **3)** cationic like pyridinium and ammonium salts (Senthil Kumar & Chandrasekara Pillai, 2006); and **4)** zwitterionic, which contains negative and positive charges with a net zero formal charge, such as amino acids and

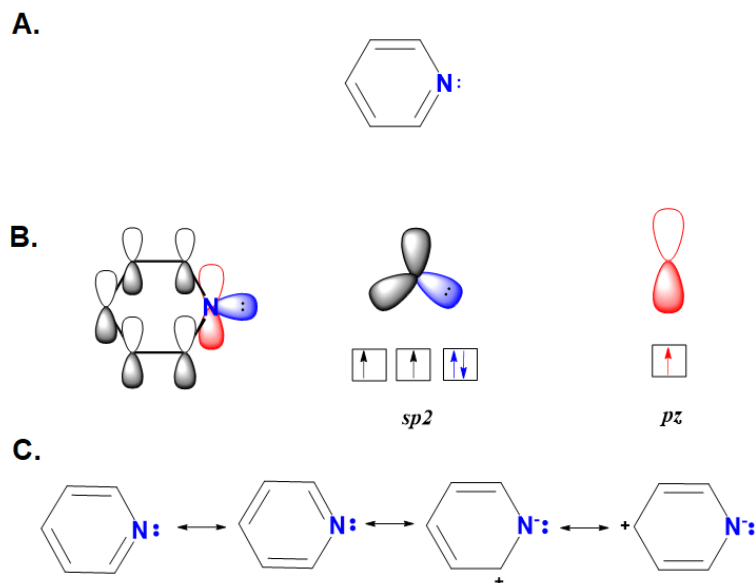


corresponding GS with two carbon spacer is 0.9 mM (Akbaş, Elemenli, & Boz, 2012). Historically, GSs were first reported in 1971 by Bunton group, where a series of bisquaternary ammonium bromides was used as micellar catalysts (Bunton, Robinson, Schaak, & Stam, 1971). Twenty years later, the physicochemical properties of cationic (quaternary ammonium) and anionic (anionic alkyl phosphate) GSs were investigated thoroughly (Menger & Littau, 1991). Following that, numerous studies were performed to compare the bulk and interfacial properties of GSs (Du, Lu, Li, Wang, & Yang, 2006; Yujie Wang, Marques, & Pereira, 2008; Aurora Pinazo, Pons, Bustelo, Manresa, Morán, Raluy, & Pérez, 2019).

## 1.2 Pyridinium-based GSs

Pyridine (1-azacyclohexa-1,3,5-triene (C<sub>5</sub>H<sub>5</sub>N), **Scheme 1.3A**), is a six-membered, heterocyclic aromatic compound, that is water-soluble, weakly alkaline, flammable, and colorless liquid, with an unpleasant odor, that boils at 115.5 °C (“Britannica Encyclopedia,” 2018). It is used as a solvent, and precursor to synthesize different anti-microbial agents (Patel & Agravat, 2009; Patel *et al.*, 2011). While it exists in different naturally occurring compounds such as niacin and pyridoxal (both known as B vitamins), it is obtained industrially by the reaction of acetaldehyde and ammonia.

As shown in **Scheme 1.3B**, the *sp*<sup>2</sup> hybridized pyridine nitrogen is engaged in two  $\sigma$ -bonds with the neighboring carbons and a  $\pi$ -bond through the electron in the unhybridized *p* orbital. The electron pair in third *sp*<sup>2</sup> orbital does not contribute to the aromatic system and lies closer to the nucleus once compared with an electron pair occupies *sp*<sup>3</sup> orbital, which makes it a weaker base than alkylamines. For example, the *pK*<sub>b</sub> of pyridine and piperidine are 8.75 and 2.88, respectively (Kum-Tatt, 1958). The chemical structure of pyridine and its resonance are presented in **Scheme 1.3**.

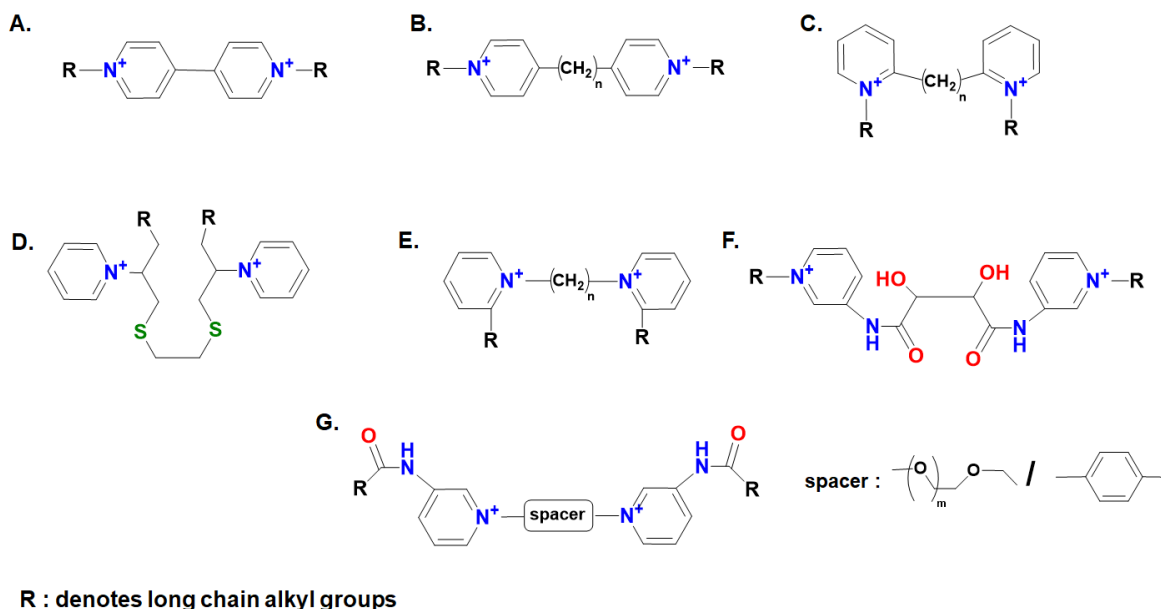


**Scheme 1.3.** **A.** The chemical structure of pyridine; **B.** The orbital diagram of the pyridine nitrogen and **C.** Resonance contributors for pyridine.

1,1'-dialkyl-4,4'-bispyridinium compounds (known as dialkylviologens, **Scheme 1.4A**) are prominent examples of pyridinium based GSs that were investigated extensively for mediating redox reactions, without exploring surface activity and self-aggregation properties (Thompson, Barrette, & Hurst, 1987; Vermeulen & Thompson, 1992; D. K. Lee, Kim, Kwon, Kang, & Kevan, 1997a), until Quagliotto group reported on the synthesizing of a series of 1,1'-dialkyl-4,4'-alkylenebispyridinium compounds and the corresponding 2,2'-series (**Scheme 1.4B-C**) using different spacers and counter ions. While the high Krafft points of the former ( $> 50\text{ }^{\circ}\text{C}$ ) limits their potential applications, the synthesis of the second series with alkylene linkers at the 2-position of the pyridine ring was challenging. The methanesulfonate salts of the latter have CMC values ranging between 2.07 and 0.75 mM going from ethylene into dodecylene spacer. Replacing  $\text{CH}_3\text{SO}_3^-$  with halides, decreased the CMC from 2.09 into 1.51 mM in the case of  $\text{Cl}^-$ , and raised the Krafft point up to  $27.9\text{ }^{\circ}\text{C}$  when  $\text{Br}^-$  was introduced. The CMC of the chloride salt was about half of the bromide correspondent (1.86 .vs. 0.837 mM) (Quagliotto, Viscardi, Barolo, Barni, Bellinvia, Fiscaro, & Compari, 2003). Tethering two pyridine rings with ethane-1,2-dithiol spacer (**Scheme 1.4D**) resulted in GSs with extremely low CMC down to 0.03 mM for the hexadecyl derivative, where the DNA binding capability increases with increasing the tail length. The structure property relationship of the thiolated surfactants were evaluated against 1,1'-dialkyl-2,2'-alkylenebispyridinium and 1,1'-

alkylenebis(2-alkylpyridin-1-ium) compounds (**Scheme 1.4C** and **E**, respectively) (Bhadani & Singh, 2009).

Water insoluble, amide bonded pyridinium GSs were synthesized by the reaction of tartaric acid and 3-aminopyridine, followed by quaternization reaction with 1-hexadecyl bromide (**Scheme 1.4F**). Although surface pressure-area ( $\pi$ - $A$ ) isotherms of the chiral and the meso compounds were similar, the former had more compressed film and comprised of two-dimensional crystalline aggregates as confirmed by Brewster angle microscopy (BAM). The formate salt of those surfactants are water soluble, and their aggregation was affected by the linker stereochemistry (Maximilian E. Franke & Rehage, 2019). The bromide salts of carboxy amide bonded pyridinium GSs with *p*-xylene and polyethylene glycol spacers (**Scheme 1.4G**) were synthesized and investigated in Langmuir monolayers. While the latter form a mesh-like network at the air-water interface, the use of the aromatic, rigid spacer resulted in a solid monolayer. Once again, the micellization behavior in aqueous medium was investigated upon replacing the bromide with formate anion. It was concluded that stronger counter anion binding and thus lower enthalpy of aggregation were associated with shorter length of polyethylene glycol (Maximilian Eberhard Franke & Rehage, 2022).

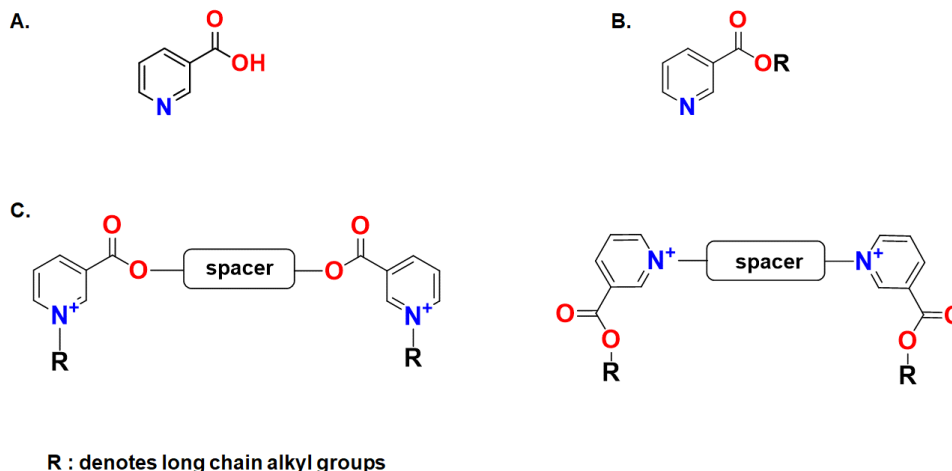


**Scheme 1.4.** The chemical structure of selected pyridinium based GSs. **A.** 1,1'-dialkyl-4,4'-bispyridinium; **B.** 1,1'-dialkyl-4,4'-alkylenebispyridinium; **C.** 1,1'-dialkyl-2,2'-alkylenebispyridinium; **D.** 1,1'-((ethane-1,2-diylbis(sulfanediy))bis(alkane-1,2-diyl))bis(pyridin-1-ium); **E.** 1,1'-alkylenebis(2-alkylpyridin-1-ium); **F.** 3,3'-((2,3-dihydroxysuccinyl)bis(azanediyl))bis(1-hexadecylpyridin-1-ium); **G.** 1,1'-(1,4-phenylenebis(methylene))bis(3-stearamidopyridin-1-ium) or 1,1'-[poly(oxyethylene)]bis(3-stearamidopyridin-1-ium).

As mentioned earlier, one of the naturally occurring pyridine derivatives is nicotinic acid (NA) (**Scheme 1.5A**), that is used for treating pellagra and reducing high cholesterol levels in the blood (“Britannica Encyclopedia,” 2017). NA-esters (or ester nicotines, **Scheme 1.5B**) have better pharmacokinetics in comparison with the parent molecule, including longer half-life and slower elimination rates, with enhanced solubility in hydrophobic media (Ojogun, Vyas, Lehmler, & Knutson, 2010). Lehmler *et al.* reported on the interaction between a series of NA-esters and DPPC in monolayer and bilayers. Analysis of the mixing thermodynamics suggested that DPPC-nicotinate binary mixtures were partially miscible at the air-water interface, while the NA-ester bearing a partially fluorinated stearyl side chain was immiscible with the phospholipid at the same conditions (Lehmler & Bummer, 2005; Lehmler, Fortis-Santiago, Nauduri, & Bummer, 2005a). Further studies have concluded that the more hydrophobic nicotinate ester, the better partitioning in the DPPC bilayer (Ojogun, Vyas, *et al.*, 2010).

Two strategies were reported for the synthesis of NA based GSs. Firstly, dimerization two ester nicotinate molecules *via* ester linkage and alkyl chains are bonded to the pyridinium nitrogen’s (**Scheme 1.5C**) or secondly, the two pyridinium ring are attached with a spacer through nitrogen’s and alkyl chains are connected through ester bonds (**Scheme 1.5C**). In this respect, those designs were examined for the removal of methyl orange from aqueous solutions (Kan, Jiang, Zhou, Yang, Duan, Liu, & Jiang, 2011; C. Wang, Jiang, Zhou, Xia, Chen, Duan, & Jiang, 2013). The interaction of the ester-bonded surfactant with bovine serum albumin has been reported as well (Ya Wang, Jiang, Zhou, Yang, Xia, Chen, & Duan, 2013).

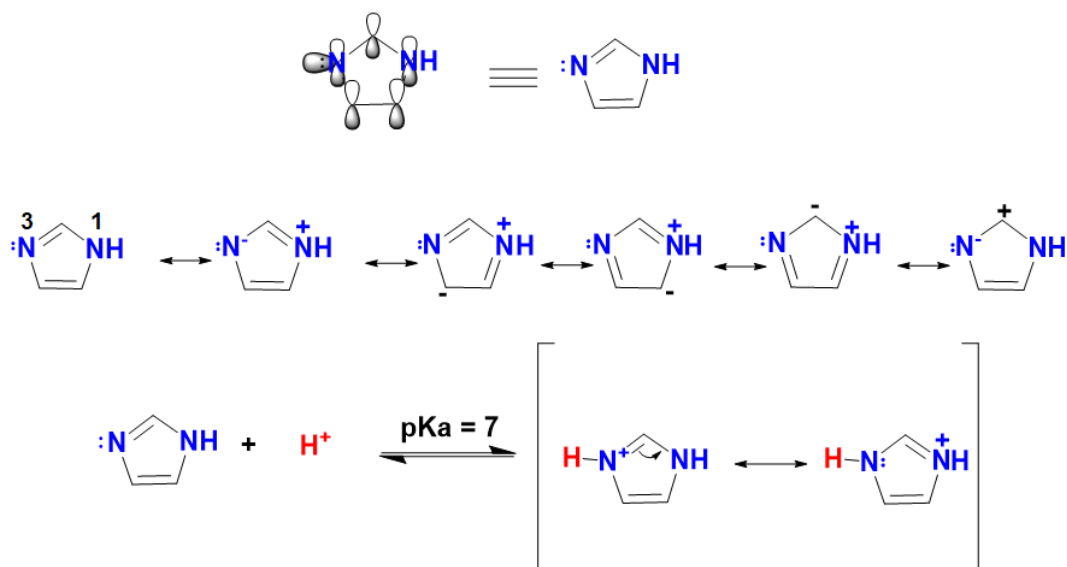
To the best of our knowledge, there is no report on the interfacial behavior of water insoluble, pyridinium GSs at the air-water and air-solid interfaces, except the work of Maximilian Franke and Heinz Rehage that were published during the course of this work (*vide supra*). So the reader is directed to read the review by Heinz-Bernhard Kraatz and co-workers and the articles discussed therein for more information about the synthesis and aggregation behavior of water soluble pyridinium GS (Sharma, Kamal, Abdinejad, Mahajan, & Kraatz, 2017a).



**Scheme 1.5.** The chemical structure of: **A.** NA; **B.** NA-ester and **C.** Representative NA based GSs.

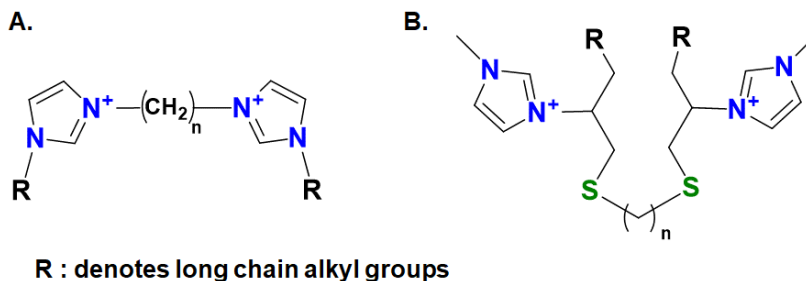
### 1.3 Imidazolium-based GSs

Imidazole (1,3-diazacyclopenta-2,4-diene ( $C_3H_3N_2$ )) is a five-membered, heterocyclic aromatic compound, that contains two non-adjacent nitrogen atoms. The first one (labeled as 1) is not basic as its electron pair is a part of the aromatic six- $\pi$ -electron system. The second nitrogen atom (labeled as 3) is about 100 times more basic than pyridine. The higher basicity is attributed to the resonance stabilization of the positive charge of the conjugate acid. The chemical structure of the resonance stabilized imidazole, imidazolium ion and their resonance stabilized structures are presented in **Scheme 1.6**. Imidazole is a building block of histidine and histamine (“Britannica Encyclopedia,” 2018) and it is found in the chemical structure of many antibiotics and antifungal drugs.



**Scheme 1.6.** The chemical structure of: **A.** Imidazole and **B.** Imidazolium cation and their resonance structures (Joule & Mills, 2010).

Away from the water soluble, surface active 1-alkyl-3-methyl imidazolium (A. F. Eftaiha, Qaroush, Kayed, Abdel Rahman, Assaf, & Paige, 2020a) and their diverse applications as antimicrobial agents (Garcia, Ribosa, Perez, Manresa, & Comelles, 2013), or stabilizers in the synthesis of nanoparticles (Souza, Souza, Tondo, Leopoldino, Fiedler, & Nome, 2015), the first imidazolium GS (1,1'-(alkane-1,4-diyl)bis(3-alkyl-1H-imidazol-3-ium), **Scheme 1.7A**) was synthesized and compared with 1-n-tetradecyl-3-methylimidazolium (Ding, Zha, Zhang, & Wang, 2007). Results indicated that the more symmetrical surfactant structure enhanced thermal stability and crystallinity. In addition, the CMC value of the GS was 200 times lower than that the conventional surfactant counterpart. Moreover, a series of alkylene-dithiol tethered imidazolium GSs (**Scheme 1.7B**) were synthesized and fully characterized. The area per surfactant molecule at the air-water interface ( $A_{min}$ ), evaluated from Gibbs adsorption isotherm, of the surfactant bearing dodecyl chains, increased with increasing spacer length; however, the reverse scenario was observed for the gemini with the tetradecyl chain length. This was attributed to the tendency of the latter to form premicellar aggregates in bulk solution. The CMC values of these surfactants lower than for the conventional counterparts and other categories of gemini pyridinium (**Scheme 1.4C** (Quagliotto *et al.*, 2003), **Scheme 1.4E** (L. Zhou, Jiang, Li, Chen, & Hu, 2007) and quaternary ammonium (alkanediyl- $\alpha,\omega$ -bis(dkyl)dimethylammonium bromide) (Alami, Beinert, Marie, & Zana, 1993) surfactants having similar hydrophobic alkyl chain lengths (Bhadani & Singh, 2011).



**Scheme 1.7.** The chemical structure of selected imidazolium GSs. **A.** 1,1'-(alkane-1,4-diyl)bis(3-alkyl-1H-imidazol-3-ium) and **B.** 3,3'-((alkane-1,5-diylbis(sulfanediy))bis(alkane-2,1-diyl))bis(1-methyl-1H-imidazol-3-ium).

Datta *et al.* reported on a series of silver nanoparticle capped with hexadecyl gemini imidazolium surfactants at air-water and air-solid interfaces (**Scheme 1.7A**) (Datta, Biswas, & Bhattacharya, 2014a). The limiting molecular area obtained from  $\pi$ -A isotherms, indicated that short spacers adopt more extended conformation to minimize the electrostatic repulsion between the cationic headgroups. Interestingly, while Brewster Angle Microscopy (BAM) images of the imidazolium GSs showed no contrast, the reflectivity of the capped nanoparticles domains was a function of surface pressure. The Atomic Force Microscopy (AFM) images of Langmuir Blodgett (LB) films indicated the formation of compact tubular morphology, with the occurrence of spherical islands. It is worth to emphasize that although there is a plenty of literature reports on imidazolium GSs, we discussed few examples as this master thesis is focused on exploring water insoluble monolayers.

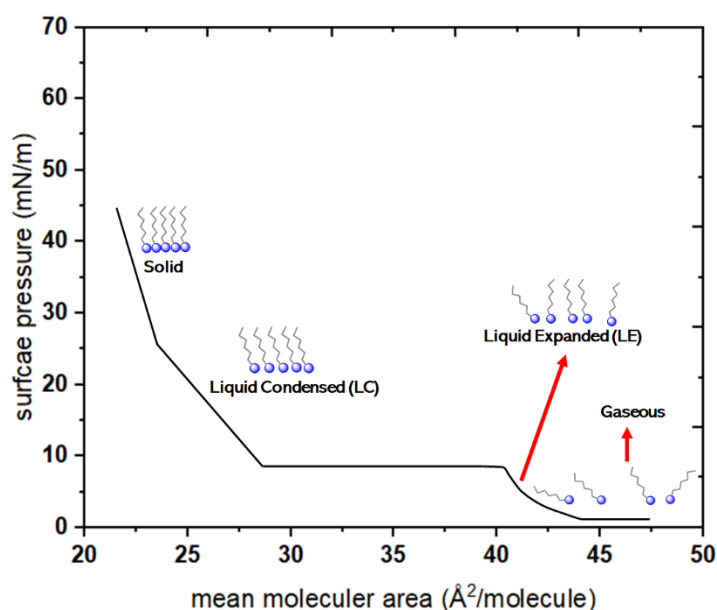
#### 1.4 Insoluble Surfactant Monolayers

An interface is the boundary between two phases such as solid-liquid, solid-gas, and liquid gas, or two immiscible liquids as in water and hexane. It is not a sharp border line and a highly turbulent region, with a thickness defined by density and molecular orientation. For example molecules evaporate from the liquid surface into the vapor phase and diffuse into the bulk phase from the surface (Butt, 2010). The interaction between interfaces is influenced by surfactants adsorption. If the surface tension decreases when surfactant concentration is increase, it tends to accumulate at the interface. Above a certain concentration (defined previously as CMC), the surface tension does not change any more, because the added surfactant goes into micelles, and not to the air-liquid interface.

Water insoluble surfactants form monomolecular layers (known as Langmuir monolayers) at the air-water interface, by spreading surfactants dissolved in a volatile, water immiscible solvent on the surface

of an aqueous subphase. After the solvent evaporation, the surfactant molecules spread over the entire surface, where the polar headgroups contact the aqueous subphase, and the hydrophobic tails point to the air in various orientations relative to the surface plane (Sorrenti, Illa, & Ortuño, 2013; Giner-Casares, Brezesinski, & Möhwald, 2014). Changing the monolayer packing would affect the surface pressure ( $\pi$ ), which equals to the difference in surface tension between the bare liquid surface ( $\gamma_0$ ) and in the presence of a film ( $\gamma$ );  $\pi = \gamma_0 - \gamma$  (Michael C. Petty, 1996). Monitoring  $\pi$  as a function of the area occupied by a molecule (or mean molecular area,  $A$ ) would result in the two-dimensional phase diagram as presented in **Scheme 1.8**.

For long chain alcohols, fatty acids or amines, low monolayer packing, or large mean molecular area corresponds to gaseous phase, no interaction between molecules. Adding more surfactant molecules or reducing the film area results in a liquid expanded (LE) phase, that is characterized by translational disorder together with disordered conformations of the hydrocarbon chains. A further increase in the surface pressure leads to a liquid condensed (LC) phase. At this stage, the surfactants molecules become closer with smaller tilt angle with respect to the surface normal. Further film compression causes a linear increase in pressure, after which no pressure increase is recorded above the collapse pressure (Hann, 1990).

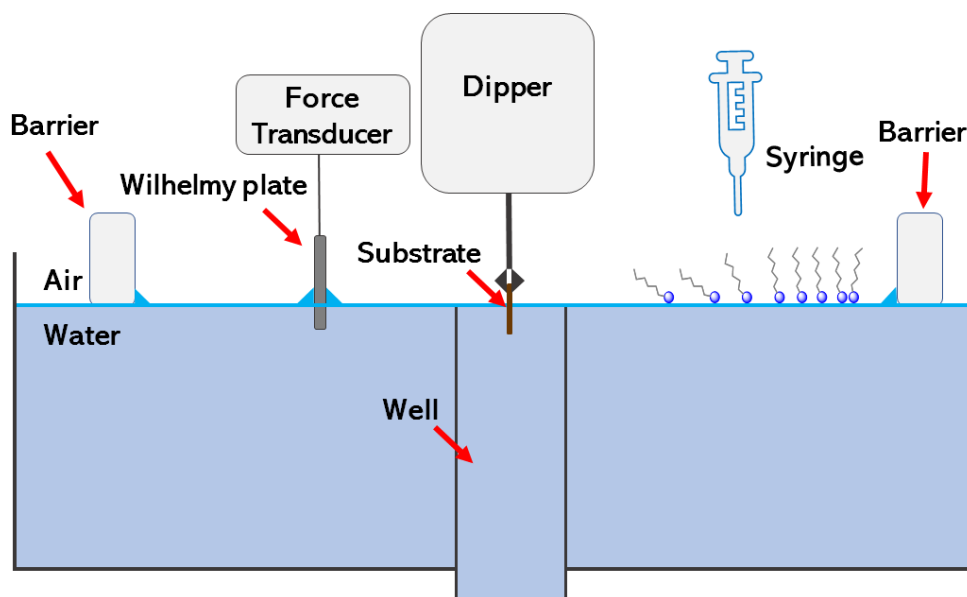


**Scheme 1.8.** A hypothetical  $\pi$ - $A$  isotherm that shows the most characteristic features of an insoluble surfactant monolayer.  $A$  ( $\text{\AA}^2/\text{molecule}$ ) is calculated using the following equation:  $Area_{trough} M / c N_A V$ , where the trough area is in  $\text{\AA}^2$ ,  $M$  is the surfactant molecular weight (g/mol),  $c$  is concentration (g/L),  $N_A$  is Avogadro's number (molecule/mol) and  $V$  is the spreading volume of solution (L) (Michael C. Petty, 1996).

## 1.5 Langmuir and Langmuir-Blodgett Trough

Langmuir trough is used to explore the interfacial behavior of insoluble surfactant films at air-water (Murray & Nelson, 1996). As shown in **Scheme 1.9**, the polytetrafluoroethylene trough contains two movable, hydrophilic, Delrin-made barriers located at the top of it, in contact with the aqueous subphase to control the film area. The trough is equipped with a Wilhelmy balance to monitor the change in the surface pressure (Michael C. Petty, 1996).

Langmuir-Blodgett (LB) technique provides a platform to transfer insoluble monolayers onto the air-solid interface by a vertical movement of a solid, hydrophilic substrate (glass or mica) through a dipping well **Scheme 1.9**. Upon immersing a previously cleaned substrate, surfactant spreading, solvent evaporation, and compressing the monolayer up to a desired surface pressure, subsequently, the substrate is pulled up and the monolayer is transferred with the headgroups oriented towards the substrate and the alkyl chains exposed to the air (M. C. Petty & Barlow, 1990)

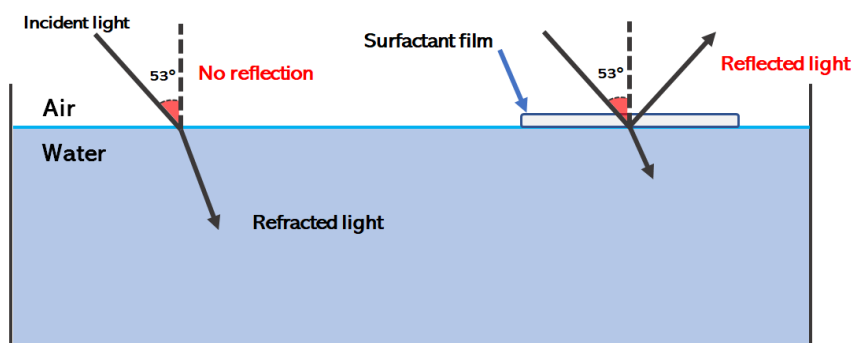


**Scheme 1.9.** A graphical illustration of a Langmuir/LB trough. This Figure has been redrawn from the work of R. F. de Oliveira *et al.* (de Oliveira, de Barros, & Ferreira, 2017).

## 1.6 Brewster Angle Microscopy (BAM)

BAM is a real-time imaging technique of surfactant monolayers at the air-water interface. The general principle of BAM is presented in **Scheme 1.10**. When a parallel polarized light, *i.e.*, the electric field is parallel to the plane of incidence, illuminates at a clean water surface by  $53.1^\circ$  to the surface normal

(estimated by  $\tan^{-1}\left(\frac{\text{Refractive index}_{\text{water}}}{\text{Refractive index}_{\text{air}}}\right)$ ), the light is refracted and the surface appears as a dark area, while in the presence of a film, light is reflected and a bright region is appeared, where the brightness depend on the monolayer density (Stine, 2012). This technique provides diffraction-limited images on the microscale, without the need of adding probe molecules to the insoluble film (A. Eftaiha, Brunet, & Paige, 2012).

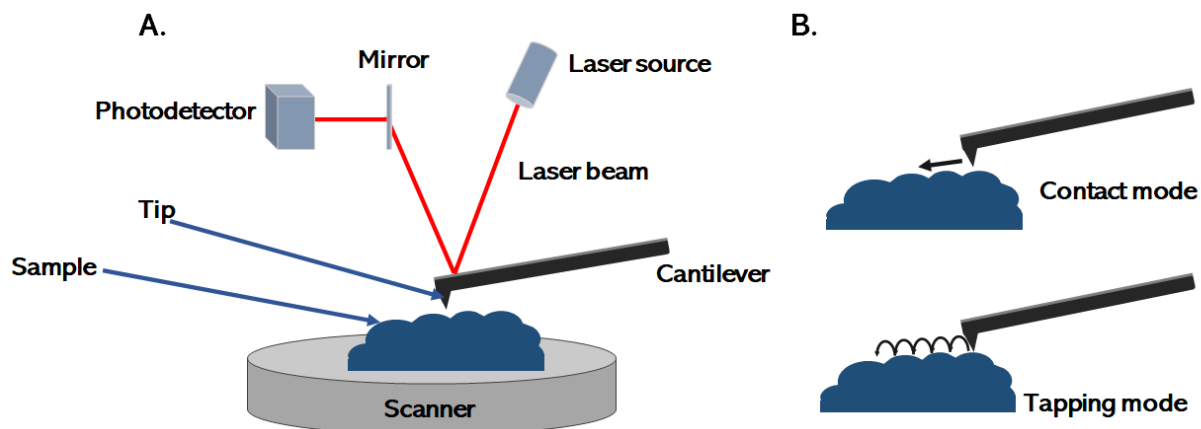


**Scheme 1.10.** An illustration of BAM principle. This Figure has been redrawn from the work of T. Kaercher *et al.* (Kaercher, Hönig, & Möbius, 1993)

## 1.7 Atomic Force Microscopy (AFM)

AFM is a technique that provides three dimensional topography of solid surfaces, with a spatial vertical resolution down to angstrom length scale and horizontal resolution on order of nanometers. (Eaton, 2014). It comprised of the microfabricated tip that is positioned to a flexible cantilever. The interaction between the tip and the sample causes a cantilever deflection, which is monitored by a feedback control of a laser beam reflection from the back of the cantilever, towards a photodetector, to keep the cantilever deflection constant by adjusting the position of the surface to a user-defined value (set point) (Eaton, 2014). A Schematic diagram of AFM scanned sample is shown in **Scheme 1.11A**.

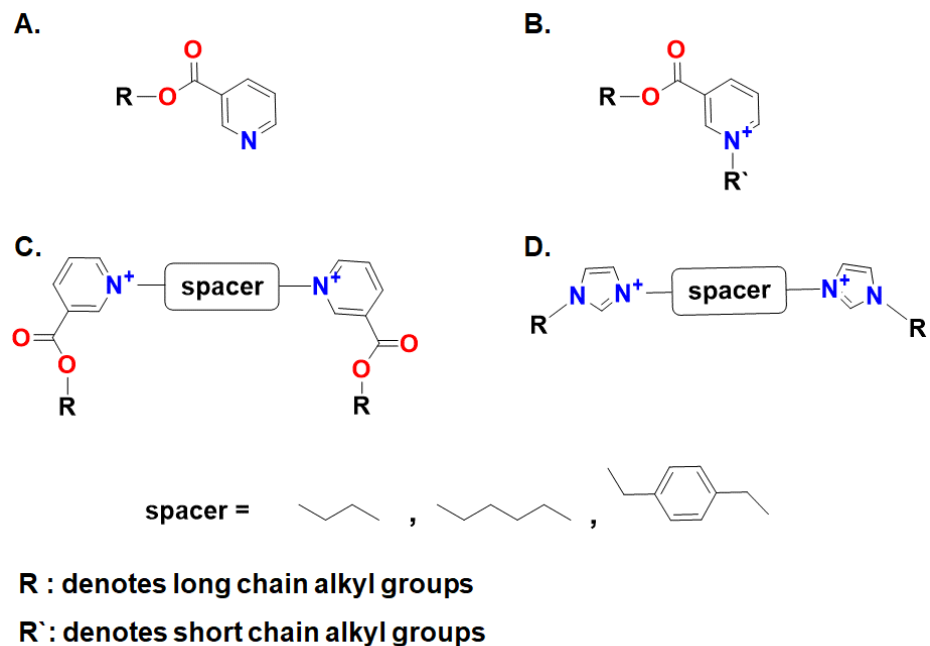
As shown in **Scheme 1.11B**, AFM is operated by contact and tapping modes. In the former, the tip is in a direct contact with the sample and scan the surface at constant deflection or constant height, while in tapping mode, the cantilever is vibrated at a certain resonance frequency with slightly lower resolution (Eaton, 2014). As AFM does not provide chemical information, morphological-compositional mapping is challenging and requires the use of complementary techniques for characterization of mixed films (A. Eftaiha *et al.*, 2012).



**Scheme 1.11.** **A.** Schematic illustration of AFM, **B.** presentation of tip movement in contact and tapping mode. This Figure has been redrawn from the work of Bert Voigtländer (Voigtländer, 2019).

## 1.8 Research Objectives

In this work, we would like to explore the interfacial properties of conventional and gemini NA based surfactants (**Scheme 1.12**) using the Langmuir and LB techniques. The self-assembly pure and mixed surfactant monolayers will be investigated using at air-water and air-solid interfaces using BAM and AFM, respectively. Density functional theory (DFT) calculations will be used to understand *homo*- and *hetero*-pair interactions. For comparison purposes, quaternized NA-ester and a series of imidazolium-based GSs will be studied as well. The target compounds will be synthesized and characterized by different spectroscopic techniques including nuclear magnetic resonance ( $^1\text{H}/^{13}\text{C}$  NMR), *ex situ* attenuated total reflectance Fourier transform infrared (ATR-FTIR) spectroscopy. The chemical structures will be further confirmed using elemental analysis (EA) and high-resolution mass spectroscopy (HR-MS).



**Scheme 1.12.** The chemical structure of **A.** NA-ester; **B.** Quaternized NA-ester; **C** and **D.** The proposed architectures of NA and imidazolium GSs, respectively.

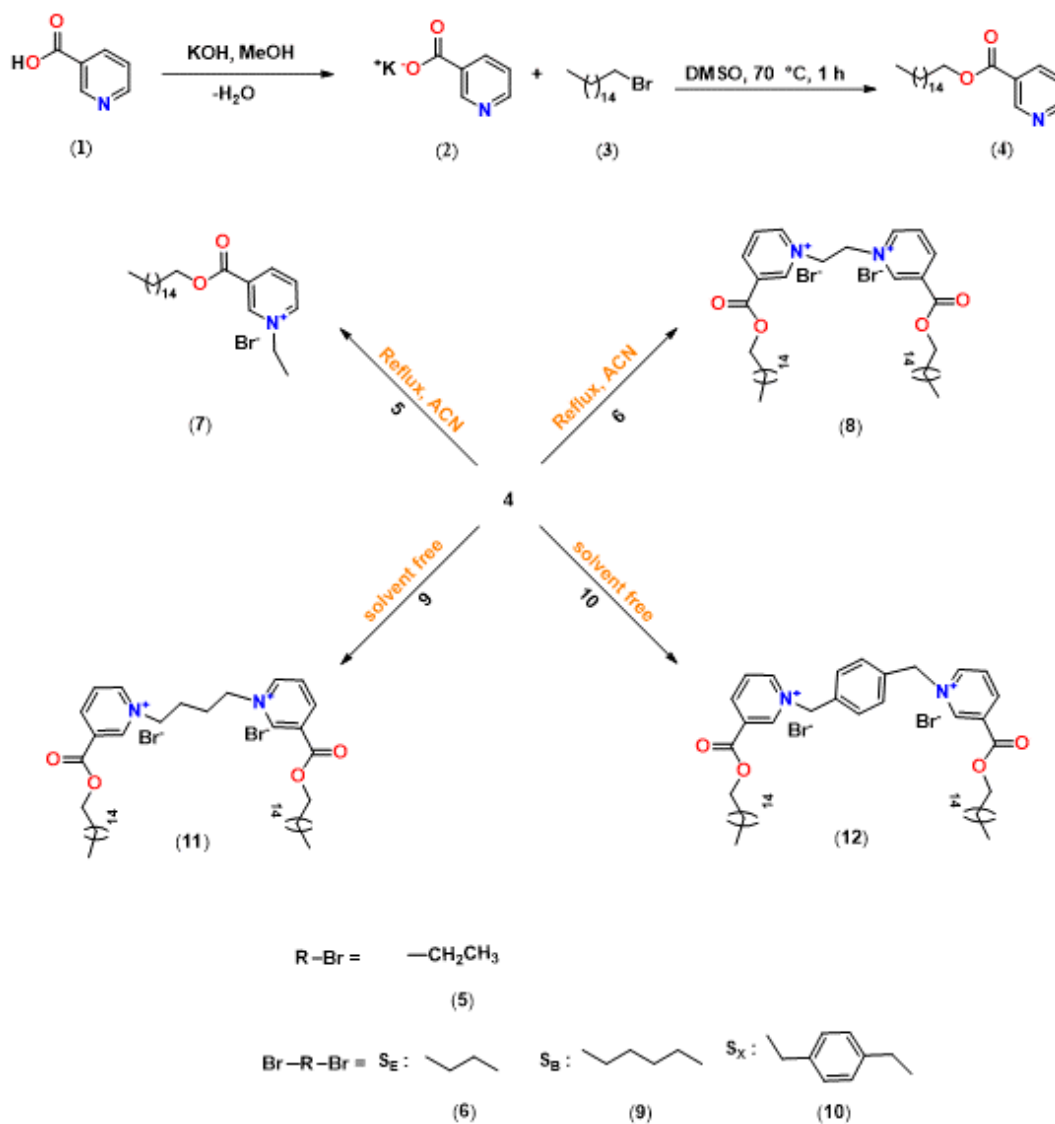
## Chapter 2

### The Synthesis and Characterization of Nicotinic acid and Imidazole-Based Cs/GS

This chapter is a verbatim copy of a paper published in ACS Langmuir. [Reprinted with permission from Langmuir, 2022, 38, 28, 8524–8533, Supporting Information. Copyright 2022 American Chemical Society.]

#### 2.1 Nicotinic acid-Based CS/GS

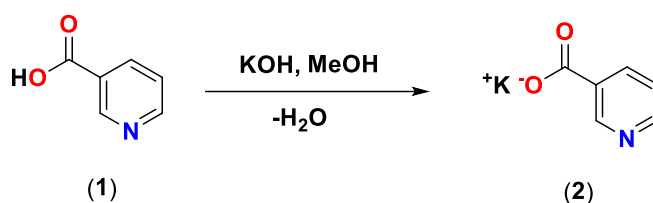
The synthesis of an ester-bonded, pyridinium-based "Gemini surfactants" (GSs) is described in bulk as well as solvent-assisted pathways as shown in **Scheme 2.1**. The first step starts with an activation of pyridine-3-carboxylic acid (nicotinic acid, NA, **1**), followed by the reaction with 1-bromohexadecane (**3**) to give the pyridine-based ester, hexadecyl nicotinate (**4**).



**Scheme 2.1.** Schematic representation for the synthesis of the ester-bonded, pyridine(ium)-based conventional; hexadecyl nicotinate (NA-C<sub>16</sub>, **4**) and 1-ethyl-3-((hexadecyloxy)carbonyl)pyridin-1-ium bromide Et-(NA<sup>+</sup>-C<sub>16</sub>•Br, **7**) as well as GSSs; **S<sub>E</sub>**: Ethylene spacer (**S<sub>E</sub>**(NA<sup>+</sup>-C<sub>16</sub>)<sub>2</sub>•2Br, **8**). **S<sub>B</sub>**: Butylene spacer (**S<sub>B</sub>**(NA<sup>+</sup>-C<sub>16</sub>)<sub>2</sub>•2Br, **11**). **S<sub>X</sub>**: Xylenylene spacer (**S<sub>X</sub>**(NA<sup>+</sup>-C<sub>16</sub>)<sub>2</sub>•2Br, **12**).

### 2.1.1 Activation of Nicotinic Acid (NA, 1)

A suspension of nicotinic acid (**1**, 5.0 g, 40.8 mmol) in 10 mL of methanol. Afterwards, a slightly excessive amount of an aqueous solution of potassium hydroxide (3.2 g, 57.6 mmol) was added. The mixture was stirred until the product was fully dissolved. Similarly, 40 mL of isopropanol was added to precipitate **2**, then the solid was collected using suction filtration, washed twice using Et<sub>2</sub>O (2 × 25 mL), dried in the oven at 60 °C for 2 h with a yield of 77 %. Melting point (uncorrected) = 334 °C. <sup>1</sup>H NMR: (400 MHz, D<sub>2</sub>O): δ 8.83 (s, *J* = 2.2 Hz, 1H), 8.49 (d, *J* = 5.1, 1.9 Hz, 1H), 8.18 – 8.06 (d, 1H), 7.40 (t, *J* = 8.0, 5.0 Hz, 1H). ATR-FTIR: (C=O) 1548 & 1558 cm<sup>-1</sup>, (Ar-H) 3048 cm<sup>-1</sup>.



**Scheme 2.2.** Deprotonation of NA (**1**) by KOH in MeOH.

The structure of **2** was examined using ATR-FTIR (**Figure 2.1**), where the O-H stretching at 2400 cm<sup>-1</sup> disappeared upon activation (Taylor, 1962). Furthermore, the C=O stretching frequency centered at 1700 cm<sup>-1</sup> shifted to a lower frequency and split into two symmetric and asymmetric stretching peaks of O=C=O centered at 1558 and 1548 cm<sup>-1</sup>, respectively (Lewandowski, Barańska, & Mościbroda, 1993). Meanwhile, **Figure 2.2** confirmed the disappearance of the -OH peak of **1** at 13.23 ppm.

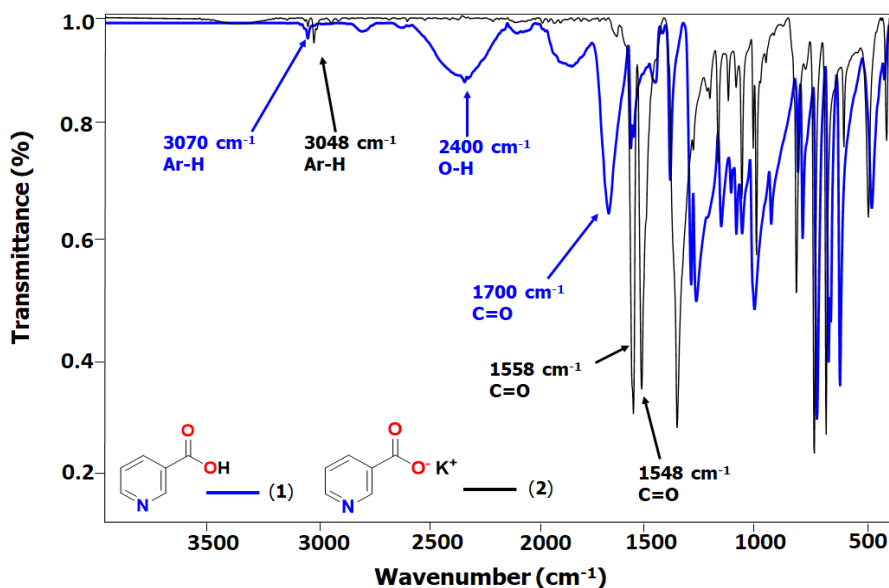


**Figure 2.1.** ATR-FTIR spectra of **1** (blue trace), and **2** (black trace).

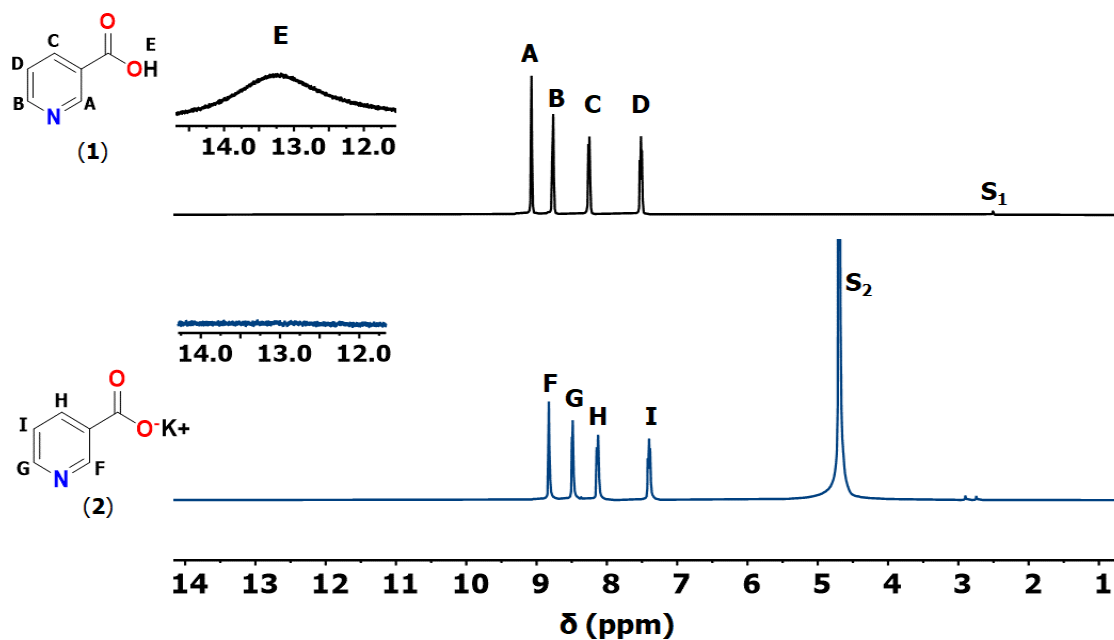
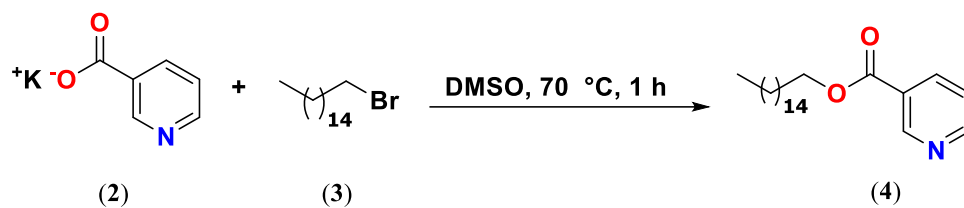


**Figure 2.2.**  $^1\text{H}$  NMR spectra of **1** (black trace,  $\text{S}_1$ : solvent =  $\text{DMSO-}d_6$ ), **2** (blue trace,  $\text{S}_2$ : solvent =  $\text{D}_2\text{O}$ ).

### 2.1.2 Synthesis of Hexadecyl Nicotinate (NA- $\text{C}_{16}$ , **4**)

Potassium nicotinate (**2**, 2.3 g, 14.3 mmol) was added into 100 mL DMSO and stirred until fully dissolved at 110 °C. The solution was left to cool down to 70 °C, followed by a dropwise addition of 1-bromohexadecane (**3**, 4.0 g, 12.0 mmol) in toluene, the reaction was left to stir for 1 h as shown in **Scheme 2.3**. The solution cooled down to room temperature, and the crude product was collected *via* suction filtration. The product was purified by liquid-liquid extraction (Hexane: ACN) (1:4), the ACN solution was placed in the freezer for 2 h to give white crystalline solid, which was collected by suction filtration with yield of 45 %. Melting point (uncorrected) = 50 °C .  $^1\text{H}$  NMR: (400 MHz,  $\text{CDCl}_3$ )  $\delta$  9.25 (s,  $J = 2.1$  Hz, 1H), 8.80 (d,  $J = 4.9, 1.8$  Hz, 1H), 8.33 (d,  $J = 8.0, 2.0$  Hz, 1H), 7.42 (t,  $J = 8.0, 4.8$  Hz, 1H), 4.37 (t,  $J = 6.7$  Hz, 2H), 1.80 (p,  $J = 6.9$  Hz, 2H), 1.59 – 1.11 (m, 29H), 0.90 (t,  $J = 6.7$  Hz, 3H).  $^{13}\text{C}$  NMR: (101 MHz,  $\text{CDCl}_3$ )  $\delta$  165.3, 153.3, 150.8, 137.03, 126.4, 123.2, 65.6, 31.9, 29.7, 29.6, 29.5, 29.3, 29.2, 28.6, 26.0, 22.7, 14.1. ATR-FTIR: (C=O st.) 1715  $\text{cm}^{-1}$ , (C-H st.) 2850 and 2910  $\text{cm}^{-1}$ , (Ar=C-H st.) 3091 $\text{cm}^{-1}$ . EA ( $\text{C}_{22}\text{H}_{37}\text{N}_1\text{O}_2$ ; Calculated (%): C, 76.03, H, 10.73, N, 4.03. Found (%): C, 76.19, H, 10.67, N, 4.03). HRMS ( $m/z$  of  $[\text{C}_{22}\text{H}_{37}\text{NO}_2 + \text{H}^+]$ , Calculated: 348.28970. Found: 348.29103).



**Scheme 2.3.** The synthesis of the nicotinate ester, NA-C<sub>16</sub> (4).

The structure was examined using ATR-FTIR, <sup>1</sup>H/<sup>13</sup>C NMR, and elemental analysis. As shown in **Figure 2.3**, the C=O peak shifted from 1548 and 1558 cm<sup>-1</sup> to 1715 cm<sup>-1</sup> accompanied with the appearance of strong C-H aliphatic tail peaks centered at 2910 and 2850 cm<sup>-1</sup> of the asymmetric and symmetric stretching frequencies, respectively. Furthermore, the peak of (Ar=C-H) stretching was blue shifted from 3048 to 3090 cm<sup>-1</sup> (Bora, Deb, Fuller, Slawin, Derek Woollins, & Dutta, 2010). <sup>1</sup>H NMR spectrum shows a new peak at 4.37 ppm (**L**, black trace, **Figure 2.4**) that is corresponding to the methylene moiety closest to the ester functional group, where in <sup>13</sup>C NMR spectrum a new peak emerged at 65.6 ppm for the same methylene moiety (**Q**, black trace, **Figure 2.5**) (Bora *et al.*, 2010).

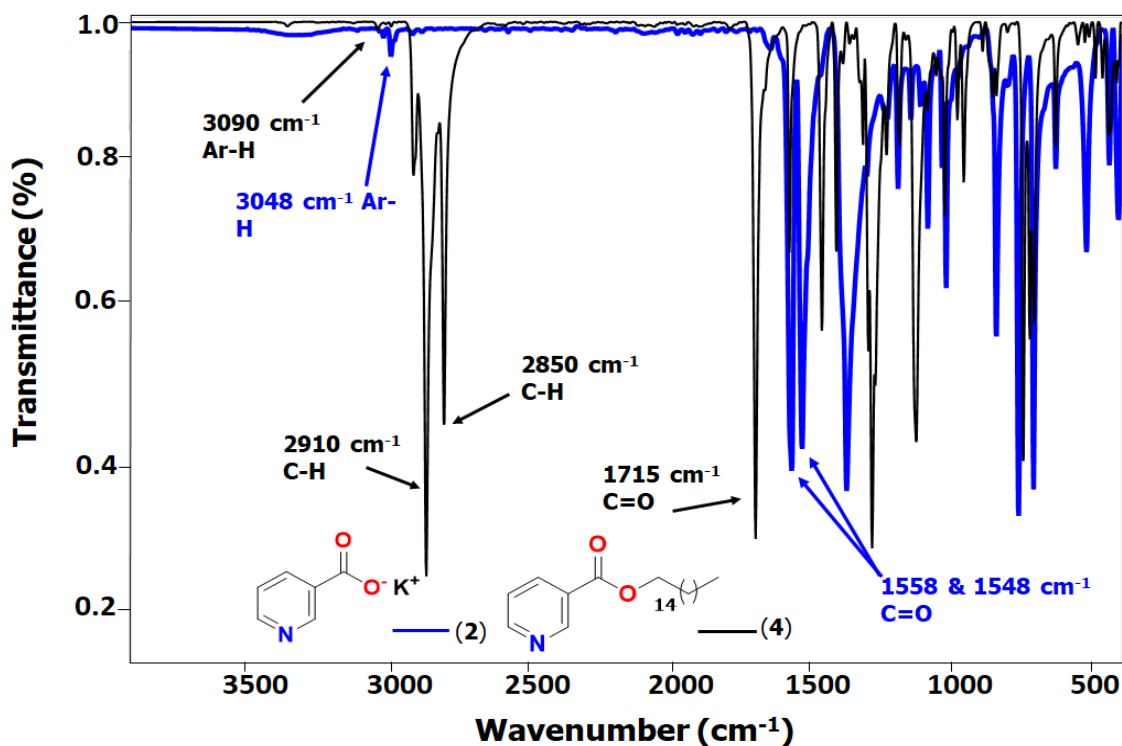


**Figure 2.3.** ATR-FTIR spectra of **2** (blue trace), and **4** (black trace).

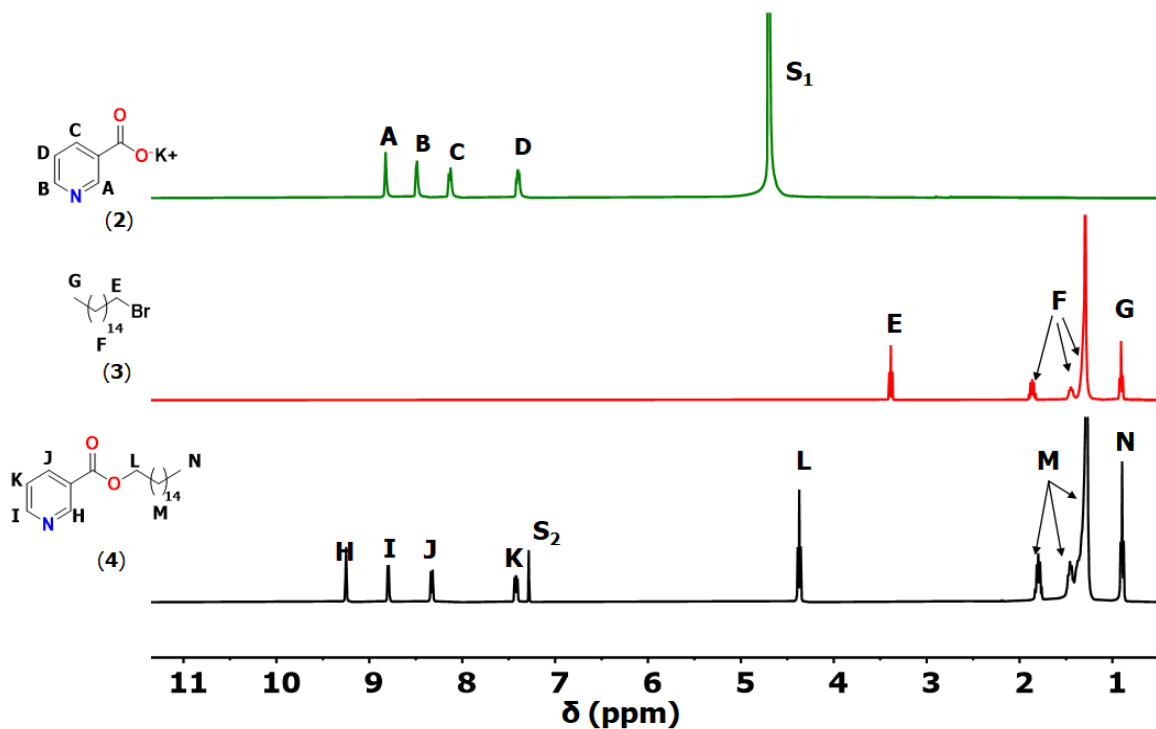


Figure 2.4.  $^1\text{H}$  NMR spectra of 2 (green trace,  $S_1$ : solvent =  $\text{D}_2\text{O}$ ), 3 (red trace) and 4 (black trace,  $S_2$ : solvent =  $\text{CDCl}_3$ ).

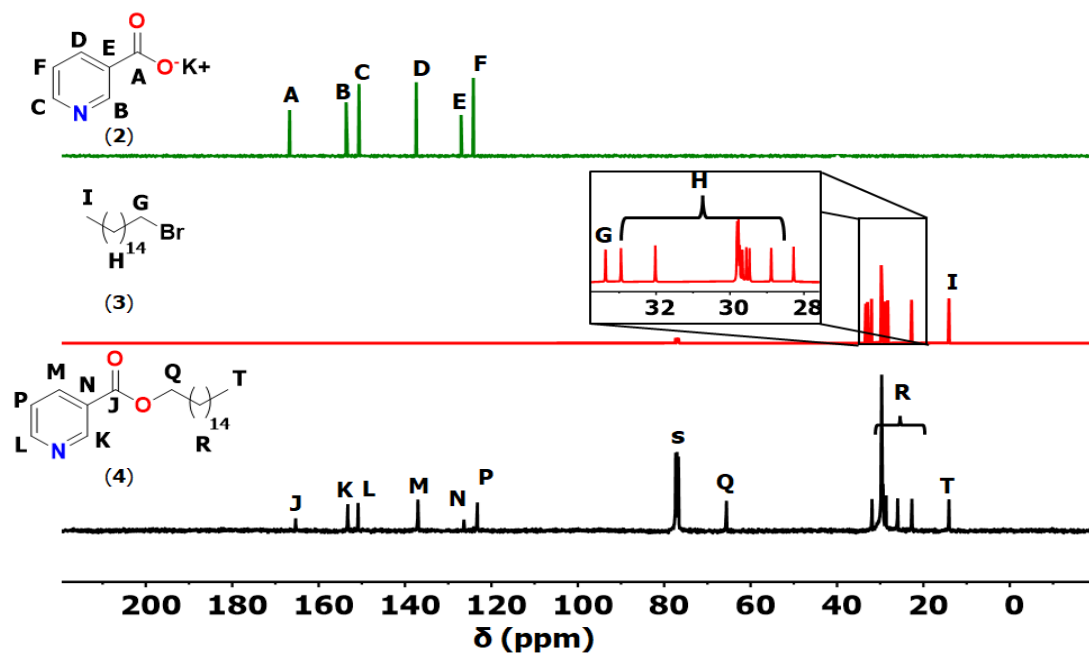
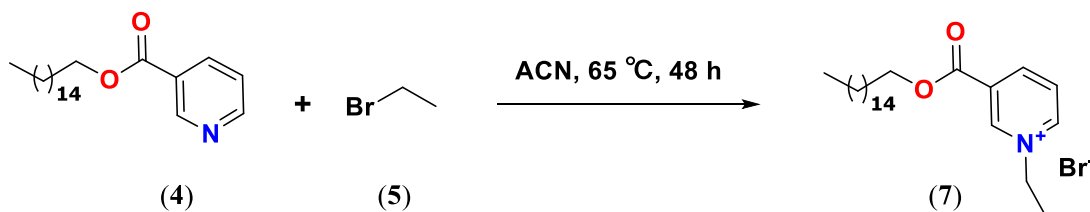


Figure 2.5.  $^{13}\text{C}$  NMR spectra of 2 (green trace, in =  $\text{D}_2\text{O}$ ), 3 (red trace) and 4 (black trace,  $S$ : solvent =  $\text{CDCl}_3$ ).

### 2.1.3 Synthesis of 1-ethyl-3-((hexadecyloxy)carbonyl)pyridin-1-ium bromide (Et-NA<sup>+</sup>-C<sub>16</sub>•Br, **7**)

The conventional surfactant **7** was prepared by dissolving hexadecyl nicotinate (**4**, 0.80 g, 2.30 mmol) and 1-bromoethane (**5**, 0.13 g, 1.15 mmol) in 10 mL, dried ACN using a 50 mL round-bottomed flask as shown in **Scheme 2.4**. The reaction was carried out at 65 °C for 48 h. After evaporating the solvent, the solid was dissolved in CHCl<sub>3</sub> and precipitated by the addition of Et<sub>2</sub>O (1:5). The collected solid was dried in the oven for 6 h at 60 °C. White crystalline solid was collected with a yield of 63 %. Melting point (uncorrected) = 75 °C. <sup>1</sup>H NMR: (400 MHz, CDCl<sub>3</sub>) δ 10.26 (d, *J* = 5.9 Hz, 1H), 9.38 (s, 1H), 8.94 (d, *J* = 8.0 Hz, 1H), 8.41 (t, *J* = 7.0 Hz, 1H), 5.24 (q, *J* = 7.3 Hz, 2H), 4.46 (t, *J* = 6.9 Hz, 2H), 1.82 (dt, *J* = 14.0, 7.0 Hz, 5H), 1.27 (s, 24H), 0.98 – 0.78 (m, 3H). <sup>13</sup>C NMR: (101 MHz, CDCl<sub>3</sub>) δ 161.1, 149.2, 144.9, 144.6, 130.9, 129.2, 67.6, 58.4, 32.5, 29.7, 14.1. ATR-FTIR: (Ar=C-H) 3011 cm<sup>-1</sup>, (C-H st) 2910 and 2850 cm<sup>-1</sup>, (C=O) 1715 cm<sup>-1</sup>, 1649, 1500, and 1470 cm<sup>-1</sup> pyridinium ring breathing mode. (C<sub>24</sub>H<sub>42</sub>NO<sub>2</sub>Br•0.05 CHCl<sub>3</sub>, 0.05 ACN; Calculated (%): C, 62.44, H, 9.16, N, 3.17. Found (%): C, 62.56, H, 9.06, N, 3.13). HRMS (*m/z* of [C<sub>24</sub>H<sub>42</sub>NO<sub>2</sub><sup>+</sup>], Calculated: 376.32100. Found: 376.32301).



**Scheme 2.4.** The synthesis of the charged conventional surfactant, Et-NA<sup>+</sup>-C<sub>16</sub>•Br (**7**).

The structure was verified by ATR-FTIR (**Figure S2.6**), in which a red shift for the pyridinium ring breathing mode was obtained from 1649 and 1558 to 1641 and 1500 cm<sup>-1</sup>, respectively. A similar red shift of Ar=C-H stretching peaks were observed from 3091 cm<sup>-1</sup> to 3011 cm<sup>-1</sup> (Kobetić & Sunko, 2008). <sup>1</sup>H NMR spectrum shows a new peak appeared at 5.24 ppm (**N**, black trace, **Figure S2.7**) for the methylene group attached to the pyridinium, accompanied with a downfield shift for the pyridinium ring. <sup>13</sup>C NMR spectrum shows (**T**, black trace, **Figure S2.8**) a new peak at 58.4 ppm for the methylene group attached to the pyridinium ring was emerged (Verdía, González, Rodríguez-Cabo, & Tojo, 2011).

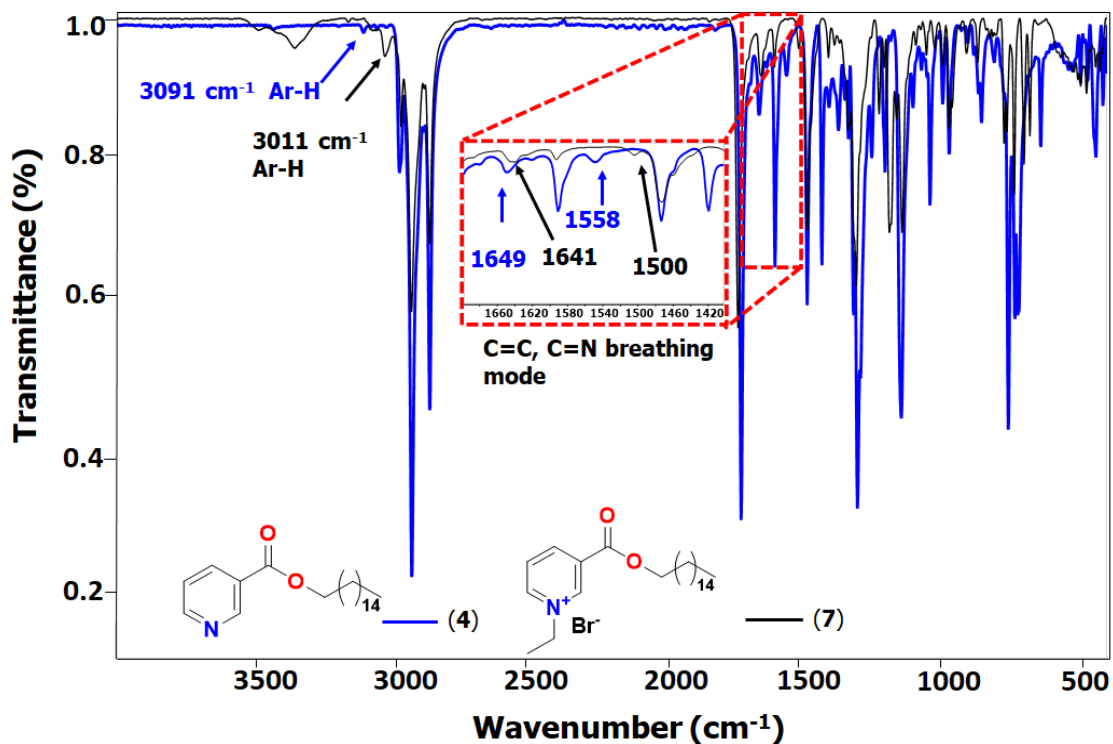


Figure S2.6. ATR-FTIR spectra of the surfactants **4** (blue trace), and **7** (black trace).

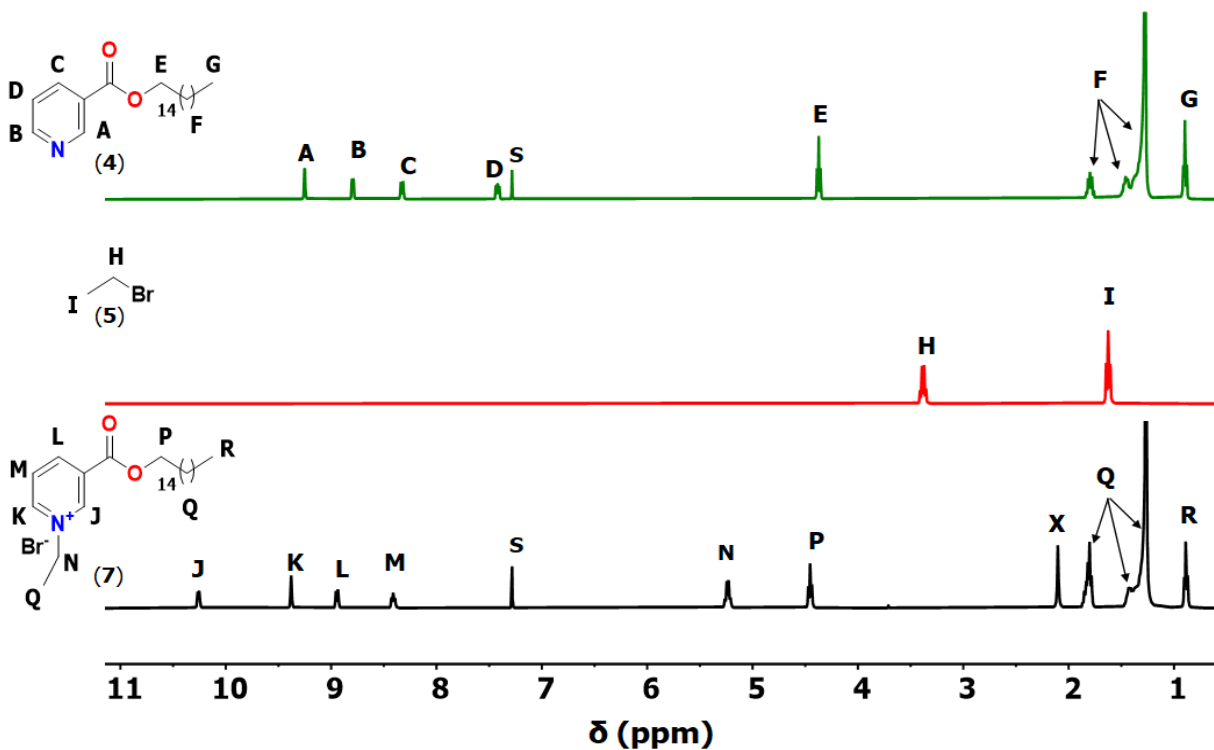
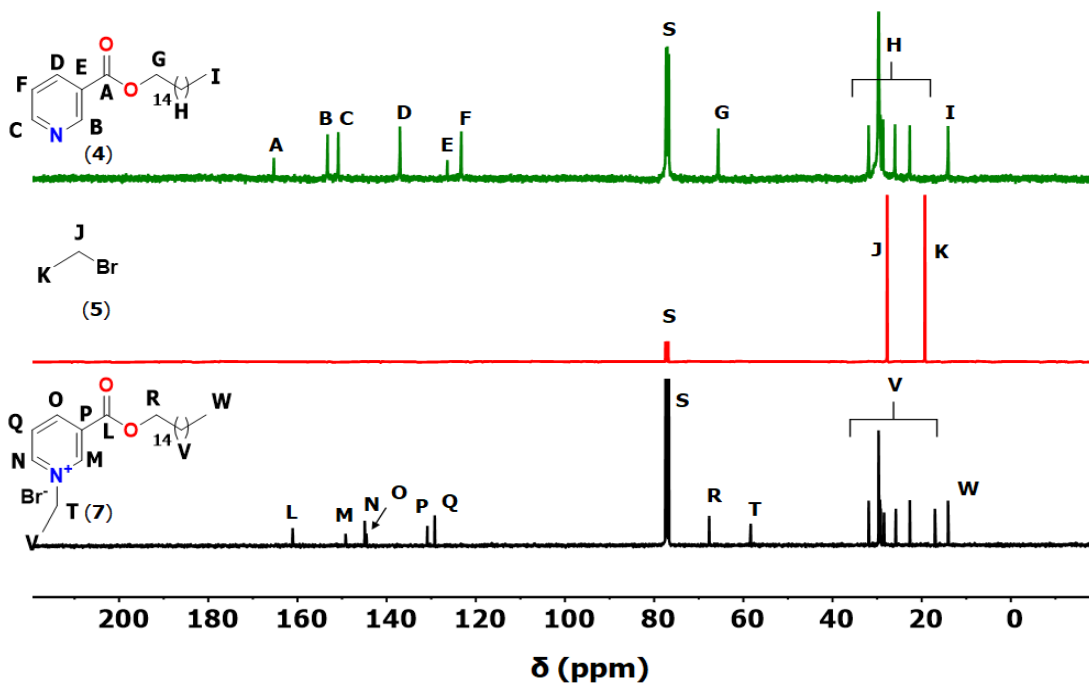


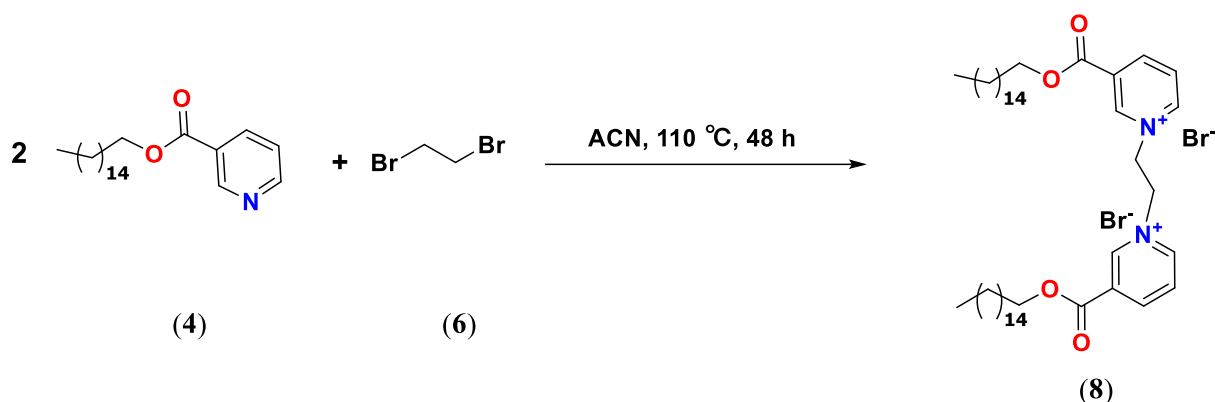
Figure S2.7.  $^1\text{H}$  NMR spectra of **4** (green trace), **5** (red trace) and **7** (black trace), S: solvent =  $\text{CDCl}_3$ , X = ACN.



**Figure S2.8.**  $^{13}\text{C}$  NMR spectra of **4** (green trace), **5** (red trace) and **7** (black trace), S: solvent =  $\text{CDCl}_3$ .

#### 2.1.4 Synthesis of 1,1'-(ethane-1,2-diyl)bis(3-((hexadecyloxy)carbonyl)pyridin-1-ium) bromide ( $\text{S}_\text{E}(\text{NA}^+-\text{C16})_2\cdot 2\text{Br}$ , **8**)

The ethylene-based GS **8** was prepared by dissolving hexadecyl nicotinate (**4**, 0.80 g, 2.30 mmol) and 1,2-dibromoethane (**6**, 0.145 g, 0.76 mmol) in 10 mL, dried ACN at 110 °C held for 48 h as presented in **Scheme S2.5**. After evaporating the solvent, the product was purified using a mixture of ( $\text{CHCl}_3:\text{Et}_2\text{O}$ ) (1:5) with a yield of 22 %. Melting point (uncorrected) = 233 °C.  $^1\text{H}$  NMR: (400 MHz,  $\text{EtOD}$  and  $\text{CDCl}_3$ )  $\delta$  10.47, 10.23, 10.21, 9.06, 9.04, 8.31, 8.29, 8.27, 8.24, 5.81, 5.78, 4.50, 4.48, 4.46, 4.44, 1.90, 1.88, 1.87, 1.83, 1.55, 1.45, 1.44, 1.43, 1.41, 1.33, 1.26, 1.22, 1.21, 1.21, 1.17, 1.14, 0.89, 0.87, 0.86.  $^{13}\text{C}$  NMR: (101 MHz,  $\text{EtOD}$  and  $\text{CDCl}_3$ )  $\delta$  161.1, 147.5, 146.4, 131.5, 128.7, 126.2, 67.7, 58.2, 31.85, 29.6, 29.6, 29.5, 29.3, 29.2, 28.4, 25.7, 22.6, 13.9. ATR-FTIR: (C=O) 1715  $\text{cm}^{-1}$ , (Ar=C-H) 3001  $\text{cm}^{-1}$ , (C-H) 2850, and 2910  $\text{cm}^{-1}$ , pyridinium ring breathing mode, 1637, 1500, and 1470  $\text{cm}^{-1}$ . EA ( $\text{C}_{46}\text{H}_{78}\text{N}_2\text{O}_4\text{Br}_2$ ; Calculated (%): C, 62.58, H= 8.90, N, 3.17. Found (%): C, 62.47, H, 8.89, N, 3.13). HRMS ( $m/z$  of  $[\text{C}_{45}\text{H}_{79}\text{N}_2\text{O}_4]^+$ , Calculated: 711.58172. Found: 711.60343).



**Scheme S2.5.** The synthesis of the ethylene-based GS,  $S_E(\text{NA}^+-\text{C}_{16})_2 \cdot 2\text{Br}$  (**8**).

As demonstrated in **Figure 2.9**, a red shift for the ring breathing mode peaks at 1650 and 1558  $\text{cm}^{-1}$  to 1637 and 1503  $\text{cm}^{-1}$ , respectively. Also, a red shift for Ar=C-H stretching peaks from 3091  $\text{cm}^{-1}$  to 3001  $\text{cm}^{-1}$ . Furthermore, the  $^1\text{H}/^{13}\text{C}$  NMR spectra (black traces; **M**, **Figure 2.10**, and **R**, **Figure 2.11**, respectively) confirmed the formation of **8** in which peaks at 5.81 and 58.2 ppm for the methylene moiety within the spacer group as proof of quaternization (L. Zhou *et al.*, 2007).

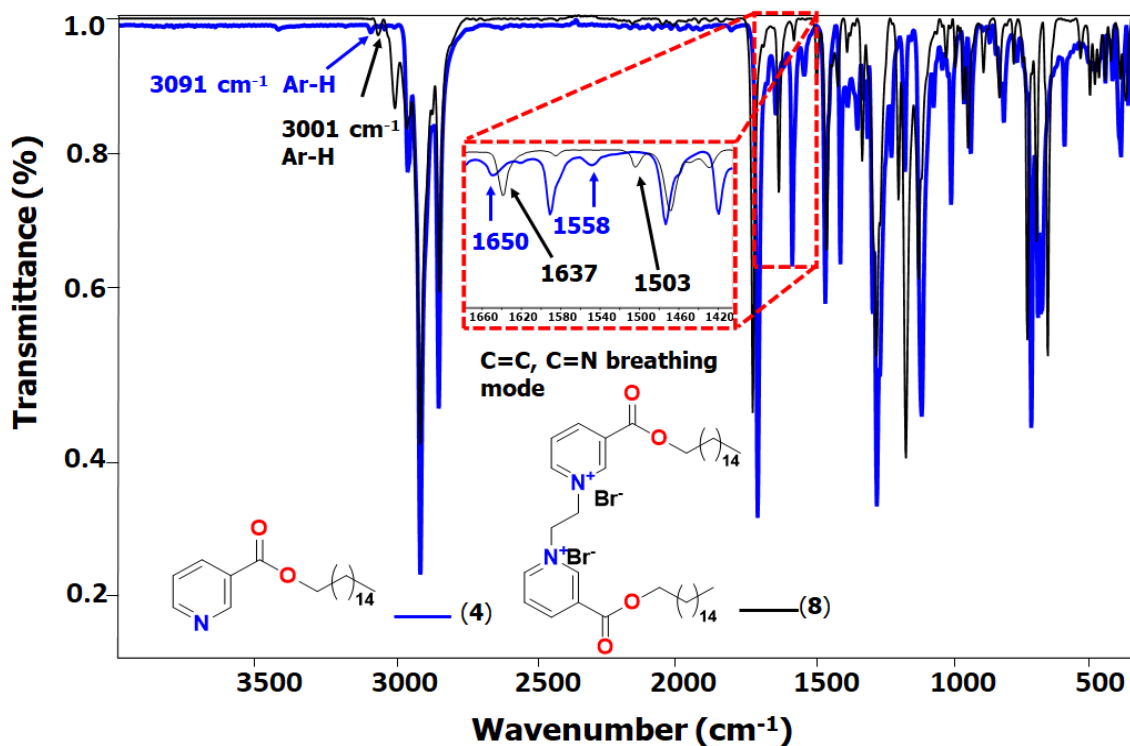


**Figure 2.9.** ATR-FTIR spectra of **4** (blue trace), and **8** (black trace)

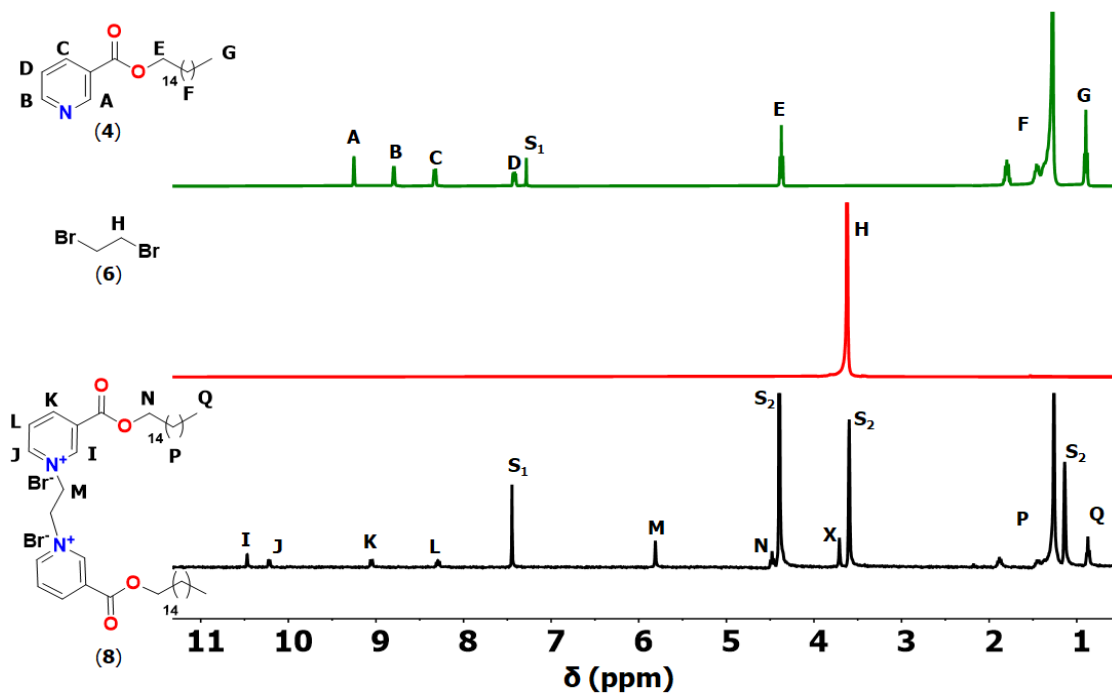


**Figure 2.10.**  $^1\text{H}$  NMR spectra of 4 (green trace), 6 (red trace,  $S_1$ : solvent =  $\text{CDCl}_3$ ) and 8 (black trace,  $S_1$ : solvent =  $\text{CDCl}_3$ ,  $S_2$ : solvent =  $\text{EtOD}$ , 3:2 (v/v) X =  $\text{Et}_2\text{O}$ )

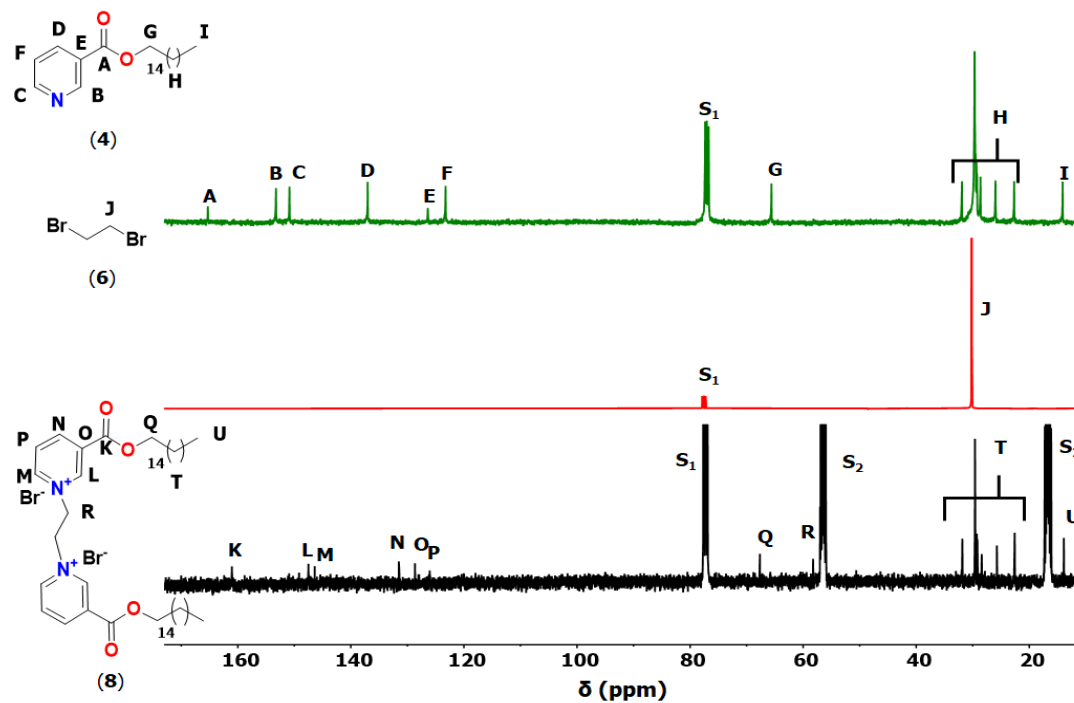
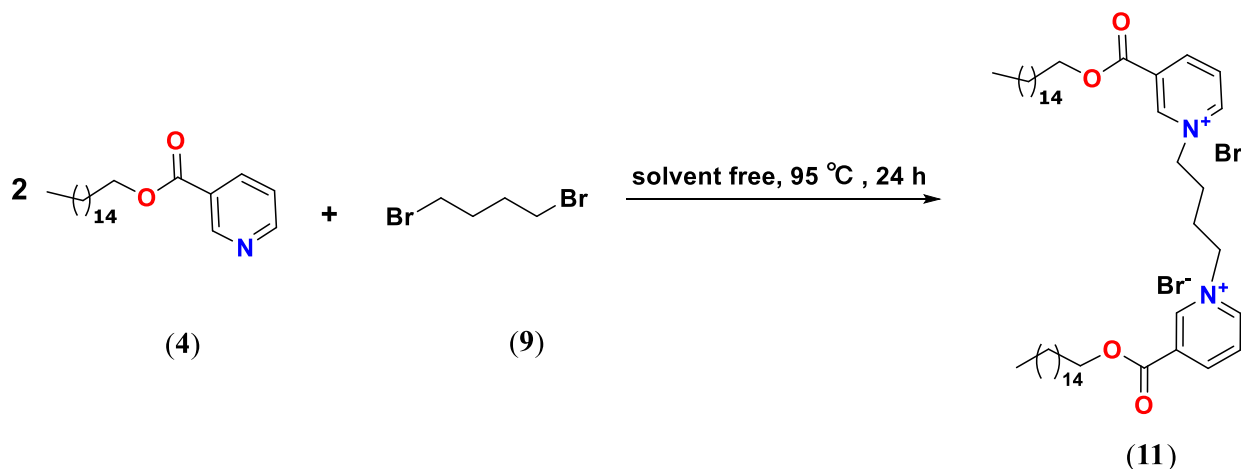


**Figure 2.11.**  $^{13}\text{C}$  NMR spectra of 4 (green trace), 6 (red trace,  $S_1$ : solvent =  $\text{CDCl}_3$ ) and 8 (black trace,  $S_1$ : solvent =  $\text{CDCl}_3$ ,  $S_2$ : solvent =  $\text{EtOD}$ , 3:2 (v/v))

### 2.1.5 Synthesis of 1,1'-(butane-1,4-diyl)bis(3-((hexadecyloxy)carbonyl)pyridin-1-ium) bromide ( $S_B(\text{NA}^+-\text{C}_{16})_2\cdot 2\text{Br}$ , **11**)

1,4-dibromobutane (**9**, 0.16 g, 0.74 mmol) was added to molten bulk of hexadecyl nicotinate (**4**, 0.80 g, 2.32 mmol). The reaction mixture was heated to 95 °C and left to stir for 24 h until a white solid was formed (**Scheme 2.6**). The obtained solid was dissolved in 5 mL  $\text{CHCl}_3$ , followed by a 50 mL  $\text{Et}_2\text{O}$  to precipitate **11** solely, which was dried in the oven for 2 h at 60 °C with a yield of 57 %. Melting point (uncorrected) = 185 °C,  $^1\text{H NMR}$ : (400 MHz,  $\text{CDCl}_3$ )  $\delta$  10.18 (s,  $J = 5.8$  Hz, 1H), 9.97 (d, 1H), 8.90 (d,  $J = 7.9$  Hz, 1H), 8.28 (t,  $J = 6.9$  Hz, 1H), 5.37 (s, 2H), 4.42 (t,  $J = 7.0$  Hz, 2H), 2.56 (d,  $J = 14.6$  Hz, 4H), 1.84 (p,  $J = 6.8$  Hz, 2H), 1.27 (s, 29H), 0.90 (t,  $J = 6.7$  Hz, 3H).  $^{13}\text{C NMR}$ : (101 MHz,  $\text{CDCl}_3$ )  $\delta$  161.1, 148.9, 146.1, 144.9, 131.2, 128.8, 67.7, 61.2, 29.7. **ATR-FTIR**: (Ar=C-H st) 3011  $\text{cm}^{-1}$ , (C-H st) 2910 and 2850  $\text{cm}^{-1}$ , (C=O st) 1714  $\text{cm}^{-1}$ , pyridinium ring breathing mode 1633, 1502 and 1470  $\text{cm}^{-1}$ . **EA** ( $\text{C}_{48}\text{H}_{82}\text{N}_2\text{O}_4\text{Br}_2$ ; Calculated (%): C, 63.15, H, 9.27, N, 3.08, Found (%): C, 63.25, H, 9.07, N, 3.08). **HRMS** ( $m/z$  of  $[\text{C}_{47}\text{H}_{83}\text{N}_2\text{O}_4]^+$ , Calculated: 739.63473. Found: 739.61267).



**Scheme 2.6.** The synthesis of butylene-based GS,  $S_B(\text{NA}^+-\text{C}_{16})_2\cdot 2\text{Br}$  (**11**).

ATR-FTIR spectra as shown in **Figure 2.12**, confirmed the formation of the postulated GS **11** in which the pyridinium ring breathing mode peaks were red shifted from 1650 and 1558  $\text{cm}^{-1}$  to 1633 and 1502  $\text{cm}^{-1}$ , respectively, accompanied with the shift of the Ar=C-H stretching peaks from 3091 to 3011  $\text{cm}^{-1}$  as a result of the successful quaternization process.  $^1\text{H NMR}$  spectrum (**Q** and **N**, black trace, **Figure 2.13**) showed two new peaks at 2.54 and 5.33 ppm for the inner and outer methylene moieties assigned for the spacer group. Additionally, the pyridine ring protons were deshielded as evidence of quaternarization,

which was further verified by a peak centered at 61.2 ppm as observed by  $^{13}\text{C}$  NMR spectroscopy (T, black trace, **Figure 2.14**) (Tu, Jiang, Zhou, Yin, Wang, Duan, Liu, & Jiang, 2012).

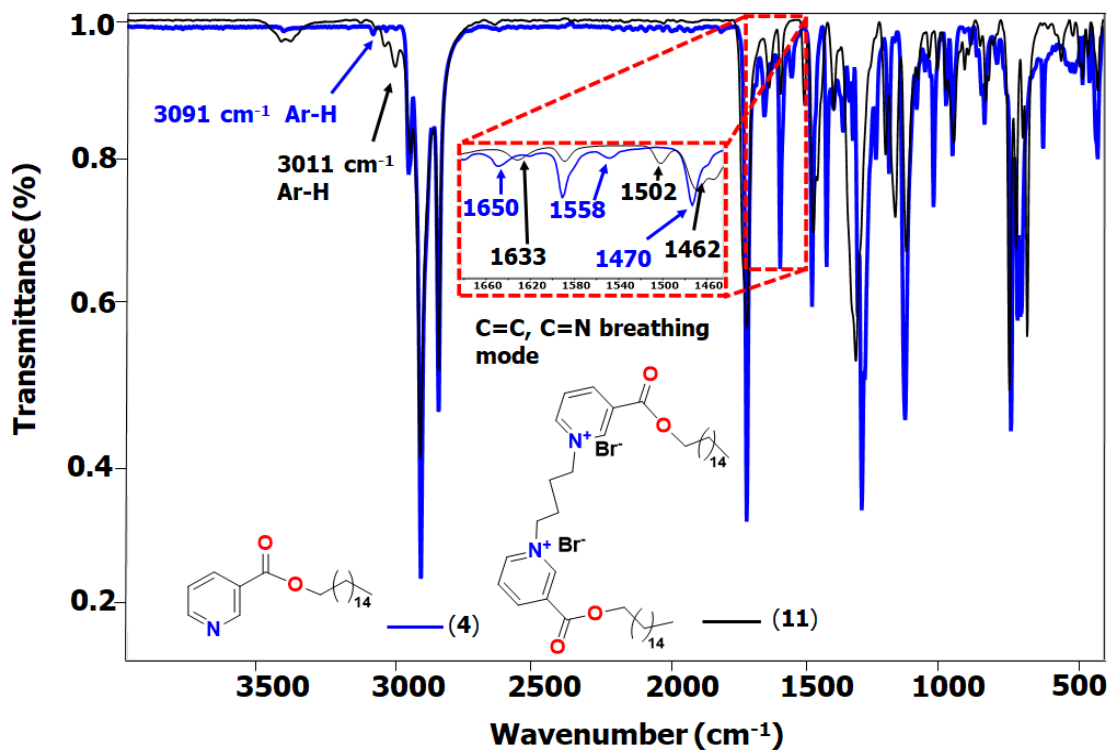


**Figure 2.12.** ATR-FTIR spectra of **4** (blue trace), and **11** (black trace).

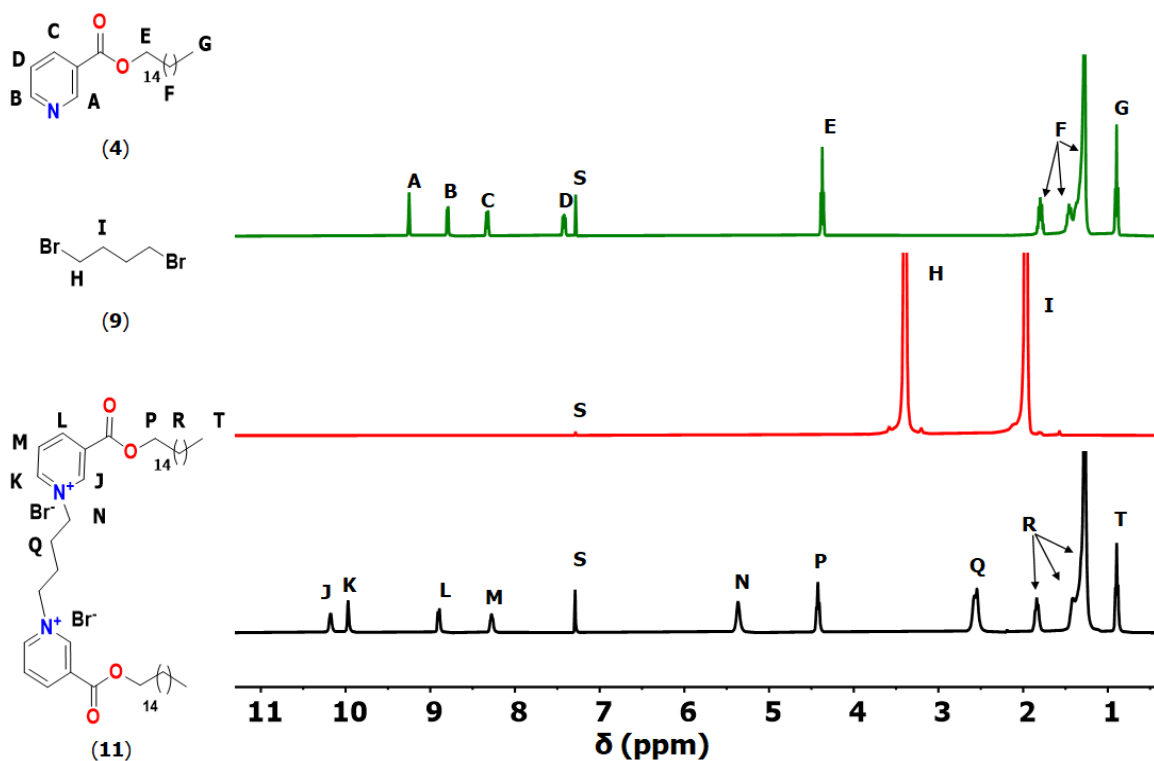


Figure 2.13.  $^1\text{H}$  NMR spectra of **4** (green trace), **9** (red trace) and **11** (black trace), S: solvent =  $\text{CDCl}_3$ .

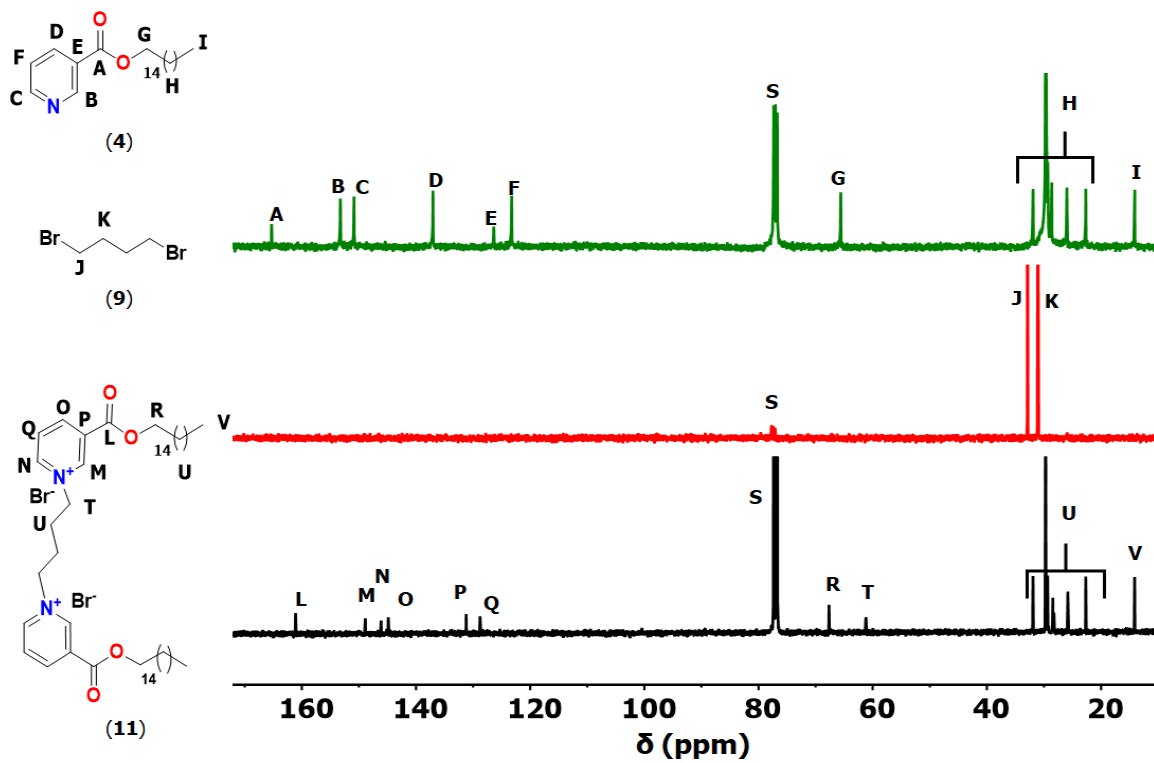
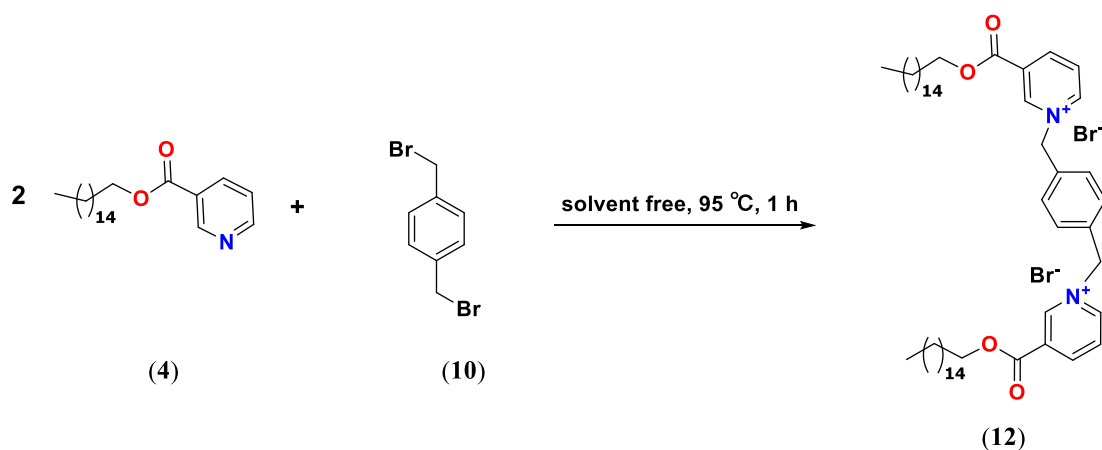


Figure 2.14.  $^{13}\text{C}$  NMR spectra of **4** (green trace), **9** (red trace) and **11** (black trace), S: solvent =  $\text{CDCl}_3$ .

### 2.1.6 Synthesis of 1,1'-(1,4-phenylenebis(methylene))bis(3-((hexadecyloxy)carbonyl)pyridin-1-ium) bromide ( $S_x(\text{NA}^+-\text{C}_{16})_2 \cdot 2\text{Br}$ , **12**)

The *p*-xylenyl-based GS **12** was prepared by melting hexadecyl nicotinate (**4**, 0.80 g, 2.30 mmol) at 50 °C, followed by the dropwise addition of  $\alpha,\alpha$ -dibromo-*p*-xylene dissolved in 2 mL  $\text{CHCl}_3$  (**10**, 0.2 g, 0.76 mmol), the temperature was increased to 95 °C (**Scheme 2.7**). After 1 h, a white solid formed. The pure product was obtained using a mixture of ( $\text{CHCl}_3:\text{Et}_2\text{O}$ ) (1:4) and dried in the oven for 2 h at 60 °C, with a yield of 72%. Melting point (uncorrected) = 175 °C.  $^1\text{H NMR}$ : (400 MHz,  $\text{CDCl}_3$ )  $\delta$  10.21 (d,  $J = 6.1$  Hz, 1H), 10.13 (s, 1H), 8.92 (d,  $J = 8.2$  Hz, 1H), 8.34 (t,  $J = 7.3$  Hz, 1H), 7.86 (s, 2H), 6.71 (s, 2H), 4.41 (t,  $J = 7.2$  Hz, 2H), 1.83 (p,  $J = 7.9, 7.4$  Hz, 2H), 1.27 (s, 22H), 0.89 (t,  $J = 6.9$  Hz, 3H).  $^{13}\text{C NMR}$ : (101 MHz,  $\text{CDCl}_3$ )  $\delta$  161.3, 149.0, 146.1, 145.3, 134.9, 131.2, 130.9, 129.1, 77.5, 77.2, 76.8, 67.8, 32.0, 29.8, 29.8, 29.8, 29.7, 29.5, 29.4, 28.6, 25.9, 22.8, 14.2. **ATR-FTIR**: (Ar= C-H st) 3011  $\text{cm}^{-1}$ , (C-H st) 2910  $\text{cm}^{-1}$  and 2850  $\text{cm}^{-1}$ , (C=O st) 1714  $\text{cm}^{-1}$ , pyridinium ring breathing mode 1633  $\text{cm}^{-1}$ , 1502  $\text{cm}^{-1}$ , 1640  $\text{cm}^{-1}$ , **EA** ( $\text{C}_{52}\text{H}_{82}\text{N}_2\text{O}_4\text{Br}_2$ ; Calculated (%): C, 65.12, H, 8.62, N, 2.92. Found (%): C, 65.24, H, 8.52, N, 3.00). **HRMS** ( $m/z$  of  $[\text{C}_{25}\text{H}_{35}\text{NO}_2]^+$ , Calculated: 381.26623. Found: 381.25214).



**Scheme 2.7.** The synthesis of *p*-xylenyl-based GS,  $S_x(\text{NA}^+-\text{C}_{16})_2 \cdot 2\text{Br}$  (**12**).

ATR-FTIR spectrum (**Figure 2.15**) reveals red shift in a breathing mode of the pyridinium peaks at 1650, 1558, and 1470  $\text{cm}^{-1}$  to 1633, 1502, and 1460  $\text{cm}^{-1}$ , respectively, accompanied by a red shift in the (Ar= C-H) stretching peak from 3091 to 3011  $\text{cm}^{-1}$  due to quaternization of the nitrogen atom (Tu *et al.*, 2012).  $^1\text{H NMR}$  spectrum showed the emergence of two new peaks at 6.71 and 7.86 ppm (**O** and **N**, black trace, **Figure 2.16**) which can be attributed to the methylene moiety and benzene ring in the spacer group, respectively. (M. Li, Fu, Yang, Zheng, He, Chen, & Li, 2005) Also, a slight shift was observed for the

neighboring methylene moiety closest to the ester functional group (**E** and **P**, **Figure 2.16**).  $^{13}\text{C}$  NMR spectrum exhibited two new peaks at 130.9 and 134.9 ppm for the benzene ring and a single peak at 63.0 ppm (**U**, **T** and **W**, black trace, **Figure 2.17**) for the methylene moiety that is attached to the pyridinium (Shakil Hussain, Kamal, & Murtaza, 2019).

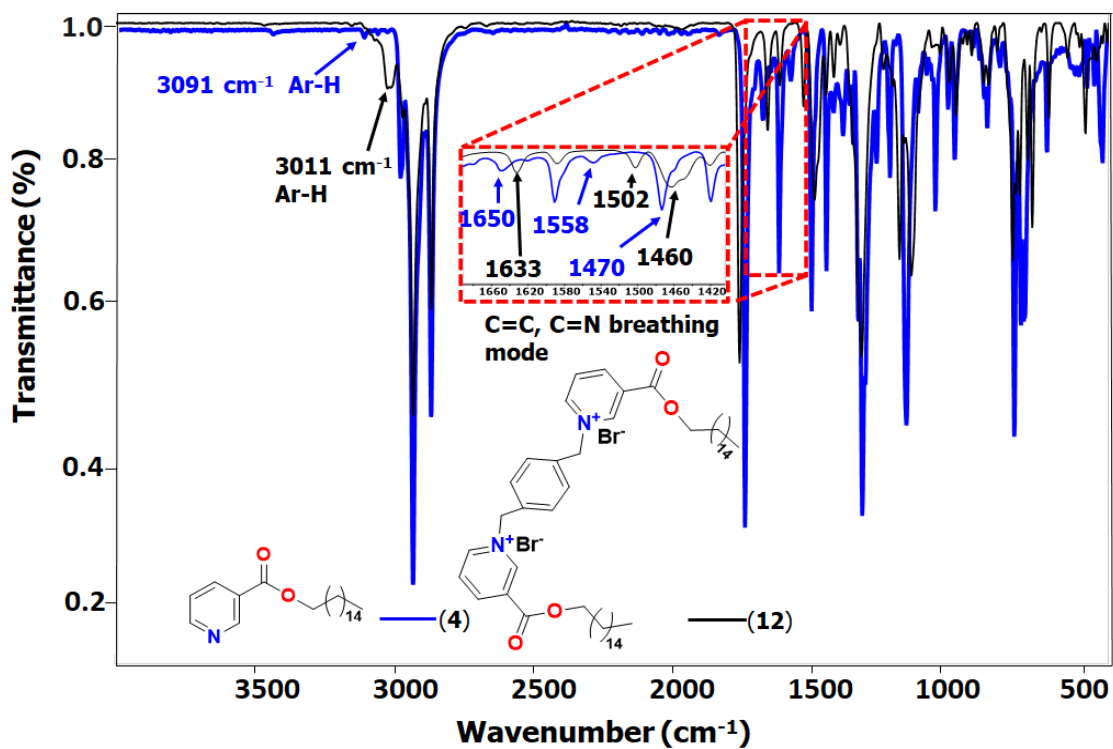


**Figure 2.15.** ATR-FTIR spectra of **4** (blue trace), **12** (black trace).

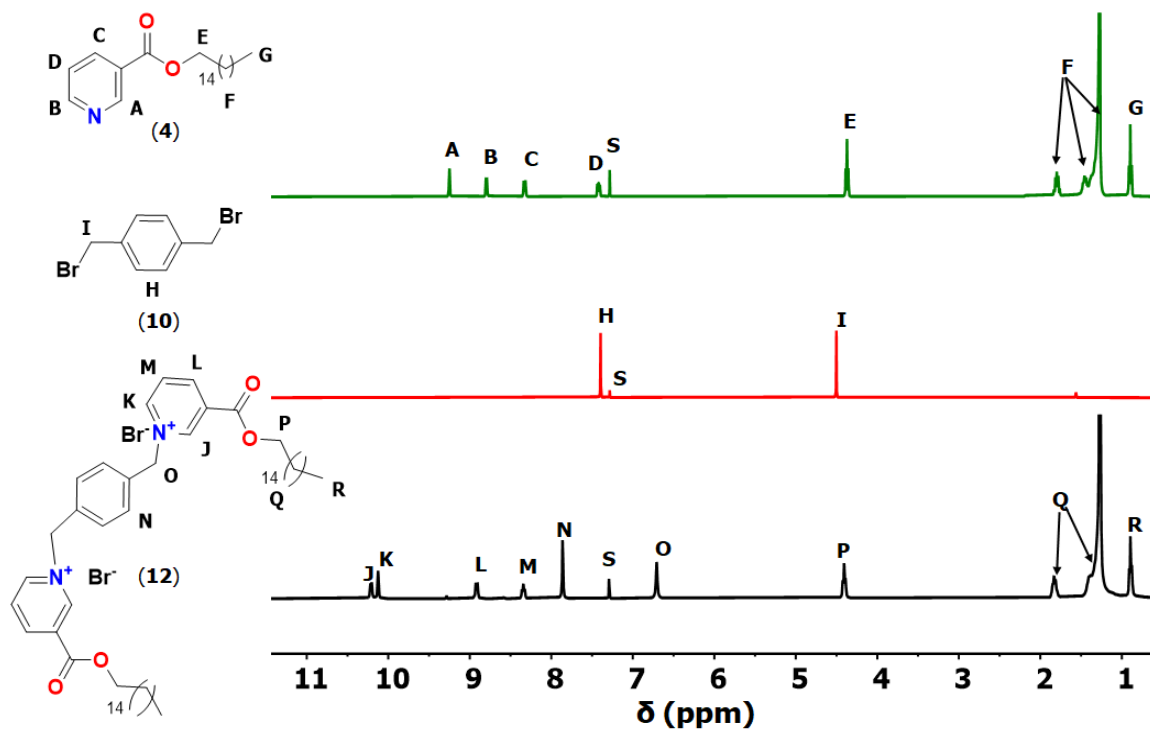


Figure 2.16.  $^1\text{H}$  NMR spectra of 4 (green trace), 10 (red trace) and 12 (black trace), S: solvent =  $\text{CDCl}_3$ .

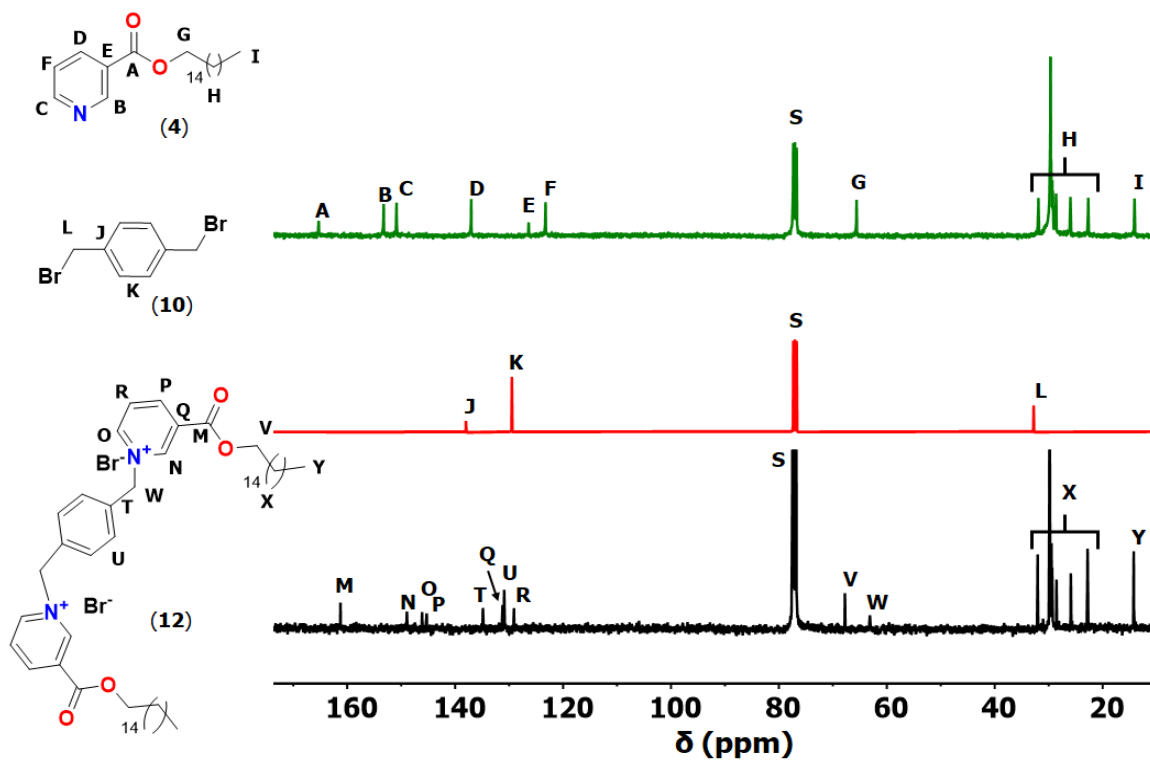
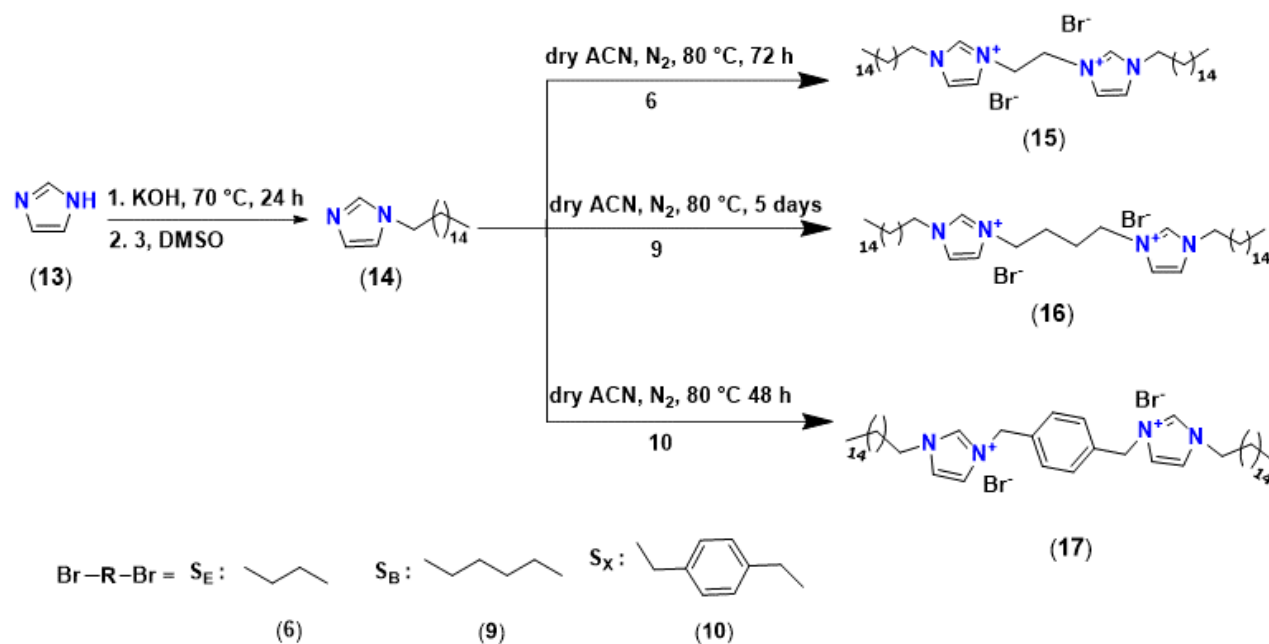


Figure 2.17.  $^{13}\text{C}$  NMR spectra of 4 (green trace), 10 (red trace) and 12 (black trace), S: solvent =  $\text{CDCl}_3$ .

## 2.2 Imidazolium-based Surfactants

The synthesis of imidazolium based GSs is described in **Scheme 2.8**. Starting with imidazole (**13**) activation by KOH, followed by the reaction with 1-bromohexadecane (**3**) in DMSO, which yielded the desired product 1-hexadecyl imidazole (**14**). The reaction of the latter with the dihalo species resulted in the target product.

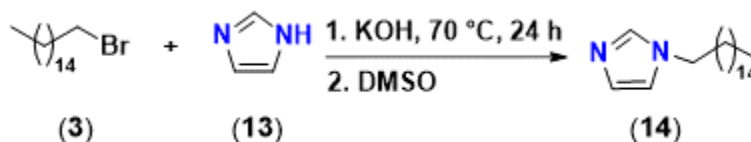


**Scheme 2.8.** Schematic representation for the synthesis of the imidazolium-based GSs; S<sub>E</sub>: Ethylene spacer (S<sub>E</sub>(Im<sup>+</sup>-C<sub>16</sub>)<sub>2</sub>•2Br, **15**). S<sub>B</sub>: Butylene spacer (S<sub>B</sub>(Im<sup>+</sup>-C<sub>16</sub>)<sub>2</sub>•2Br, **16**). S<sub>X</sub>: Xylenylene spacer (S<sub>X</sub>(Im<sup>+</sup>-C<sub>16</sub>)<sub>2</sub>•2Br, **17**).

### 2.2.1 Synthesis of 1-Hexadecylimidazole (**14**)

Following the procedure described by Izmaylov (Izmaylov, Di Gioia, Markova, Aloisio, Colonna, & Vasnev, 2015) *et al.*, the 1-Hexadecylimidazole (**14**) was synthesized with a slight modification. A solution of imidazole (**13**, 2.59 g, 38.0 mmol) in DMSO (100 mL) was stirred at RT under nitrogen atmosphere using a standard Schlenk line until homogenized and heated to 70 °C. Afterward, KOH (3.24 g, 57.9 mmol) was added to the previous solution and stirred for 30 min. followed by the dropwise addition of 1-bromohexadecane (**3**, 12.8 g, 41.8 mmol) under vigorous stirring over a period of 10 min. The reaction was left to stir for 24 h at 70 °C (**Scheme 2.9**). Upon completion of the duration, the reaction was cooled to RT, then 500 mL of distilled water (DW) was added to precipitate the 1-Hexadecylimidazole. The yellowish precipitate was filtered out, washed with (20 mL × 20) of DW, then dried in a vacuum oven for

2 h with a 92.2% yield Melting point (uncorrected) = 33 °C,  $^1\text{H NMR}$ : (500 MHz, DMSO- $d_6$ )  $\delta$  7.55 (s, 1H), 7.07 (d,  $J$  = 16.7 Hz, 1H), 6.82 (s, 1H), 3.88 (s, 2H), 1.63 (s, 3H), 1.18 (s, 24H), 0.80 (s, 3H).  $^{13}\text{C NMR}$ :  $^{13}\text{C NMR}$  (126 MHz, DMSO)  $\delta$  137.60, 128.68, 119.64, 46.39, 31.80, 31.07, 29.25 (d,  $J$  = 70.1 Hz), 26.40, 22.58, 14.37. **ATR-FTIR**: =C-H 3190  $\text{cm}^{-1}$ , -C-H 2850  $\text{cm}^{-1}$ , N=C 1460 and 1510  $\text{cm}^{-1}$ . **EA** ( $\text{C}_{19}\text{H}_{36}\text{N}_2 \cdot 0.3\text{H}_2\text{O}$ ; Calculated (%): C, 76.60; H, 12.38; N, 9.40 Found (%): C = 76.51, H = 11.0, N = 9.55. **HRMS** ( $m/z$  of  $[\text{C}_{19}\text{H}_{36}\text{N}_2 + \text{H}^+]$ , Calculated: 292.28785 Found: 293.29735).



**Scheme 2.9.** The synthesis of 1-Hexadecylimidazole **14**.

The ATR-FTIR spectrum as shown in **Figure 2.18**, which confirmed the preparation of **14** upon the emergence of two new peaks at 2852 and 2912  $\text{cm}^{-1}$  correlated to the aliphatic chain, combined with a C=N shift from 1530 and 1660  $\text{cm}^{-1}$  to 1460 and 1510  $\text{cm}^{-1}$ , respectively. Moreover, the disappearance of the N-H band at 3125  $\text{cm}^{-1}$  confirmed the coupling and the shifting for the =C-H to 3190  $\text{cm}^{-1}$ . (Nessim, Zaky, & Deyab, 2018) Further,  $^1\text{H NMR}$  shows two new peaks centered 6.82 and 7.07 ppm, accompanied with a slight upfield shift for the imidazole N=CH-N proton at 7.55 ppm. Moreover, a new peak emerged at 3.88 ppm associated with the formation of tertiary amine (**H**, **G**, **F** and **I**, black trace, **Figure S19**). (L. Wang, Liu, Huo, Deng, Yan, Ding, Zhang, Meng, & Lu, 2014).  $^{13}\text{C NMR}$  spectrum shows two new peaks corresponding to imidazolium base carbons centered at 122.0 ppm and 46.1 ppm that fortified the formation of tertiary amine (**H** and **I**, black trace, **Figure S20**). (M. Lee, Choi, Wi, Slebodnick, Colby, & Gibson, 2011).

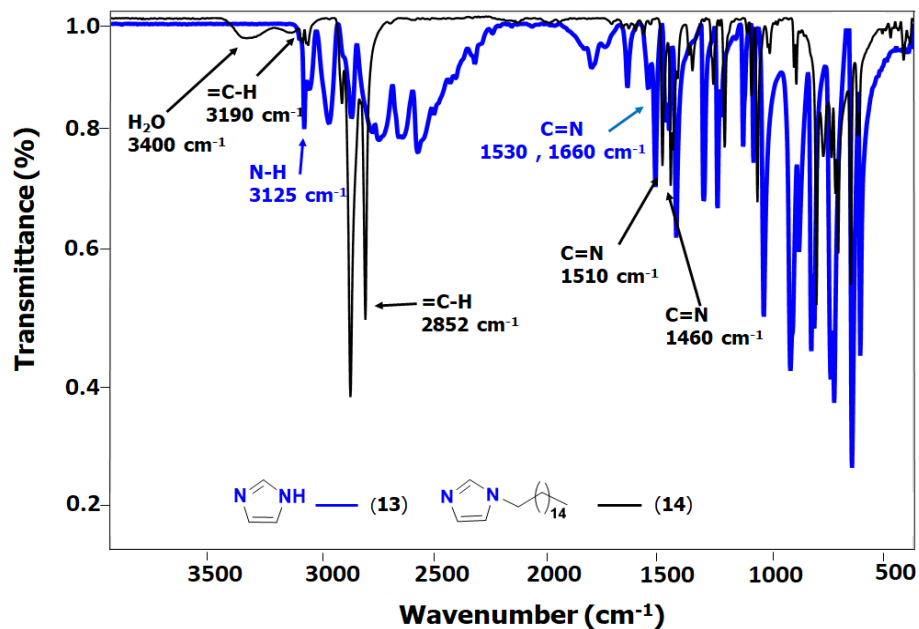


Figure 2.18. ATR-FTIR spectra of **13** (blue trace), and **14** (black trace).

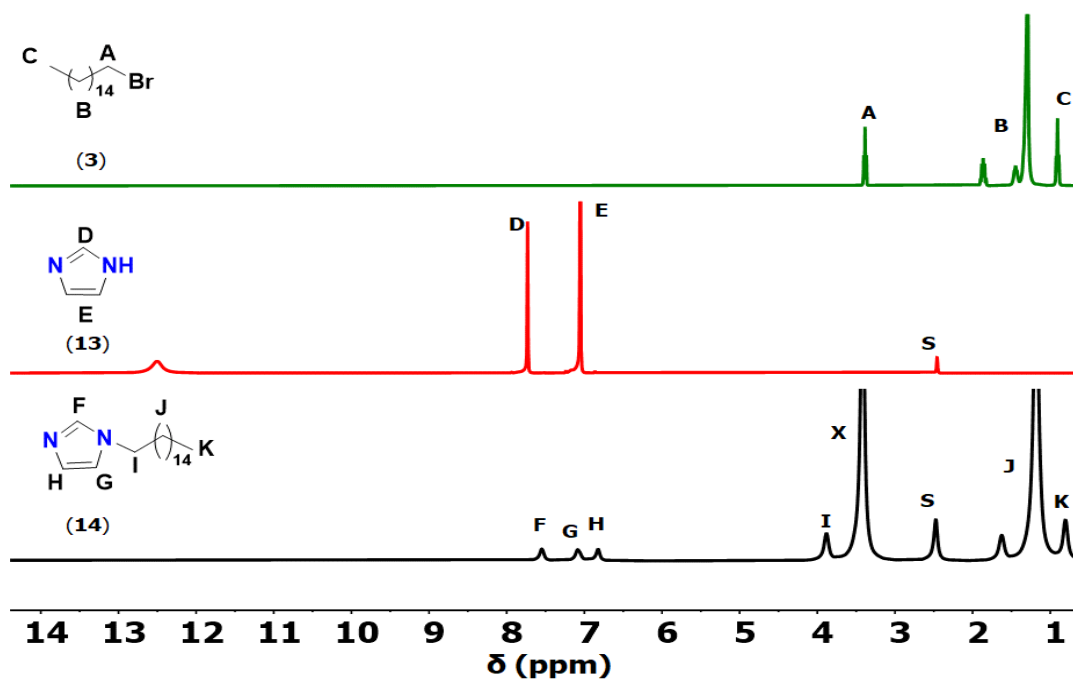
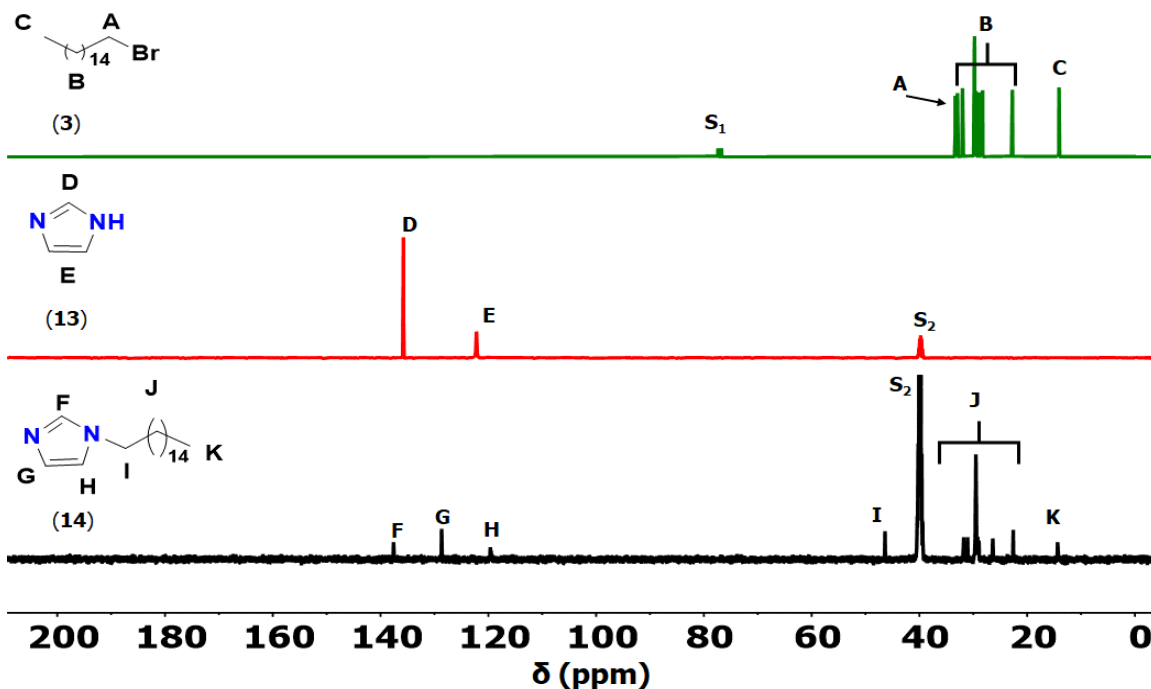


Figure 2.19.  $^1\text{H}$  NMR spectra of **3** (green trace, in  $\text{CDCl}_3$ ), **13** (red trace) and **14** (black trace), S =  $\text{DMSO-}d_6$ , X =  $\text{H}_2\text{O}$ .

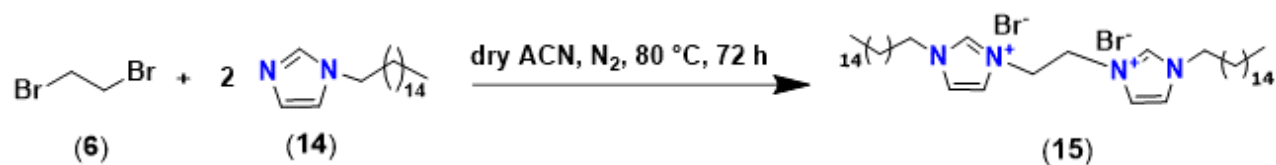


**Figure 2.20.**  $^{13}\text{C}$  NMR spectra of **3** (green trace,  $S_1 = \text{CDCl}_3$ ), **13** (red trace) and **14** (black trace),  $S_2 = \text{DMSO-}d_6$ .

### 2.2.2 Synthesis of 3,3'-(ethane-1,2-diyl)bis(1-hexadecyl-imidazol-3-ium) bromide ( $S_E(\text{Im}^+\text{C}_{16})_2\cdot 2\text{Br}$ , **15**)

The desired compound **15** was synthesized as described in **Scheme 2.10** as follows: In a 100 mL 3N round-bottomed flask, a solution of 1,2-dibromoethane (**6**, 0.513 mL, 5.95 mmol) in 10 mL dry ACN was prepared under nitrogen atmosphere using standard Schlenck line. Afterwards, dropwise-addition of 1-hexadecylimidazole (**14**, 3.50 g, 19.1 mmol) in 20 mL dry ACN to the previous solution with continuous stirring and refluxed in an oil bath at 80 °C for 72 h. Upon completion, the reaction was cooled to RT, and a yellowish precipitate was filtered out, washed with ACN (10 mL  $\times$  5), then dried in vacuum oven for 2 h with a yield of 72.7%. Melting point (uncorrected) = 240 °C,  $^1\text{H}$  NMR: (500 MHz,  $\text{CDCl}_3$ )  $\delta$  10.22 (s, 1H), 8.66 (s, 1H), 7.29 (s, 1H), 5.24 (s, 2H), 4.13 (t,  $J = 7.6$  Hz, 2H), 1.86 (t,  $J = 7.3$  Hz, 2H), 1.18 (s, 26H), 0.80 (t,  $J = 6.8$  Hz, 3H).  $^{13}\text{C}$  NMR: (126 MHz,  $\text{CDCl}_3$ )  $\delta$  136.63, 124.76, 121.43, 50.53, 48.00, 31.89, 30.04, 29.66, 29.62, 29.55, 29.45, 29.33, 28.89, 26.28, 22.66, 14.10. ATR-FTIR: ( $\text{N}^+\text{-CH}_2\text{CH}_2\text{N}^+$ ) 3030  $\text{cm}^{-1}$ ,  $\text{C=N}^+$  1550 and 1566  $\text{cm}^{-1}$ . EA ( $\text{C}_{40}\text{H}_{76}\text{N}_4\text{Br}_2$ ; Calculated (%): C, 62.16, H, 9.91, N, 7.25.

Found (%): C, 62.37, H, 9.90, N, 7.29). **HRMS** ( $m/z$  of  $[C_{25}H_{47}N_4]^+$ ), Calculated: 403.37952 Found: 403.29097).



**Scheme 2.10.** The synthesis of the ethylene-based GS,  $S_E(\text{Im}^+\text{-C}_{16})_2 \cdot 2\text{Br}$  (**15**).

The product **15** was examined by ATR-FTIR (**Figure 2.21**), which showed the emergence of a new peak at  $3030\text{ cm}^{-1}$  the alkylene group spacer  $S_E$ , *viz.*, ( $\text{N}^+\text{-CH}_2\text{CH}_2\text{N}^+$ ), and a shift in the  $\text{C}=\text{N}^+$  peak from 1460 and 1510 to  $1550$  and  $1566\text{ cm}^{-1}$ .(Shaheen, Mir, Arif, & Wani, 2020) For more evidence,  $^1\text{H}$  NMR was used (**Figure 2.22**), the spectrum showed shifting in the imidazolium group toward an upfield region 6.83-7.55 **B**, **C**, and **D** to 7.29-10.22 ppm **H**, **I**, and **J**. Moreover, the shifting of spacers hydrogen (**K**) up to 5.24 ppm as a result of quaternarization process.(Ren, Wang, Zhang, Nie, Li, & Cui, 2015) In addition,  $^{13}\text{C}$  NMR spectrum (**Figure 2.23**) support the formation of **15**, that the imidazolium carbon head experience an upfield shift from 137.5 to 136.6 ppm corresponding to **B** and **H**, respectively. This transformation is accompanied with another spacer carbon shift (**K**) centered at 50.5 ppm (Achour, Hamada, Baroudi, Abdelaziz, Rezazgui, & Trache, 2021).

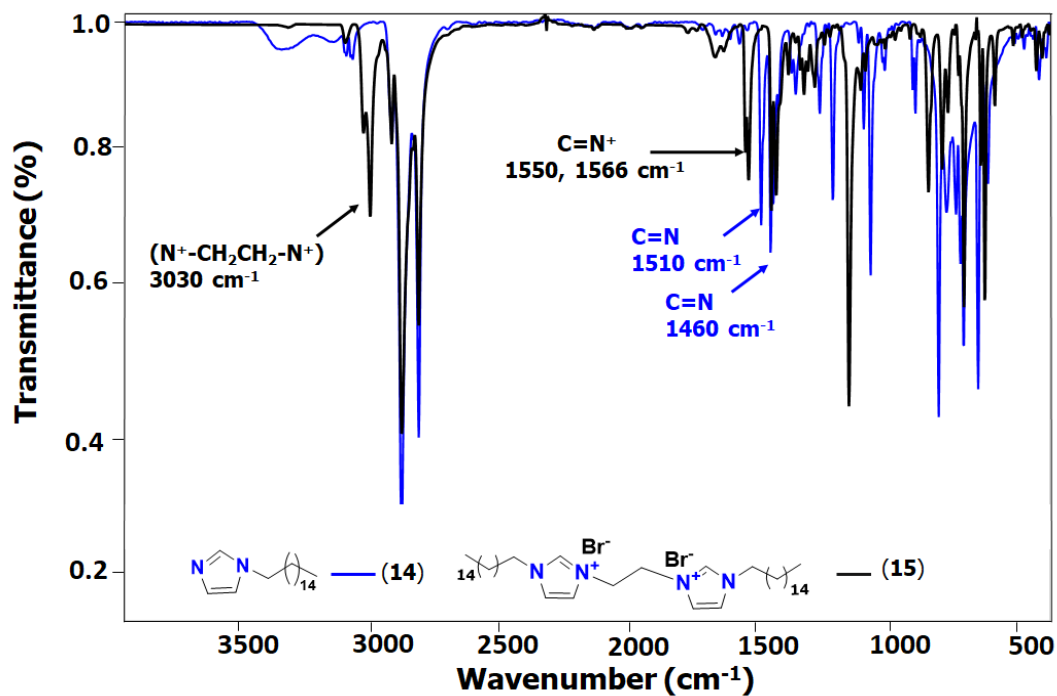


Figure 2.21. ATR-FTIR spectra of **14** (blue trace), and **15** (black trace).

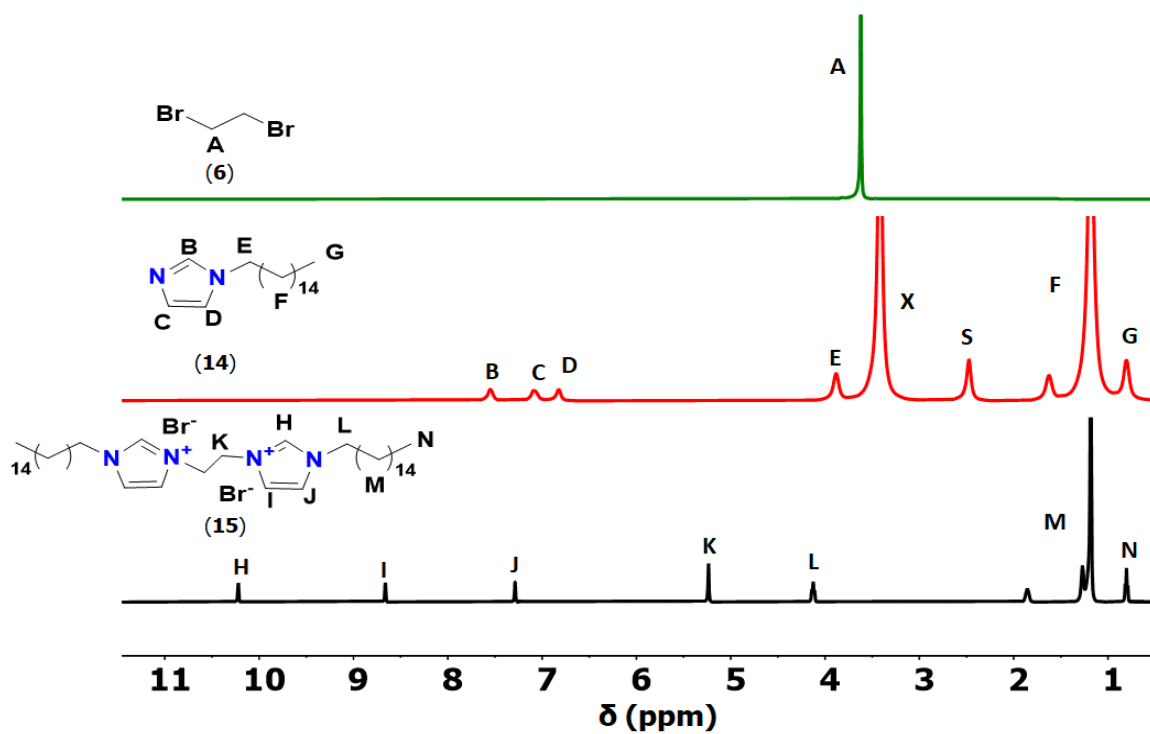
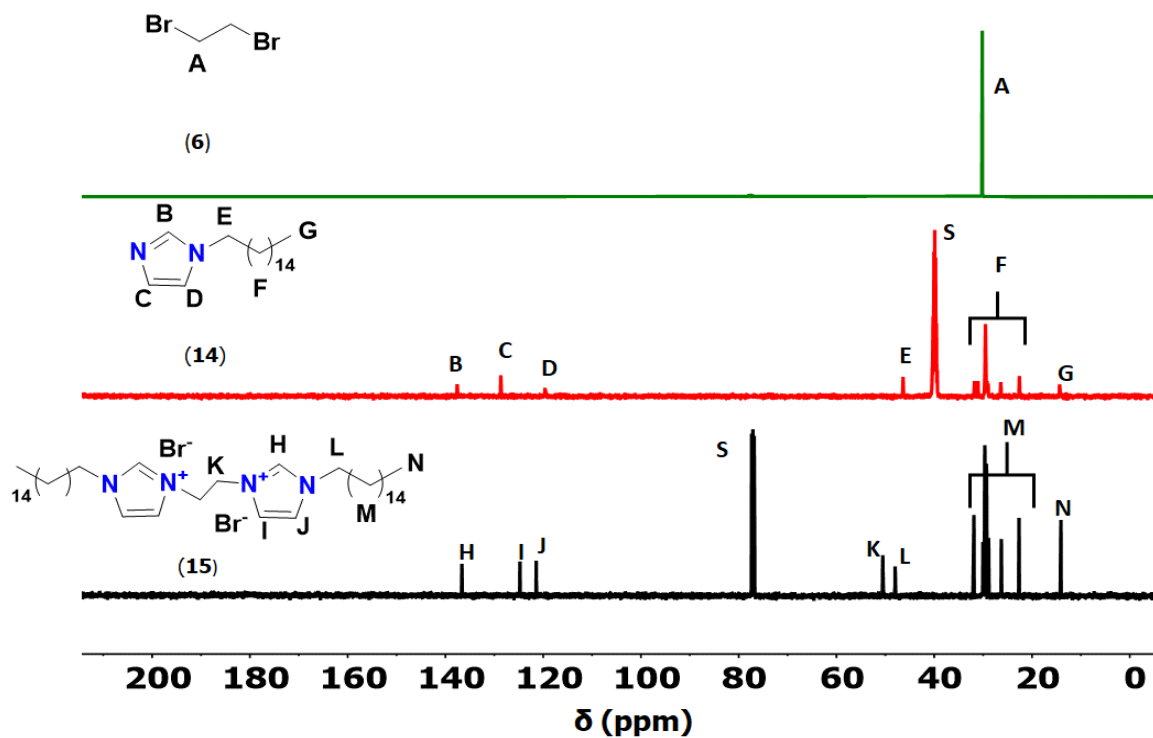


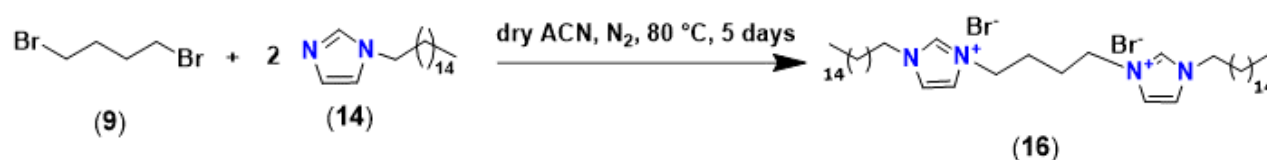
Figure 2.22.  $^1\text{H}$  NMR spectra of **6** (green trace, in  $\text{CDCl}_3$ ), **14** (red trace, **S** =  $\text{DMSO}-d_6$ , **X** =  $\text{H}_2\text{O}$ ), and **15** (black trace, in  $\text{CDCl}_3$ ).



**Figure 2.23.**  $^{13}\text{C}$  NMR spectra of **6** (green trace, in  $\text{CDCl}_3$ ), **14** (red trace, S =  $\text{DMSO-}d_6$ ), and **15** (black trace, in  $\text{CDCl}_3$ ).

### 2.2.3 Synthesis of 3,3'-(butane-1,4-diyl)bis(1-hexadecyl-imidazol-3-ium) bromide ( $S_B(\text{Im}^+-\text{C}_{16})_2\cdot 2\text{Br}$ , **16**)

Using standard Schlenck line, under nitrogen atmosphere, a solution of 1-hexadecylimidazole (**14**, 2.50 g, 8.54 mmol) in 15 mL dry ACN was dropwise-added to a solution of 1,4-dibromobutane (**9**, 0.508 mL, 4.27 mmol) prepared in 15 mL dry ACN within a 3N, 100-mL, round-bottomed flask under continuous stirring and refluxed in an oil bath at 80 °C for 5 days. Afterwards, the reaction was cooled to RT, and a yellowish precipitate was filtered out, washed with ACN (10 mL  $\times$  5), then dried in vacuum oven for 2 h with 68% yield (**Scheme 2.11**) (uncorrected) = 215 °C.  $^1\text{H}$  NMR: (500 MHz, DMSO)  $\delta$  9.44 (d,  $J = 7.3$  Hz, 1H), 7.85 (s, 1H), 7.82 (s, 1H), 4.23 (s, 2H), 4.14 (t,  $J = 7.3$  Hz, 2H), 3.29 (s, 2H), 1.84 – 1.70 (m, 4H), 1.18 (s, 21H), 0.79 (t,  $J = 6.3$  Hz, 3H).  $^{13}\text{C}$  NMR: (126 MHz, DMSO- $d_6$ )  $\delta$  136.58, 122.95, 122.89, 49.32, 48.43, 31.79, 29.82, 29.57, 29.36, 29.21, 28.91, 26.49, 26.04, 22.58, 14.39. ATR-FTIR: ( $\text{N}^+(\text{CH}_2)_4\text{N}^+$ ) 3050  $\text{cm}^{-1}$ ,  $\text{C}=\text{N}^+$  1555  $\text{cm}^{-1}$ . EA ( $\text{C}_{42}\text{H}_{80}\text{N}_4\text{Br}_2$ ; Calculated (%): C, 62.98, H, 10.07, N, 7.00. Found (%): C, 62.72, H, 9.86, N, 6.98). HRMS ( $m/z$  of [ $\text{C}_{42}\text{H}_{80}\text{N}_4^{+2}+\text{H}^+$ ], Calculated: 798.47497 Found: 799.61132).



**Scheme 2.11.** The synthesis of butylene-based GS,  $S_B(\text{Im}^+-\text{C}_{16})_2\cdot 2\text{Br}$  (**16**).

The formation of **16** was confirmed using ATR-FTIR,  $^1\text{H}/^{13}\text{C}$  NMR spectroscopies. as shown in **Figure 2.24**, a new peak centered at 3050  $\text{cm}^{-1}$  corresponding to the alkylene group spacer  $S_B$ , viz., ( $\text{N}^+(\text{CH}_2)_4\text{N}^+$ ) was observed. this was associated with a blue shift of the wavenumber value regarding  $\text{NCN}^+$  moiety from 1460 as well as 1510 up to 1555  $\text{cm}^{-1}$  (Shaheen *et al.*, 2020). In addition,  $^1\text{H}$  NMR spectra (**Figure 2.25**) the peaks belong to the imidazolium ring shifted to an upfield region (6.83-7.55 **C**, **D** and **E**) to (7.84-9.45 ppm **I**, **J**, and **K**) accompanied with an downfield shift of **L** and **N** to 4.23 and 3.29 ppm (black trace) for the  $S_B$  spacer. **Figure 2.26** fortified the presumed structure as well with an upfield shift in the imidazolium ring carbon from 137.5 to 136.5 ppm representing **C** and **I**, respectively. Additionally, a peak centered at 49.3 ppm related to **L** upon the quaternarization process (Achour *et al.*, 2021).

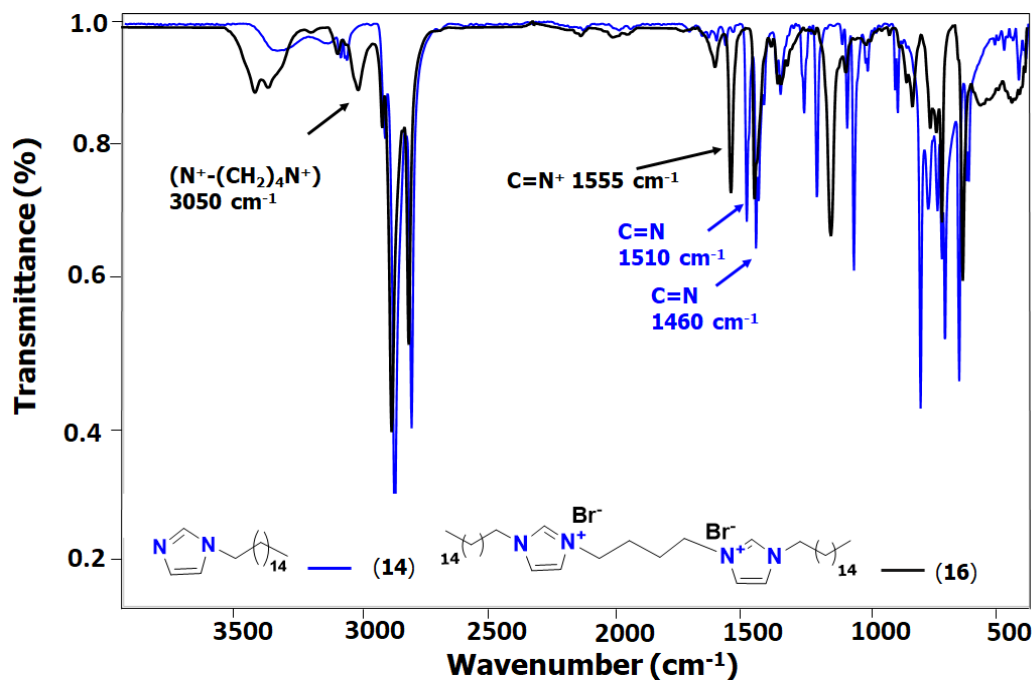


Figure 2.24. ATR-FTIR spectra of **14** (blue trace), and **16** (black trace).

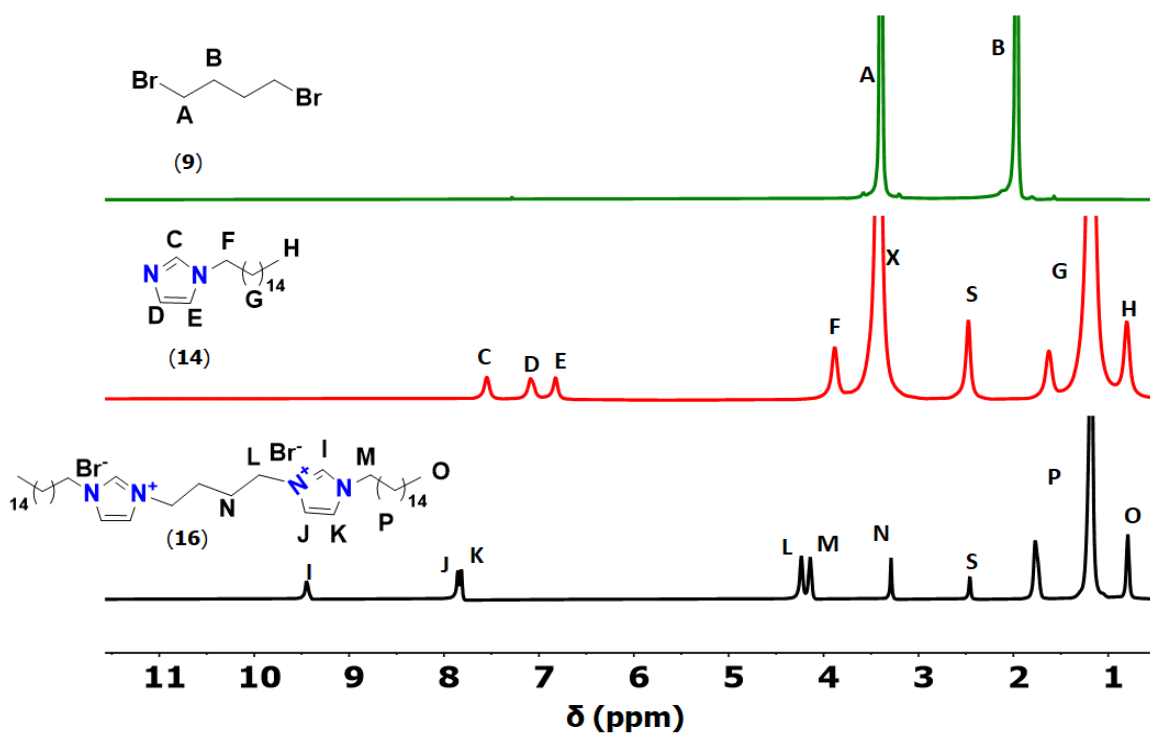
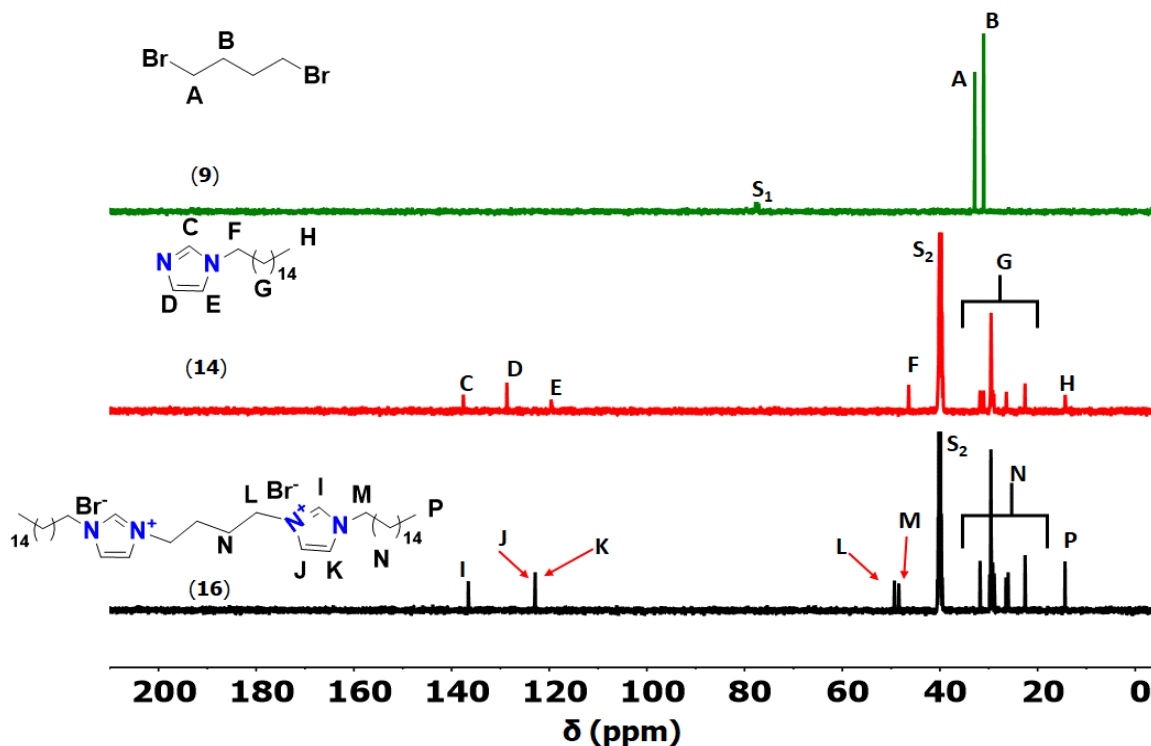


Figure 2.25.  $^1\text{H}$  NMR spectra of **9** (green trace, in  $\text{CDCl}_3$ ), **14** (red trace), and **16** (black trace), S =  $\text{DMSO-}d_6$ , X =  $\text{H}_2\text{O}$ .

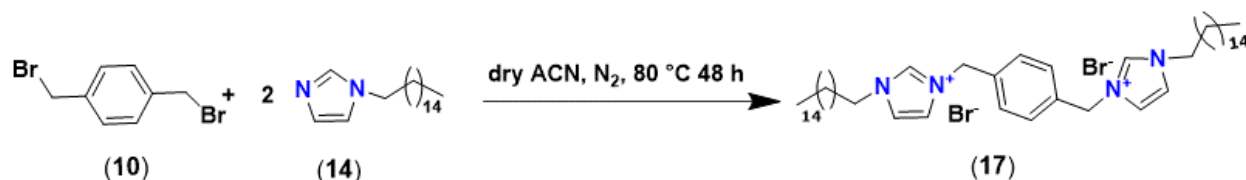


**Figure 2.26.**  $^{13}\text{C}$  NMR spectra of **9** (green trace,  $S_1 = \text{CDCl}_3$ ), **14** (red trace), and **16** (black trace),  $S_2 = \text{DMSO-}d_6$

#### 2.2.4 Synthesis of 3,3'-(1,4-phenylenebis(methylene)) bis (1-hexadecyl-imidazole-3-ium-bromidee) ( $S_x(\text{Im}^+-\text{C16})_2 \cdot 2\text{Br}$ , **17**)

Product **17** (Scheme 2.12) was prepared with slight modifications according to a literature procedure by Amirthalingam *et al.* (Amirthalingam, Rodrigues, Casal-Dujat, Calpena, Amabilino, Ramos-López, & Pérez-García, 2015) as follows: In a 3N, 100-mL, round-bottomed flask,  $\alpha,\alpha'$ -Dibromo-*p*-xylene (**10**, 0.67 g, 25.6 mmol) dissolved in 15 mL dry ACN, under nitrogen atmosphere using standard Schlenck line. Afterwards, a dropwise addition of a 15 mL solution of 1-hexadecylimidazole (**3**, 1.50 g, 51.3 mmol) in dry ACN to the previous solution at 80 °C with continuous stirring and refluxed in an oil bath for 48 h. After cooling the reaction to RT, the white precipitate was filtered out, washed with ACN (10 mL  $\times$  5), then dried in vacuum oven for 2 h with a yield of 64.5%. Melting point (uncorrected) = 190 °C.  $^1\text{H}$  NMR: (500 MHz,  $\text{CDCl}_3$ )  $\delta$  10.21 (s, 2H), 7.88 (s, 2H), 7.45 (s, 4H), 7.36 (s, 2H), 5.63 (s, 4H), 4.24 (s, 4H), 1.83 (s, 4H), 1.26 (s, 4H), 1.20 (s, 48H), 0.83 (s, 6H).  $^{13}\text{C}$  NMR: (126 MHz,  $\text{CDCl}_3$ )  $\delta$  136.50, 134.45, 130.06, 123.17, 121.91, 52.32, 50.19, 31.92, 30.34, 29.70, 29.67, 29.66, 29.63, 29.55, 29.41, 29.36, 29.03, 26.31, 22.68, 14.11. ATR-FTIR:  $[(\text{C}_6\text{H}_4)-(\text{CH}_2\text{N}^+)]_2$ : 3030  $\text{cm}^{-1}$ ,  $\text{C}=\text{N}^+$ : 1560  $\text{cm}^{-1}$ . EA ( $\text{C}_{46}\text{H}_{80}\text{N}_4\text{Br}_2$ ;

Calculated (%): C, 65.08, H, 9.50, N, 6.60. Found (%): C, 65.08, H, 9.64, N, 6.74). **HRMS** ( $m/z$  of  $[C_{23}H_{40}N_2^+]$ , Calculated: 344.31860 Found: 344.32148).



**Scheme 2.12.** The synthesis of p-xylylene-based GS,  $S_x(\text{Im}^+\text{-C}_{16})_2 \cdot 2\text{Br}$  (**17**).

The structure of **17** was examined using ATR-FTIR and  $^1\text{H}/^{13}\text{C}$  NMR. The ATR-FTIR shown in **Figure 2.27** revealed a new peak centered at  $3030\text{ cm}^{-1}$  corresponding to the xylylene spacer;  $S_x$ , *viz.*,  $[(\text{C}_6\text{H}_4)\text{-(CH}_2\text{N}^+)_2]$  was observed. This is verified by C=N blue-shifting from  $1460$  as well as  $1510\text{ cm}^{-1}$  to  $1560\text{ cm}^{-1}$  (Nessim *et al.*, 2018). The NMR spectrum verified the presumed structure upon assigning the methylene moiety within the rigid spacer related to **M** centered at  $5.62\text{ ppm}$  (**Figure 2.28**, black trace) corresponding to **J**  $52.3\text{ ppm}$  (**Figure 2.29**, black trace) as a result of quaternarization (Casal-Dujat, Rodrigues, Yagüe, Calpena, Amabilino, González-Linares, Borràs, & Pérez-García, 2012).

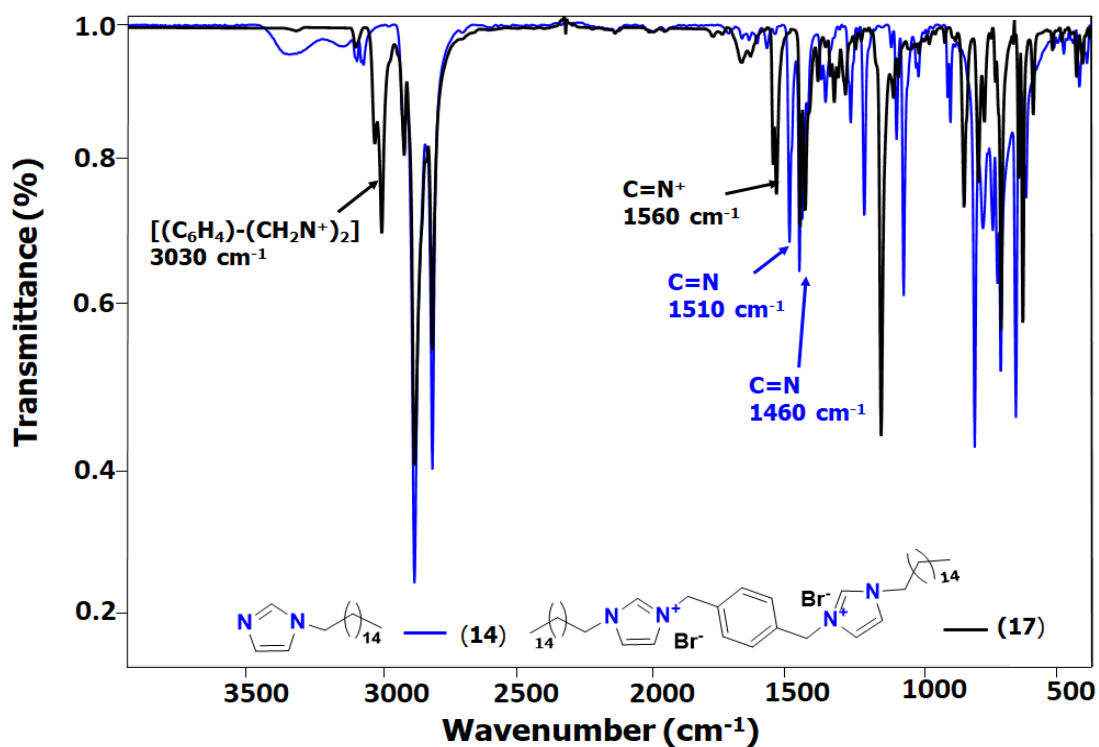


**Figure 2.27.** ATR-FTIR spectra of **14** (blue trace), and **17** (black trace).

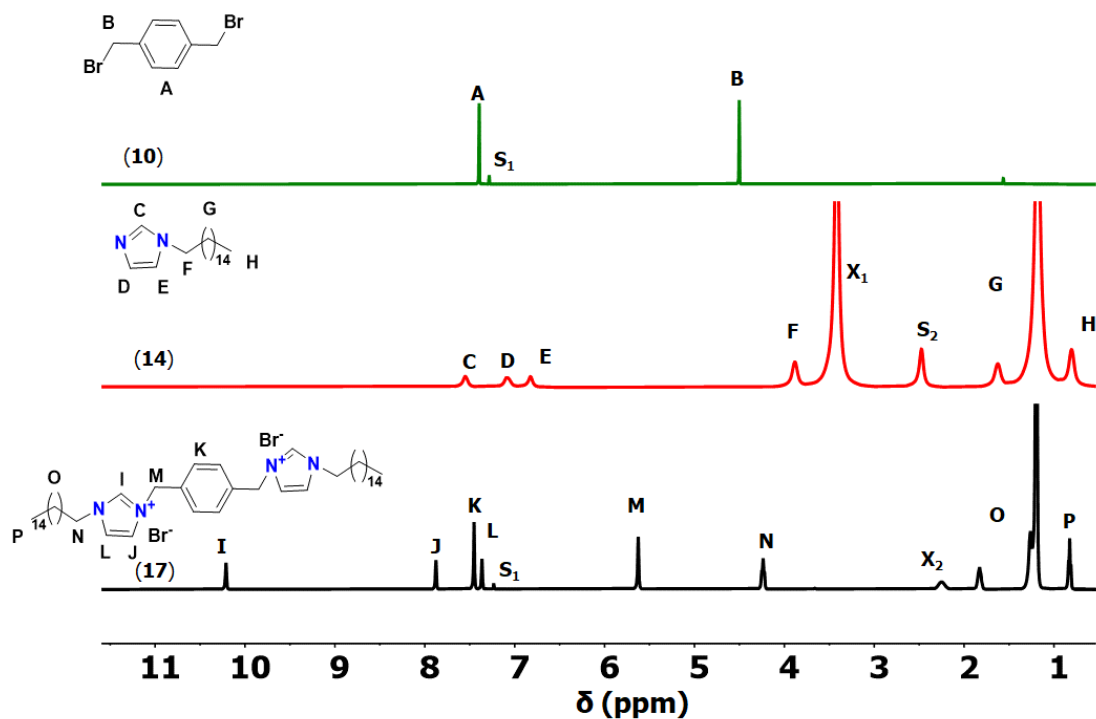


**Figure 2.28.**  $^1\text{H}$  NMR spectra of **10** (green trace,  $S_1 = \text{CDCl}_3$ ), **14** (red trace,  $S_2 = \text{DMSO}-d_6$ ,  $X_1 = \text{H}_2\text{O}$ ), and **17** (black trace,  $S_1 = \text{CDCl}_3$ ,  $X_2 = \text{ACN}$ ).

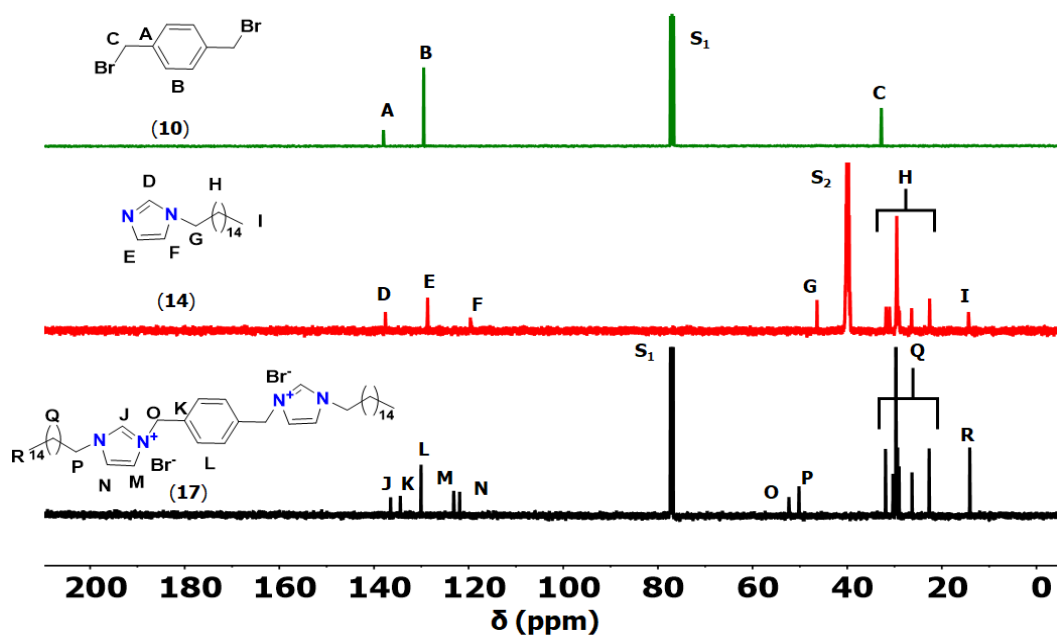


**Figure 2.29.**  $^{13}\text{C}$  NMR spectra of **10** (green trace,  $S_1 = \text{CDCl}_3$ ), **14** (red trace,  $S_2 = \text{DMSO}-d_6$ ), and **17** (black trace,  $S_1 = \text{CDCl}_3$ ).

### 2.3 Instruments

$^1\text{H}$  and  $^{13}\text{C}$  nuclear magnetic resonance (NMR) spectroscopy were measured at room temperature using a 400 MHz FTNMR NanoBay spectrometer together with 500 MHz AVANCE-III NMR (Bruker, Switzerland). *Ex situ* ATR-FTIR spectra were recorded using a Bruker Vertex 70-FT-IR spectrometer at room temperature coupled with a Vertex Pt-ATR-FTIR accessory (Bruker, Switzerland). Elemental analysis was completed by an EA3000 (Eurovector, Italy). While uncorrected melting point was measured using an SMP1 (Stuart Scientific, United Kingdom). High-Resolution Mass Spectra (HRMS) were measured (in either positive or negative ion modes) using electrospray ion trap (ESI) technique by collision-induced dissociation on a Bruker APEX-IV (7 Tesla) instrument. The samples were dissolved in  $\text{CHCl}_3$  and ACN and infused using a syringe pump with a flow rate of  $120 \mu\text{L min}^{-1}$ . External calibration was conducted using arginine cluster in a mass range  $m/z$  175-871. Mass error: 0.00-0.50 ppm.

### 2.4 Chemicals

All chemicals were used without further purification and are commercially available, nicotinic acid (NA, **1**, 98%), 1-bromohexadecane (**3**, 97%), 1,4-dibromobutane (**9**, 99%),  $\alpha, \alpha'$ -dibromo-*p*-xylene (**10**, 97%), imidazole (**13**, 99%), dimethyl sulfoxide- $d_6$  (DMSO- $d_6$ , 99.5 + % atom D), deuterium oxide ( $\text{D}_2\text{O}$ , 99.9 % atom D), ethanol- $d_6$  (EtOD, 99.5 % atom D), and chloroform- $d$  ( $\text{CDCl}_3$ , 99.8 % atom D) were purchased from Sigma Aldrich. 1-Bromoethane (**5**, 99 %) and 1,2-Dibromoethane (**6**, 98%) were obtained from Ridel-de Haen and Fluka Analytical, respectively. Potassium hydroxide (pellets) was obtained from Fisher. Diethyl ether ( $\text{Et}_2\text{O}$ ) and methanol (HPLC grade) were acquired from Biochem. Dimethyl sulfoxide (DMSO, HPLC grade), isopropanol (HPLC grade), toluene (RG), hexane (RG), and chloroform ( $\text{CHCl}_3$ , HPLC grade) were obtained from TEDIA. Acetonitrile (ACN, HPLC grade) was purchased from Anquan Chemicals Supply. Unless otherwise stated, dry ACN (HPLC grade) was purchased from SDFCL Sd Fine Chem Limited, desiccated, and distilled over  $\text{MgSO}_4$ , and kept under nitrogen  $\text{N}_2$  gas (industrial grade) was purchased from Advanced Technical Gases Co. (Amman, Jordan).

## Chapter 3

### Interfacial Behavior of modified Nicotinic acids as Conventional/Gemini Surfactants

This chapter is a verbatim copy of a paper published in ACS Langmuir. [Reprinted with permission from Langmuir, 2022, 38, 28, 8524–8533. Copyright 2022 American Chemical Society.]

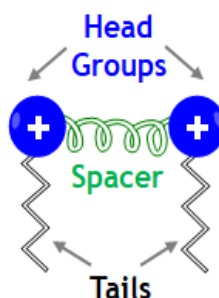
#### 3.1 Abstract

We report the synthesis and monolayer properties of conventional and gemini surfactants comprised of nicotinic acid-based head groups with an emphasis on assessing how chemical structures affect the behavior of monolayers. A combination of Brewster angle microscopy and atomic force microscopy showed that pure hexadecyl nicotinate formed rippled strands in monolayers, and the gemini correspondents with either flexible or rigid organic linkers resulted in lobed-compact domains, which provides a simple method for patterning air-water and solid-air interfaces. The structural differences between conventional and gemini nicotinic acid-based surfactants could be explained by the interplay between line tension (that favors the formation of circular domains), balanced by dipole-dipole repulsion interaction between headgroups, which promote extended domains. Miscibility and morphology studies of the modified nicotinic acid surfactants with palmitic acid demonstrated that the properties of mixed films can be controlled by the structure of the former. Excess Gibbs free energies of mixing indicated that the mixed films are less stable than the pure monolayers, and the positive deviations from ideality were the largest in the case of the gemini surfactant.

#### 3.2 Introduction

Since the pioneering work of Bunton group (Bunton *et al.*, 1971) on using dicationic ammonium detergents for catalytic applications, cationic gemini surfactants (GSs, **Scheme 3.1**) (F. M. Menger & Littau, 1991, 1993) have gained interest within the research community because of their excellent performance characteristics in terms of lowering surface tension, small critical micelle concentration (CMC), unique rheological properties and excellent adsorption on solid surfaces. These characteristics make GSs potential candidates for a broad range of applications ranging from cleaning agents, (Kumar & Tyagi, 2014) oil recovery, (Hou, Jia, Fu, Wang, Ma, Jiang, & Yang, 2019) corrosion inhibitors (Pakiet, Tedim, Kowalczyk, & Brycki, 2019) drugs (Rajput, Mondal, Kuddushi, Jain, Ray, Aswal, & Malek, 2020) and gene delivery (Costa, Oliveira, Silva, Silva, Botelho, do Vale, Real Oliveira, Gomes, & Marques,

2021). For detailed information about the classification, synthesis, physicochemical properties and prospective aspects of GSs, readers are directed to the review by Sharma *et al.* (Sharma, Kamal, Abdinejad, Mahajan, & Kraatz, 2017b)



**Scheme 3.1.** Schematic illustration of a positively charged GS. The physicochemical properties of these surfactants depend on the flexibility/rigidity of the spacer, the length of the tails and the chemical identity of the headgroups.

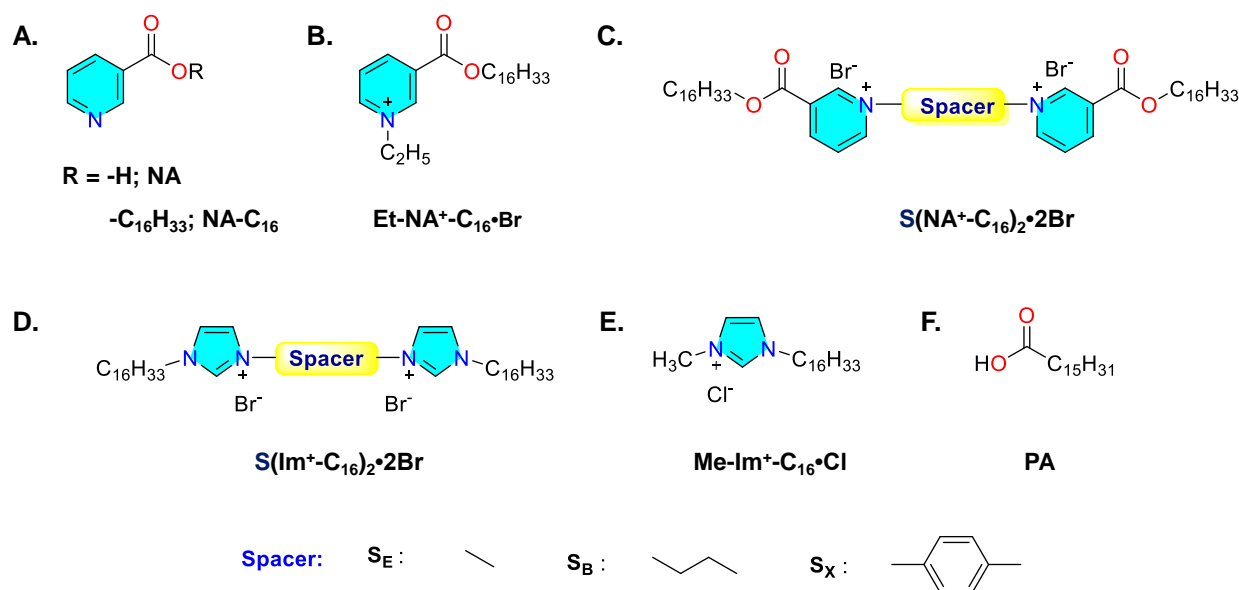
There is growing interest in the use of ecologically “friendly” chemical building blocks in the preparation of synthetic surfactants to mitigate any toxicity for medicinal and pharmaceutical applications, (Johnsson & Engberts, 2004; Yoshimura, Ishihara, & Esumi, 2005; Scarzello, Klijn, Wagenaar, Stuart, Hulst, & Engberts, 2006; Silva, Alves, Cardoso, Jurado, Pedroso de Lima, Vale, & Marques, 2013; A. Pinazo, Manresa, Marques, Bustelo, Espuny, & Pérez, 2016; Anchev, Tsekova, Mircheva, & Grozev, 2019) and to fully realize the potential of GSs for these applications, this issue needs to be considered. An important class of compounds which show excellent surface activity are the pyridinium based-GSs (dialkylviologens), which were first synthesized as part of studies aimed at exploring photoreduction from micellar counterions. (D. K. Lee, Kim, Kwon, Kang, & Kevan, 1997b) However, the synthesis of these compounds can be challenging and is generally not ecologically benign. Furthermore, there is a very limited understanding of how chemical structure of the surfactant impacts the basic physical chemical properties of the resulting monolayers. Nicotinic acid (NA, **Scheme 3.2A**), a relatively low-cost natural product, (Aldrich, 2022; TCI Chemical, 2022) and its esters (nicotinate)s (Gunderson, 1943; Kaufman, 1945; Badgett, Provost, Ogg, & Woodward, 1945) present a particularly intriguing opportunity for accessing improved synthetic routes to surfactants. NA has potential for use to alleviate lung injury and prevent/lower the risk of cardiovascular heart disease and for cancer treatment. (Girgis, Kalmouch, & Ellithey, 2006; He, He, Khoshaba, Lu, Cai, Zhou, Liao, & Cao, 2019; Lehmler, Xu, Vyas, Ojogun, Knutson, & Ludewig, 2008) Nicotinate esters bearing hydrogenated, fluorinated or semifluorinated alkyl chains are putative prodrugs with enhanced pharmacokinetics and

better solubility in non-polar pulmonary drug delivery vehicles in comparison with the parent molecule.(Ojogun, Knutson, Vyas, & Lehmler, 2010)

The use of NA can be viewed as a transition towards implementing nontoxic, environmentally benign materials for medicinal applications. This approach agrees well with the “Green Chemistry Principles” set in the late 1990’s, (P. T. Anastas & Warner, 2000) which establishes a framework for making more benign chemicals and processes. In this work, we report the synthesis and characterization of nicotinate esters (NA-C<sub>16</sub> and Et-NA<sup>+</sup>-C<sub>16</sub>•Br) and their corresponding NA-based GSs (S(NA-C<sub>16</sub>)<sub>2</sub>•2Br, **Scheme 3.2A-C**). The design of our surfactants (**Scheme 3.2C**) takes into consideration the following: (1) incorporation of a biorenewable pyridine nucleus; (2) inclusion of an ester linkage within the structural motif and (3) the use of flexible (ethylene and butylene) or rigid (*p*-xylylenyl) spacers. Intuitively, the use of a non-fossil fuel feedstock is necessary to achieve greener substances.(P. Anastas & Eghbali, 2010) Moreover, pyridinium-based ionic liquids bearing an ester side chain showed remarkable biodegradability under aerobic conditions in comparison with linear alkyl chains.(Harjani, Singer, Garcia, & Scammells, 2008) Furthermore, the self-assembly of GSs at air-water and air-solid interfaces is directed by controlling the spacer length, hydrophobicity and flexibility.(Han, Xu, Liu, & Hu, 2005; M. Zhou, Liu, Yang, Liu, Zhang, & Hu, 2006; R. Li, Chen, Liu, & Hu, 2010; Mivehi, Bordes, & Holmberg, 2011) Notably, the permanent charge of the synthesized surfactants makes them insensitive to *pH* changes and suitable for many applications.

The interfacial properties of these surfactants were investigated in monolayers at the air-water interface and compared with their imidazolium analogues (S(Im<sup>+</sup>-C<sub>16</sub>)<sub>2</sub>•2Br and Me-Im<sup>+</sup>-C<sub>16</sub>•Cl, **Scheme 3.2D-E**) to examine the effect of head group structural differences on the packing of the resulting monolayer films, while holding the same spacer/tail arrangement within the heterocyclic ring.

For most medicinal applications, surfactants can reasonably be expected to be used as mixtures (*e.g.*, lung surfactant mixtures, mixed micelles in drug delivery), and thus, the mixing behavior of new, NA-based surfactants in monolayers is also of significant interest. Thus, the interfacial mixing of the pyridinium surfactants was examined in the presence of palmitic acid (PA, **Scheme 3.2F**), which was chosen previously as a suitable candidate to model, understand and probe interfacial properties of biological membranes.(Sah & Kundu, 2020; Sthoer & Tyrode, 2019; Sung, Krem, & Kim, 2018)



**Scheme 3.2.** The chemical structure of: **A.** Pyridine-3-carboxylic acid (Nicotinic acid, NA; R = -H)/Hexadecyl nicotinate (NA- $C_{16}$ ; R = - $C_{16}H_{33}$ ), **B.** 1-ethyl-3-((hexadecyloxy)carbonyl)pyridin-1-ium bromide Et-NA<sup>+</sup>- $C_{16}$ •Br, **C.** 1,1'-(spacer)bis(3-((hexadecyloxy)carbonyl)pyridin-1-ium) bromide (S(NA<sup>+</sup>- $C_{16}$ )<sub>2</sub>•2Br), **D.** 3,3'-(spacer)bis(1-hexadecyl-1H-imidazol-3-ium) bromide (S(Im<sup>+</sup>- $C_{16}$ )<sub>2</sub>•2Br), **E.** 1-hexadecyl-3-methyl-1H-imidazol-3-ium chloride (Me-Im<sup>+</sup>- $C_{16}$ •Cl) and **F.** Palmitic acid (PA).

### 3.3 Results and Discussion

**Figure 3.1** shows the  $\pi$ - $A$  isotherms of hexadecyl nicotinate esters (including both neutral NA- $C_{16}$ , positively charged Et-NA<sup>+</sup>- $C_{16}$  and S(NA- $C_{16}$ )<sub>2</sub> measured at 25 °C using a Milli-Q water subphase. The isotherm of NA- $C_{16}$  is consistent with that reported previously by the Lehmler group.(Lehmler, Fortis-Santiago, Nauduri, & Bummer, 2005b) It exhibits characteristic liquid-expanded (LE) and liquid-condensed (LC) phases, with the onset of the phase transition at  $\sim \pi = 5$  mN/m and a collapse pressure at  $\sim \pi = 35$  mN/m. The limiting molecular area ( $A_0$ ) estimated by extrapolating the linear segment of the LC phase to zero surface pressure is  $\sim 31.5$  Å<sup>2</sup>/molecule. It is noteworthy that the previously reported  $A_0$  ( $26.2 \pm 1$  Å<sup>2</sup>/molecule measured using HCl subphase, pH 1.9–2.1) is smaller in comparison with our estimated value, though we note that monolayer packing in this system is strongly sensitive to pH as  $pK_b$  of pyridine is 8.8. (Dewick, 2013) To understand the impact of quaternization on the nicotinate ester headgroup, the isotherm of (Et-NA<sup>+</sup>- $C_{16}$ •Br, **Scheme 3.2B**) was examined. It shows a single smooth curve with a maximum surface pressure and  $A_0$  values of *ca.* 1.7 mN/m and 22 Å<sup>2</sup>/molecule, respectively. The recorded  $A_0$  indicates that Et-NA<sup>+</sup>- $C_{16}$ •Br forms a relatively stable film at the air-water interface under the explored conditions. The stability of the monolayer was determined by measuring how the barrier position is

changed as a function of time before transferring the surfactant film into a solid substrate. Compressing the surfactant film to  $\pi = 1$  mN/m, the barriers are contract over a few millimeters to maintain constant surface pressure over the time course of 5 min, which suggests there is a slow dissolution of the surfactant into the subphase. While we have estimated the CMC of Et-NA<sup>+</sup>-C<sub>16</sub>•Br at  $\sim 0.24$  mM using a Wilhelmy plate force tensiometer (**Figure A.1**), it cannot be determined for NA-C<sub>16</sub> because of solubility limitations in the aqueous media.

The isotherms of S(NA<sup>+</sup>-C<sub>16</sub>)<sub>2</sub> are substantially expanded in comparison with the film of NA-C<sub>16</sub>, with a collapse plateau ranging between  $\pi = 55 - 58$  mN/m. The more expanded monolayer of GSs is correlated with the density functional theory (DFT)-optimized surfactant structures in the gas phase (**Figure A.2**). While the area of the latter is  $34 \text{ \AA}^2/\text{molecule}$ , it ranges between  $66-108 \text{ \AA}^2/\text{molecule}$  for the NA-based GSs. The isotherms of surfactants with butylene and xylenyl spacers show a kink at *ca*  $\pi = 45$  mN/m. Although it is not clear in the case of S<sub>E</sub>(NA<sup>+</sup>-C<sub>16</sub>)<sub>2</sub>, compressional modulus analysis indicates a minimum at *ca.* 48.5 mN/m, which corresponds to the kink feature (**Figure A.4**). Notably, the position of the LE-LC phase change and the kinks (which are ranging between 1-2 mN/m) are different for both pure NA-C<sub>16</sub> and the gemini correspondents, and the extent of the difference is affected by the linker length. It is anticipated that the recorded kinks corresponding to the formation of more ordered, highly packed film in comparison with the LC phase, as deduced from the Brewster angle microscopy (*vide infra*). Moving from ethylene to butylene spacer, the isotherm is shifted to smaller mean molecular area, while that of the xylenyl resides between the former two. This suggests that the spacers have a significant role in controlling structure of the molecules at the interface. We postulate that the two-carbon spacer takes on a more extended conformation to minimize the electrostatic repulsion between the two cationic head groups, and the hydrophobic interactions between the tails dominates for longer flexible or rigid spacers. (Datta, Biswas, & Bhattacharya, 2014b) CMC values for S(NA<sup>+</sup>-C<sub>16</sub>)<sub>2</sub>•2Br could not be determined because of their insolubility in water.

To understand the impact of the ester linkage on the surface properties of the synthesized surfactants, we have replaced the pyridinium with an imidazolium ring while keeping the same substituent spacing intact. Consistent with our previous measurements, Me-Im<sup>+</sup>-C<sub>16</sub>•Cl (**Figure 2.1B**) does not form a stable monolayer as inferred from the extremely low  $A_0$  value, (A. F. Eftaiha, Qaroush, Kayed, Abdel Rahman, Assaf, & Paige, 2020b) and a CMC at  $\sim 0.82$  mM (**Figure A.3A**). We have reported previously on small  $A_0$  values for a series of 1-alkyl-3-methyl imidazolium chloride monolayers ranging between  $6.7-11.0 \text{ \AA}^2/\text{molecule}$ . (A. F. Eftaiha *et al.*, 2020b) S(Im<sup>+</sup>-C<sub>16</sub>)<sub>2</sub>•2Br form expanded monolayers and their isotherms

do not exhibit a plateau region characterizing phase transition. It is noteworthy that the isotherms of silver nanoparticles capped with the corresponding GSs resulted in similar patterns, but shifted to smaller mean molecular area. (Datta *et al.*, 2014b) Surface tension measurements of Im-GSs in bulk solution indicated that the CMC values for those with butylene or xylenyl spacers were lower than the ethylene analogous (0.013 and 0.016 versus 0.028 mM, respectively, (**Figure A.3B-D**), which means that the former GSs are more prone to form sub-surface aggregates (*e.g.* micelles) in aqueous solution than the latter. We note that the insoluble nature of the monolayers needs to be considered here. Within the time scale of acquiring isotherms, no equilibrium is assumed between the sparingly water-soluble surfactant in the bulk phase and surface. It could be inferred from the isotherm data that both butylene and xylenyl Im-GSs achieved surface saturation at larger mean molecular area, after which molecules start to depart from the interface, enter the bulk water, and form micelles at the CMC.

The larger dipole moment of imidazole compared to pyridine 3.84 (Hamano & Hameka, 1962) *versus* 2.15 (Hameka & Liquori, 1958) Debye, respectively suggests a tendency to form a more expanded film in the case of  $S(\text{Im}^+-\text{C}_{16})_2 \cdot 2\text{Br}$ , because of the repulsive interactions along the amphiphilic molecular axes. (Takehara, Oozono, Oda, Isomura, & Taniguchi, 1990) This is reinforced by replacing the ester hinge (C-O-C(=O)) by a N-C bond, which results in less ordering of the lipid alkyl chains. In a similar manner, substituting one ester linkage in dipalmitoylphosphatidylcholine (DPPC) by ether bond influence its alignment and self-assembly at the air-water interface. (K. Y. C. Lee, Gopal, von Nahmen, Zasadzinski, Majewski, Smith, Howes, & Kjaer, 2002) Moreover, the location of (C=O) of the ester bond within sugar-based surfactants control their interfacial properties. (Razafindralambo, Blecker, Mezdour, Deroanne, Crowet, Brasseur, Lins, & Paquot, 2009) Furthermore, we note that the presence of the ester bond within the structure of ammonium GSs reduces the solubilization power of organic dyes. (Tehrani-Bagha, Singh, & Holmberg, 2012)

These observations might encourage future studies to design and improve our understanding of the interfacial behavior of GSs containing pharmaceutically relevant heterocyclic rings such as pyrazine, quinoline, pyrrole, and so forth., by attenuating LE-LC phase transition as in the case of conventional nicotinate ester against the GS counterparts or controlling the monolayer packing as obtained upon replacing pyridinium with imidazolium headgroup.

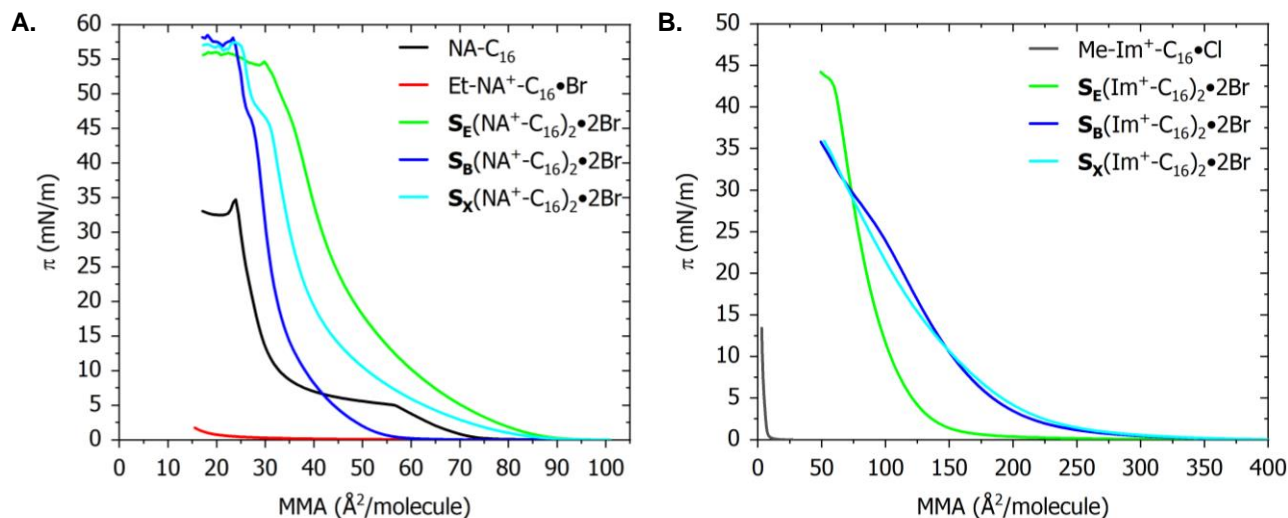


**Figure 3.1.**  $\pi$ - $A$  isotherms of conventional and gemini surfactants comprised of **A.** Nicotinate and **B.** Imidazolium head group(s).

We will now consider the mixing properties of the new surfactants with a simple fatty acid, PA. Fatty acids play important role in modulating biophysical, structural, and functional properties of cell membranes (Ibarguren, López, & Escribá, 2014) and PA is one the most common saturated fatty acid found in humans. (Carta, Murru, Banni, & Manca, 2017) In this work, we have chosen to work with PA rather than phospholipids because the complex chemical structure and phase behavior of the latter makes deconvoluting molecular organization and miscibility parameters challenging in comparison with fatty acids. (Paige & Eftaiha, 2017) As all synthesized NA-based surfactants bear palmitoyl tail(s), PA was chosen to allow investigation of intermolecular headgroup interactions, while keeping similar tail-tail interactions within the mixture components.  $\pi$ - $A$  isotherms of PA mixed either with NA- $C_{16}$  or  $S_x(NA^+-C_{16})_2 \cdot 2Br$  are shown in **Figure 3.2**. The isotherm of the pure PA monolayer is in a good agreement with previous literature. (Albrecht, 1989; Qaqish, Urquhart, Lanke, Brunet, & Paige, 2009) The surface pressure increases continuously, moving from gaseous to tilted and untilted condensed phases, respectively, after which, the monolayer collapses at  $\pi = 37$  mN/m with  $A_0$  value of about  $22.0 \text{ \AA}^2/\text{molecule}$ . The isotherms of the mixed films comprised of PA/NA- $C_{16}$  reside between those of the pure components (**Figure 3.2A**), where the onset of the transition pressure depends on the amount of the PA, that is, it is increases and shifts toward larger mean molecular area at higher content of NA- $C_{16}$ . This could be explained by the fact that PA is not able to condense the expanded portion of NA- $C_{16}$  monolayer. However, when PA is mixed with  $S_x(NA^+-C_{16})_2 \cdot 2Br$ , the isotherms are shifted markedly to larger mean molecular areas (**Figure 3.2B**).

The latter shift indicates nonideal mixing behavior. Moreover, the collapse pressure of the mixed monolayers (in both systems) is larger than the pure components regardless of the mole fraction. The high surface pressure values of the mixed monolayers are of particular interest for surface scientists working in the field of pulmonary surfactants, where additives (Ala'a F. Eftaiha & Paige, 2011; Ala'a F. Eftaiha, Brunet, & Paige, 2012b, 2012c; Ala'a F. Eftaiha, Tremblay, Rainey, & Paige, 2015) are used to inhibit the crystallization of DPPC (the main component of endogenous lung surfactant) at high compression pressure, (Zuo, Veldhuizen, Neumann, Petersen, & Possmayer, 2008) without affecting its ability to reduce surface tension. The reasonable elasticity values of  $S(\text{NA}^+-\text{C}_{16})_2\cdot 2\text{Br}$  films ( $> 100 \text{ mN/m}$ ), in comparison with the benchmark DPPC molecule (Figure A.4), suggest the potential use of the NA based surfactants in synthetic pulmonary surfactant preparations.

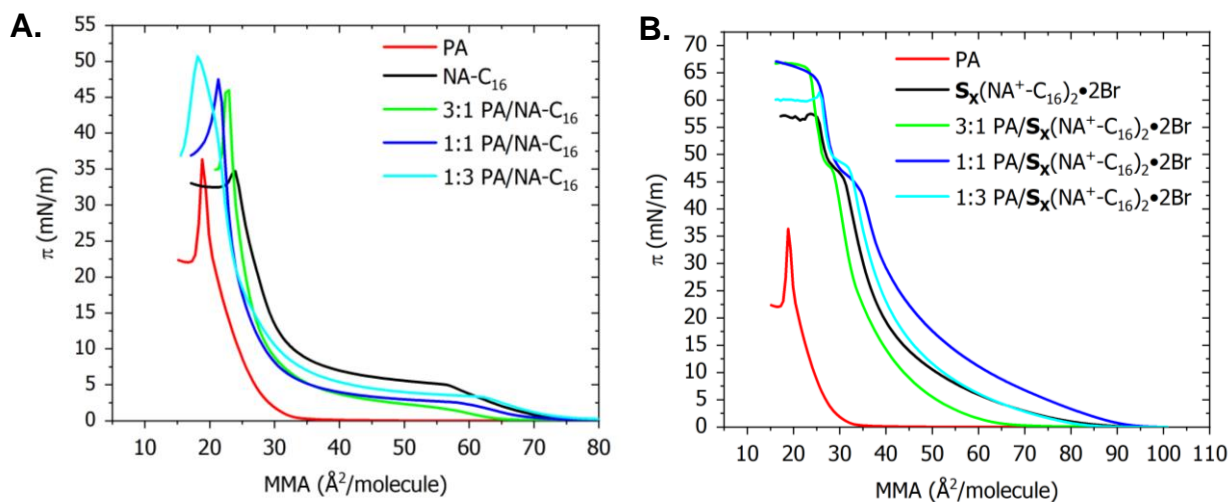


**Figure 3.2.**  $\pi$ - $A$  isotherms of: **A.** PA/NA- $\text{C}_{16}$ ; **B.** PA/ $\text{S}_x(\text{NA}^+-\text{C}_{16})_2\cdot 2\text{Br}$  mixed monolayers measured on Milli-Q water subphase at 25 °C. The data including 2:1 and 1:2 mixtures are presented in Figure S34, Supporting Information.

The extent of interaction between the film components was evaluated by calculating excess Gibbs free energy of mixing ( $\Delta G_{ex}^\pi$ ) according to the following equation: (Dynarowicz-Łątka & Kita, 1999)

$$\Delta G_{ex}^\pi = \int_0^\pi [A_{12} - \chi_1 A_1 - \chi_2 A_2] d\pi \quad (1)$$

where  $\chi_1$  and  $\chi_2$  are the molar fractions of component 1 and 2 in the binary mixed monolayer, respectively,  $A_{12}$ ,  $A_1$  and  $A_2$  are the areas under the isotherm curve for the mixed and pure monolayer film components.

As shown in **Figure 3.3**, positive  $\Delta G_{ex}^{\pi}$  values indicate that the mixed films are less stable than the pure monolayers of the individual components. The positive deviation from ideality is a function of surface pressure and composition and it is more pronounced in the case of the GS in comparison with the conventional counterpart.

For an aqueous subphase of  $pH = 5.5$ , one can reasonably expect PA ( $pK_a \sim 8.7$ ) (Kanicky, Poniatowski, Mehta, & Shah, 2000) to predominantly exist as neutral species (R-COOH), while around 50% of NA-C<sub>16</sub> head groups are expected to be protonated ( $pK_a$  of pyridinium cation is 5.2; (Dewick, 2013) shifts in protonation equilibria due to hydrophilic environment should be taken into consideration (Chi, Dhathathreyan, & Moebius, 1990)). This is anticipated to stabilize the mixed films because to dipole-dipole and ion-dipole interactions, and we further assume that this will be enhanced by the low steric hindrance with the carboxylate bearing the hydrophobic tail and the pyridine ring. (Dressler, Mastai, Rosenbluh, & Fleger, 2009) Aside from head-head interactions, there is a head-tail mismatch within NA-C<sub>16</sub> as indicated by DFT calculations that showed a larger cross-sectional area of the nicotinate ester headgroup in comparison with the hydrocarbon tail (24 vs 19 Å<sup>2</sup>; values were calculated in vacuum, **(Figure A.2)**). This is expected to affect the packing of the mixed monolayers.

In order to judge the overall mixing, we should pay attention to the total Gibbs free energy of mixing ( $\Delta G_{mix}^{total}$ ), which is made of two components,  $\Delta G_{ex}^{\pi}$  and the ideal Gibbs free energy of mixing ( $\Delta G_{mix}^{ideal}$ ), that equals to  $RT \sum_{i=1}^2 \chi_i \ln \chi_i$  (keep in mind that  $\Delta H_{mix}^{ideal} = 0$  as we should expect for a binary system in which the A-B interactions are the same as the A-A and B-B interactions). Thus, we postulate that entropy is the predominant thermodynamic factor controlling mixing (values range between -0.8 to -1.7 kJ.mol<sup>-1</sup>) as exceeded  $\Delta G_{ex}^{\pi}$  by several hundred J/mol. Herein, the entropy of mixing could be determined following Clapeyron equation ( $\Delta S_{mix} = -(\partial \Delta G_{mix} / \partial T)_{\pi}$ ) by measuring the  $\pi$ -A isotherms of the pure and mixed monolayers at different temperatures. The large ideal entropy value indicates it is predominant, thus, the temperature dependent mixing study is beyond the scope of the current work.

For PA/S<sub>x</sub>(NA<sup>+</sup>-C<sub>16</sub>)<sub>2</sub>•2Br mixed monolayers, the rigidity brought by the xylylenyl spacer allows for a complete separation between the pyridinium moieties, which interact with the underlying water subphase *via* ion-dipole interaction through the ring nitrogen and the Br<sup>-</sup> ion. While the attractive interaction between the positive charge of S<sub>x</sub>(NA<sup>+</sup>-C<sub>16</sub>)<sub>2</sub>•2Br and carboxylic acid head group of PA might nominally be used to justify their mutual attraction, the significant head-tail mismatch between PA and S<sub>x</sub>(NA<sup>+</sup>-C<sub>16</sub>)<sub>2</sub>•2Br is more likely to underlie immiscibility.

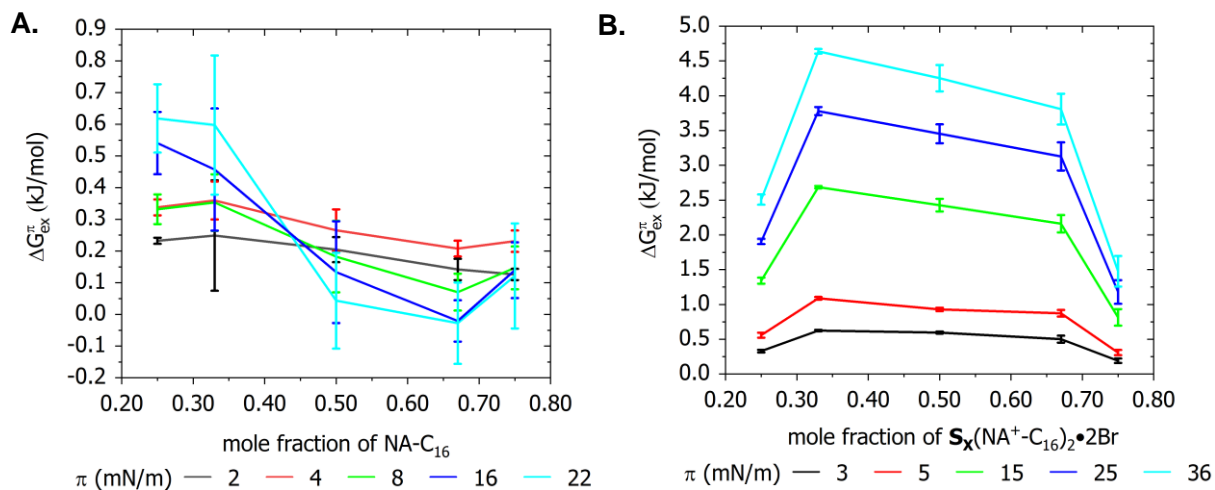


**Figure 3.3.**  $\Delta G_{ex}^{\pi}$  of binary mixtures comprised of: **A.** PA/NA-C<sub>16</sub>; **B.** PA/S<sub>x</sub>(NA<sup>+</sup>-C<sub>16</sub>)<sub>2</sub>•2Br measured as a function of monolayer composition at different surface pressure

The interaction between the hydrated surfactant headgroups was further examined using DFT calculations at B3LYP/6-31G(d) level of theory, applying polarizable continuum model (PCM). The use of short chain length (C-2 instead of C-16) simplified the calculations and offered fast computational time. The optimized *homo*- and *hetero*-pair are shown in **Figure 3.4**. Regarding the *homo* systems, the interaction energy between carboxylic acid headgroups is the lowest, followed by the nicotinate ester and its protonated form, then S<sub>x</sub>(NA<sup>+</sup>-C<sub>2</sub>)<sub>2</sub>. This can be rationalized by hydrogen bonding between the carboxylic acid groups and by electrostatic repulsion between the cationic groups of the GS, which exists to a lesser extent in the protonated ester (4 against 2 centers, respectively) and is absent in the case of the neutral ester. The *hetero* interactions are more favorable in the case of conventional NA-based surfactant, where cationic species attracts the carboxylic acid headgroup more strongly than the neutral ester. In contrast, the interaction of PA with S<sub>x</sub>(NA<sup>+</sup>-C<sub>2</sub>)<sub>2</sub> is less favorable, which agrees with the experimental data.

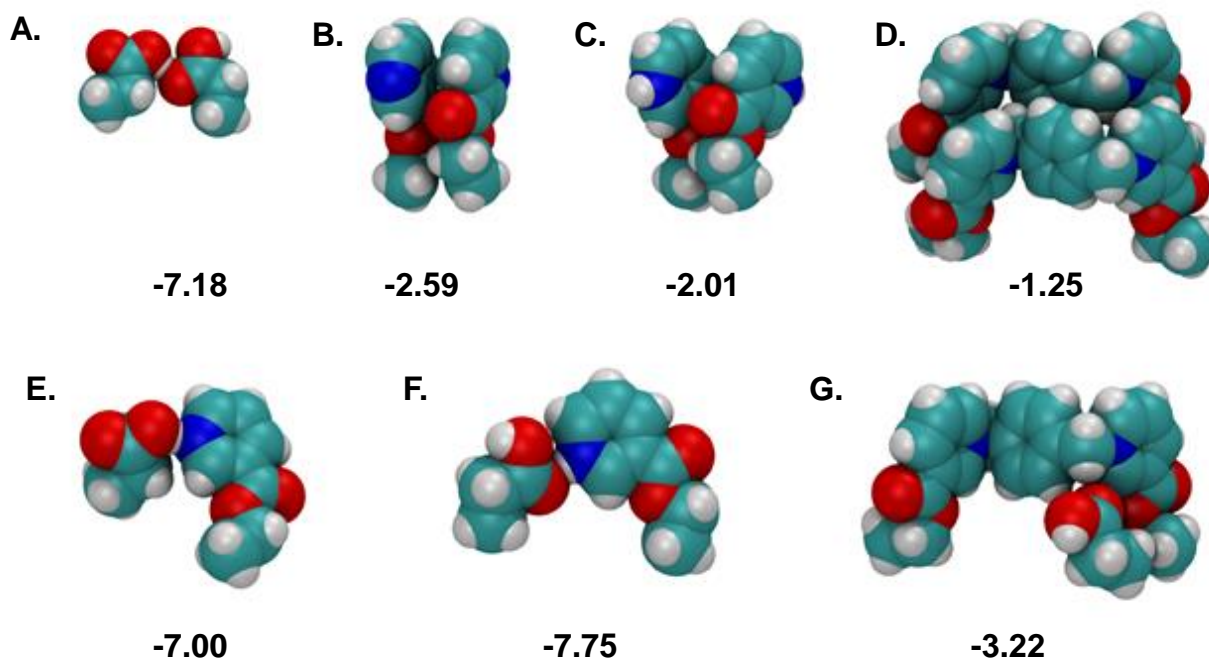


**Figure 3.4.** DFT-optimized structures of *homo*- and *hetero*-pair (with hydrated head groups using PCM model) of: **A.** carboxylic acid, **B.** nicotinate ester, **C.** protonated nicotinate, **D.**  $S_x(NA^+-C_2)_2$ , **E.** carboxylic acid: nicotinate ester, **F.** carboxylic acid: protonated nicotinate, **G.** carboxylic acid:  $S_x(NA^+-C_2)_2$ . Interaction energy values in kcal mol<sup>-1</sup> are given below structures.

BAM was used to measure morphology of NA-based films at the air-water interface. The contrast provides information on molecular organization and phase behavior by detecting changes in the interfacial refractive index when a *p*-polarized light is reflected in the presence/absence of surface-active molecules on the water surface. **Figure 3.5** shows BAM images of the conventional and gemini NA surfactants subjected to surface pressure of  $\pi = 7$  mN/m, a pressure at which clear morphological features of  $S_x(NA^+-C_{16})_2 \cdot 2Br$  was obtained. While the water soluble Et- $NA^+-C_{16}$  resulted in polydisperse, reflective circular domains of diameter ranging between 1.5 to 2.6  $\mu m$  (**Figure 3.5A**), NA- $C_{16}$  shows a uniform film structure, where separated lamella have been obtained after conducting several compression/expansion cycles (**Figure 3.5B**). Tremendous morphological changes were observed upon tethering the nicotinate esters *via* organic spacers (**Figure 3.5C-G**). The use of alkylene linkers resulted in the formation of micron-sized, discrete domains that were roughly circular in shape and became larger when the spacer length was doubled (ethylene *versus* butylene). When *p*-xylylene was incorporated within the GS motif, star-shaped structures were detected (**Figure 3.5E**). The domain size was increased when larger surface pressures were applied, suggesting that domains were being compressed and fused together at higher film

compression. It is noteworthy that the LE-LC phase was observed over a large range of pressures, because the BAM images were acquired under nonequilibrium conditions. The domain formation occurring during monolayer compression is likely a pressure-induced crystallization effect, but this would need to be confirmed using X-ray diffraction measurements on the floating monolayer, which is outside of the scope of this current work.

No contrast was observed for BAM images of both conventional and gemini imidazolium surfactants. This inherent limitation was reported previously by our group because of the comparable refractive index of imidazolium compounds and water (1.362 and 1.345, respectively). (A. F. Eftaiha *et al.*, 2020b) A similar scenario has been reported for mixed films composed of hydrogenated and perfluorinated surfactants. (Ala'a F. Eftaiha, Brunet, & Paige, 2012a; Ala'a F. Eftaiha & Paige, 2012)

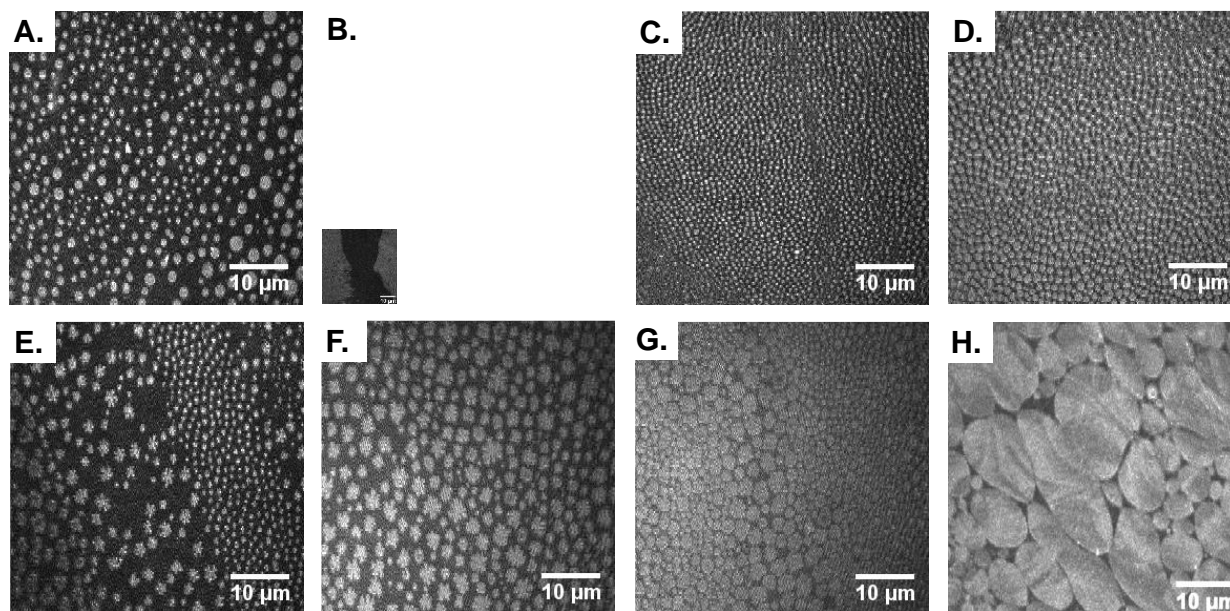


**Figure 3.5.** BAM images (50  $\mu\text{m}$  x 50  $\mu\text{m}$ ) measured at  $\pi = 7$  mN/m of: **A.** Et-NA<sup>+</sup>-C<sub>16</sub>•Br, **B.** NA-C<sub>16</sub>, **C.** S<sub>E</sub>(NA<sup>+</sup>-C<sub>16</sub>)<sub>2</sub>•2Br, **D.** S<sub>B</sub>(NA<sup>+</sup>-C<sub>16</sub>)<sub>2</sub>•2Br, **E-G.** S<sub>X</sub>(NA<sup>+</sup>-C<sub>16</sub>)<sub>2</sub>•2Br (The last two images were acquired at  $\pi = 15$  and 24 mN/m, respectively) and **H.** PA.

In order to obtain higher spatial resolution images, surfactant monolayers have been transferred from the air-water interface to mica substrates by LB deposition, then, they were measured using AFM under ambient conditions (**Figure 3.6**). The topographic images of Et-NA<sup>+</sup>-C<sub>16</sub>•Br and NA-C<sub>16</sub> were in a good agreement with the BAM data. The charged conventional surfactant forms well-resolved, sharp-edged domains, typically around 2.2  $\mu\text{m}$  in diameter and a height of 1.2 nm. NA-C<sub>16</sub> films were generally smooth and featureless at a length scale of 50  $\mu\text{m}$ . However, smaller-scale images (5  $\mu\text{m}$   $\times$  5  $\mu\text{m}$ ) show rippled

strands that extended to several micrometers in length and had thicknesses of 1.5 nm. These structures were not observed in BAM. We postulate that repulsive dipole-dipole interactions between surfactants plays a major role in controlling the formation of the ripples.(Seul & Andelman, 1995) Similar morphologies have been reported previously in supported phospholipid bilayers in the presence of tris(hydroxymethyl)aminomethane.(Mou, Yang, & Shao, 1994) For  $S(\text{NA}^+-\text{C}_{16})_2 \cdot 2\text{Br}$ , the stripes were modulated into distinct, micron sized domains, and the morphology varied significantly from three-lobed structures to higher order domain shapes as a function of linker (**Figure 3.6, C-E**). Cross sectional analysis of the three-lobed domain showed that its thickness estimated relative to the pinhole defect is around 1.5 nm.

Our working hypothesis is that line tension at the domain boundaries overcame the electrostatic repulsions between molecules to form compact domain shapes, but the relative importance of the two effects can be tailored by the molecular structure of the surfactant. Replacing butylene by ethylene moves the positively charged nitrogen atoms apart, and eventually anchors them in place in the case of the rigid xylynyl spacer. Accordingly, the unfavorable dipole repulsions become more important to produce more branched shapes.(Keller, McConnell, & Moy, 1986; H M McConnell, 1991; Harden M. McConnell & De Koker, 1992)

The difference between shapes associated with BAM and AFM could be explained by the inherent resolution limit of the former or the limited optical capability of the microscope.

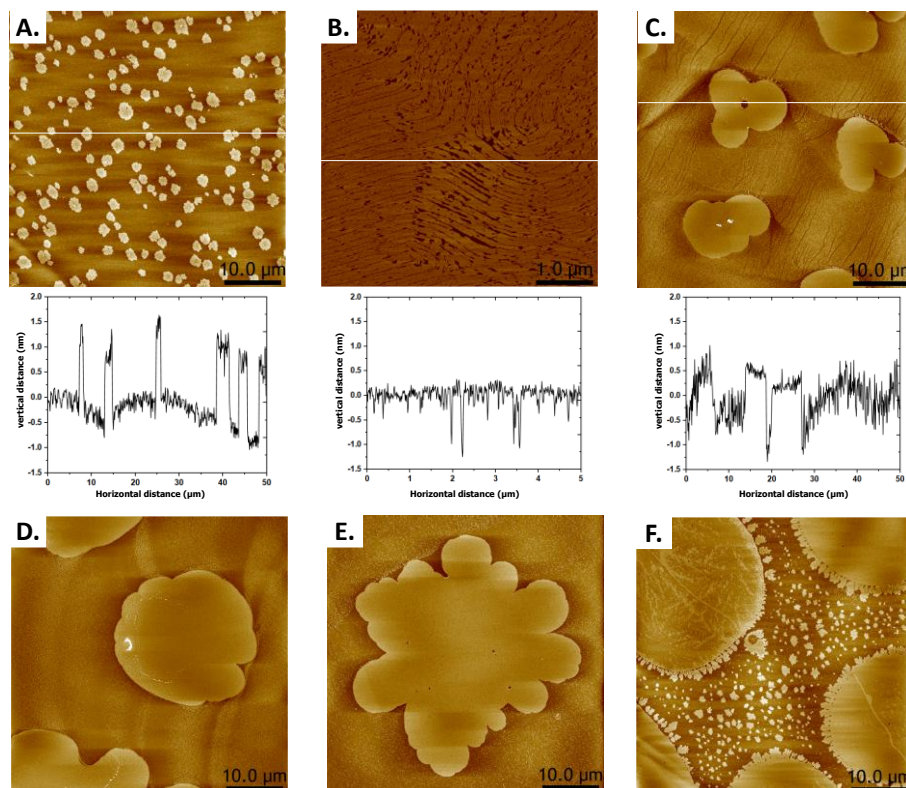


**Figure 3.6.** AFM height images measured at  $\pi = 7$  mN/m of: **A.** Et-NA<sup>+</sup>-C<sub>16</sub>•Br, **B.** NA-C<sub>16</sub>, **C.** S<sub>E</sub>(NA<sup>+</sup>-C<sub>16</sub>)<sub>2</sub>•2Br, **D.** S<sub>B</sub>(NA<sup>+</sup>-C<sub>16</sub>)<sub>2</sub>•2Br; **E.** S<sub>X</sub>(NA<sup>+</sup>-C<sub>16</sub>)<sub>2</sub>•2Br and **F.** PA.

In order to understand the morphologies of mixed films comprised of NA-based surfactants and PA, the latter was explored. As shown in **Figure 3.6F**, pure PA film consists of multiple circular domains with diameters ranged between approximately 20 and 30  $\mu\text{m}$ , with “hairy” extensions radiating out the domains. The domain heights ( $8.0 \pm 1.8$  Å) were less than the expected length of a PA molecule ( $\sim 24$  Å as determined by DFT calculations), suggesting that the surfactant molecules are tilted with respect to the substrate surface by an angle of  $70 \pm 5^\circ$  with respect to the normal. This is consistent with the data obtained from BAM (**Figure 3.5H**), where differences in reflectivity suggest variations in molecular tilt. (Nandi & Vollhardt, 2003) Our value is in a good agreement with data obtained from grazing incidence synchrotron X-ray diffraction of PA films measured at low surface pressure, that showed a tilt angle of about  $20 \pm 5^\circ$  toward nearest neighbors (about  $70^\circ$  with respect to the normal). (K. Y. C. Lee *et al.*, 2002; Weidemann, Brezesinski, Vollhardt, Bringezu, de Meijere, & Möhwald, 1998) Certainly, these measurements are highly dependent on the applied temperature and pH.

The molecular-level organization of the blend films were measured using BAM and AFM as well. BAM images of mixed PA/NA-C<sub>16</sub> monolayers (**Figure 3.7**) are composed of homogeneous low-reflectivity

matrix and reflective circular domains ranging in diameter from  $2.6 \pm 1.5 \mu\text{m}$  for the 3:1 PA/NA-C<sub>16</sub> mixture to around  $4.0 \pm 1.0 \mu\text{m}$  for the mixtures containing 0.50 and 0.33 mole fraction of PA, respectively. The polydispersity of the domains is a function of the NA-C<sub>16</sub> content, and the films contain the highest number of reflective domains at equimolar surfactant ratio. The AFM images shows small discrete structures squeezed between equally leveled domains. The formation of circular patterns is likely driven by line tension as anticipated from the equal *homo* and *hetero* tail-tail interactions as well as the mixing thermodynamics together with the energetics of hydrated surfactant headgroups deduced from DFT calculations.

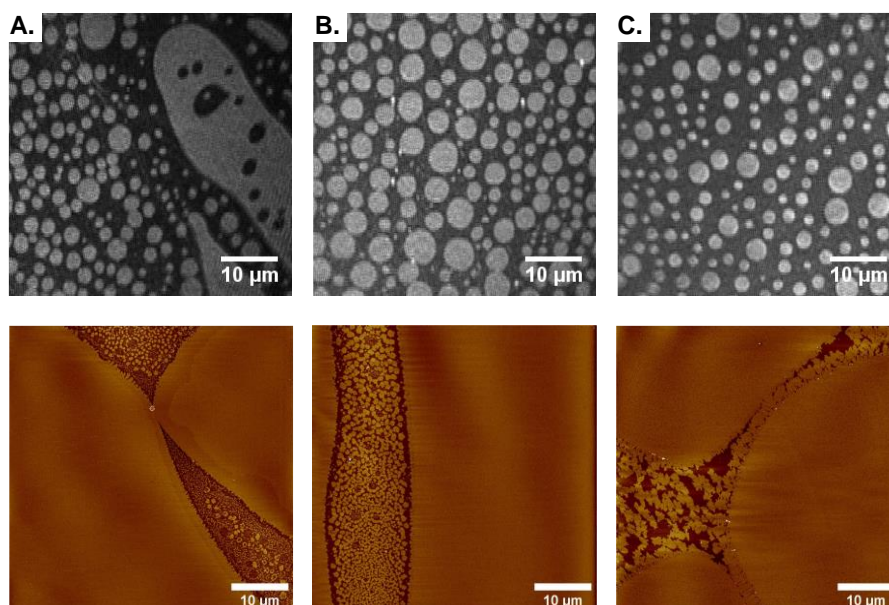


**Figure 3.7.** BAM and the corresponding AFM images of: **A.** 3:1, **B.** 1:1, and **C.** 1:3 PA/(NA-C<sub>16</sub>) mixed monolayers obtained at  $\pi = 7 \text{ mN/m}$ .

As  $\text{Sx}(\text{NA}^+\text{-C}_{16})_2 \cdot 2\text{Br}$  was mixed with PA, the circular domains became smaller, and the extensions diminished (**Figure 3.8A**). For the 1:1 mixture, the domains retained their original shape as in the neat  $\text{Sx}(\text{NA}^+\text{-C}_{16})_2 \cdot 2\text{Br}$  films, which might indicate the occurrence of phase separation (**Figure 3.8B**). At sufficiently high molar fractions of  $\text{Sx}(\text{NA}^+\text{-C}_{16})_2 \cdot 2\text{Br}$ , the film comprised of several circular, sharp-edged domains (**Figure 3.8C**). Although AFM topographic images lack chemical information, which makes compositional mapping challenging, the persistence of the multilobed domain structures is indicative of surfactant immiscibility. The results for these mixtures are consistent with the repulsive interaction between the film components for all compositions. In short, tethering the nicotinate ester allows control over the film miscibility from being ideally to nonideally miscible.

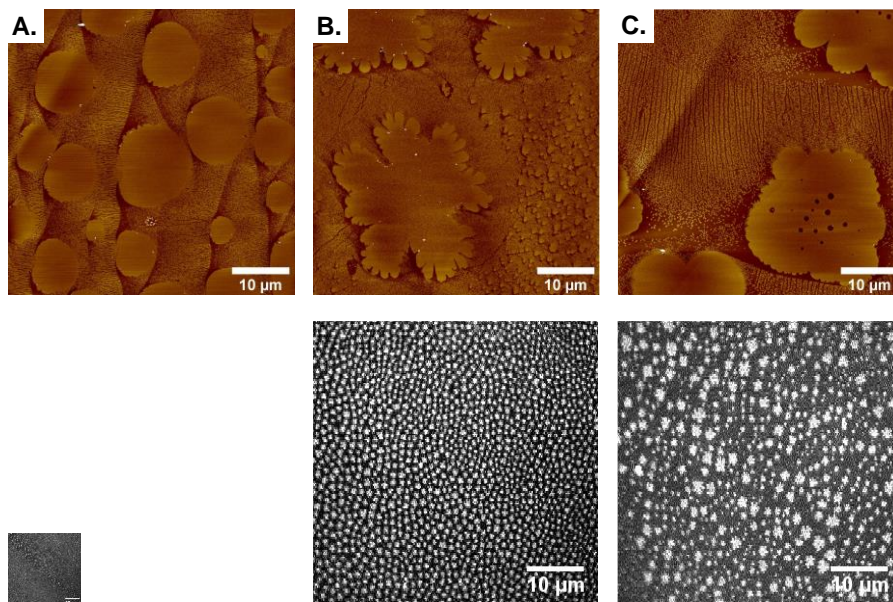


**Figure 3.8.** AFM height images and the corresponding BAM measured at  $\pi = 7$  mN/m of: **A.** 3:1 PA/S<sub>x</sub>(NA<sup>+</sup>-C<sub>16</sub>)<sub>2</sub>•2Br, **B.** 1:1 PA/S<sub>x</sub>(NA<sup>+</sup>-C<sub>16</sub>)<sub>2</sub>•2Br, and **C.** 1:3 PA/S<sub>x</sub>(NA<sup>+</sup>-C<sub>16</sub>)<sub>2</sub>•2Br. The estimated domain thickness relative to the pinhole defect is around 1.3 nm.

We note that some caution must be taken when comparing these different data sets. BAM and AFM provide different and complementary information about surfactant films at air-water and air-solid interfaces, respectively. Both have different spatial resolution, mechanism of contrast and imaging artifacts. While some film features are similar for the two techniques, we also believe that the deposition process strongly influenced monolayer domain shape and size. In this context, dynamic wetting instabilities might drive domain condensation during substrate withdrawal. While the film structures (in Figure 2.7 and 2.8) appear quite different, some similar sized circular domains are obtained (though they are on average larger in the BAM than in the AFM). However, the films also form large, flat domains in the AFM images, which suggests that domain fusion occurs during the drying process. Careful inspection of the images also reveals cracks in the film, suggesting that drying effects do impact the film structures.

## 3.4 Experimental

### 3.4.1 Chemicals

Nicotinic acid (98%), imidazole (99%), 1-bromohexadecane (97%), 1,4-dibromobutane (99%),  $\alpha,\alpha'$ -dibromo-*p*-xylene (97%), 1-hexadecyl-3-methyl imidazolium chloride (Me-Im<sup>+</sup>-C<sub>16</sub>•Cl) and palmitic acid (PA) were purchased from Sigma-Aldrich. 1-Bromoethane (99 %) and 1,2-Dibromoethane (98%) were

obtained from Ridel-de Haen and Fluka Analytica, respectively. Dipalmitoylphosphatidylcholine was purchased from Avanti Polar Lipids. Mica substrates (Grade V-I, 12 mm discs  $\times$  0.275-0.325 mm) were purchased from SPI Supplies. Each was cleaved with adhesive tape prior to film deposition. Chloroform (HPLC grade) and hydrochloric acid (37%) were acquired from TEDIA and Carol Erba, respectively.

### 3.4.2 $\pi$ -A isotherm measurements and LB film depositions

Stock solutions (0.5 mM) of pure materials were prepared by dissolving appropriate amount of the solid compounds in chloroform. Binary mixtures of PA and NA-based surfactants were prepared by mixing aliquots of the two solutions to give the desired molar ratio.  $\pi$ -A isotherms were measured at  $25 \pm 0.1$  °C (controlled using a Julabo circulating water bath) by spreading 80  $\mu$ L of the surfactant solution from a Hamilton micro-syringe on an ultrapure, Milli-Q water as a subphase (resistivity 18 M $\Omega$ .cm, pH 5.5) in a medium size Langmuir trough (area of 273 cm<sup>2</sup>, KSV NIMA) equipped with a Wilhelmy balance. The surface pressure was recorded using a homemade paper plate. The solvent was allowed to evaporate for 15 min prior compression at 10 mm/min ( $\sim 3.11$  Å<sup>2</sup>/molecule/min). For reproducibility, at least three isotherms were measured and averaged. LB film depositions were carried out at  $\pi = 7$  mN/m in a medium Langmuir trough with a central dipping well (20  $\times$  56  $\times$  60 mm, KSV NIMA) The films were allowed to stabilize for 15 min before the mica substrate was pulled upward through the water–air interface in a single stroke. The film was left to dry in a clean environment at room temperature before AFM measurement.

### 3.4.3 BAM measurements

The procedures of surfactant spreading, and solvent evaporation were similar to those adopted for the  $\pi$ -A measurements. The monolayer was compressed at 10 mm/min up  $\pi = 7$  mN/m and measured using a MicroBAM (Biolin Scientific) outfitted with a 50 mW, 659 nm laser. The angle of the incident laser light at the air-water interface was fixed to the Brewster angle (53°). For Et-NA<sup>+</sup>-C<sub>16</sub>, adequate contrast was obtained upon using 1.5 mM and spreading volume of 200  $\mu$ L.

### 3.4.4 AFM measurements

AFM topography images were collected using a Multimode 8 instrument (Bruker) operating in ScanAsyst mode in air using OTESPA-R3 AFM probes (Bruker). Samples were imaged with a scan size

of  $50\ \mu\text{m} \times 50\ \mu\text{m}$ , a scan rate of 0.8 Hz and a resolution of 512 samples/line. No tip-induced damage of films was observed under the operating conditions used.

### 3.4.5 CMC measurements

A 10 mL stock solution of each surfactant was prepared by dissolving an appropriate amount of the solid with water. The surface tension of each solution was measured at 25 °C using a Wilhelmy plate force tensiometer (Sigma 700, Biolin Scientific). Then successive dilutions were performed until constant surface tension values were obtained. Each data point is the average of three measurements within  $\pm 0.2$  mN/m. The CMC was taken as the inflection point in the plot of surface tension against log concentration.

## 3.5 Conclusion

The surface behavior of conventional and gemini surfactants comprised of pyridine(ium) and imidazolium groups have been investigated at air-water interface. The  $\pi$ - $A$  isotherm of the nicotinate ester exhibited LE-LC phase transition, and the quaternarized form together with the corresponding GSs demonstrated single smooth curves. The films of the latter were less expanded in comparison with imidazolium-based GSs. When NA-C<sub>16</sub> or S<sub>x</sub>(NA<sup>+</sup>-C<sub>16</sub>)<sub>2</sub>•2Br was mixed with PA, the monolayer collapse pressures were larger than the pure components over all composition. The degree of surfactant miscibility, as manifested by excess Gibbs free energies of mixing, was controlled by statistical entropy for PA/NA-C<sub>16</sub> and head-tail mismatch between PA and S<sub>x</sub>(NA<sup>+</sup>-C<sub>16</sub>)<sub>2</sub>•2Br. The morphology of the neat films indicated the strong tendency of NA-GSs to self-assemble into well-defined, discrete domains as obtained by a combination of BAM and AFM. Consistent with mixing thermodynamics, film morphology measurements indicated that NA-C<sub>16</sub> tends to mix with PA, while the GS counterpart maintained its domain shape to great extent.

## 3.6 Acknowledgment

This work was funded by the deanship of scientific research at the Hashemite University. Dr. Rania Hamed from Al-Zaytoonah University (Amman, Jordan) is acknowledged for assisting in CMC measurements. ASA is thankful to the faculty of graduate studies at HU for partially funding this work.

## Chapter 4

### Future Work

Examination of surfactants biodegradability and cytotoxicity is essential when considering medical and pharmaceutical applications of those molecules. So, *in vitro*, and *in vivo* experiments will be conducted in collaboration with other research groups to adjust molecular design to ultimately achieve a chemical structure with preferable characters. Moreover, exploring GSs miscibility with a more complex molecules like phospholipid in mono- and bilayers systems using blood or lung fluid mimicking subphase is of particular importance to shed more light on the real-life applications of the synthesized molecules.

Furthermore, we believe that changing the spacer polarity together with the head-tail “*hinge*” including both its relative position with respect to the N-atom of the pyridine ring and the linker identity, namely, amide *versus* ester and C-C bond will control surfactant self-assembly. This will be accomplished following microwave assisted, green synthesis protocols.

## References

- Achour, S., Hamada, B., Baroudi, S., Abdelaziz, A., Rezazgui, I., & Trache, D. (2021). Spectroscopic characterization and thermal decomposition kinetics of 1,3-dibutyl-imidazolium bromide synthesized through a solvent-free and one-pot method. *Journal of Molecular Liquids*, *339*, 117266.
- Adams, E. M., Verreault, D., Jayarathne, T., Cochran, R. E., Stone, E. A., & Allen, H. C. (2016). Surface organization of a DPPC monolayer on concentrated SrCl<sub>2</sub> and ZnCl<sub>2</sub> solutions. *Physical Chemistry Chemical Physics*, *18*(47), 32345–32357.
- Akbaş, H., Elemenli, A., & Boz, M. (2012). Aggregation and Thermodynamic Properties of Some Cationic Gemini Surfactants. *Journal of Surfactants and Detergents*, *15*(1), 33–40.
- Alami, E., Beinert, G., Marie, P., & Zana, R. (1993). Alkanediyl- $\alpha,\omega$ -bis(dimethylalkylammonium bromide) surfactants. 3. Behavior at the air-water interface. *Langmuir*, *9*(6), 1465–1467.
- Albrecht, O. (1989). Experimental study of the stability and metastability of palmitic acid. *Thin Solid Films*, *178*(1), 93–101.
- Aldrich, S. (2022). Nicotinic acid. Retrieved from <https://www.sigmaaldrich.com/JO/en/product/sial/n4126>
- Amirthalingam, E., Rodrigues, M., Casal-Dujat, L., Calpena, A. C., Amabilino, D. B., Ramos-López, D., & Pérez-García, L. (2015). Macrocyclic imidazolium-based amphiphiles for the synthesis of gold nanoparticles and delivery of anionic drugs. *Journal of Colloid and Interface Science*, *437*, 132–139.
- Anastas, P., & Eghbali, N. (2010). Green Chemistry: Principles and Practice. *Chem. Soc. Rev.*, *39*(1), 301–312.
- Anastas, P. T., & Warner, J. C. (2000). *Green Chemistry Theory and Practice*. Oxford University Press.
- Anastas, P., & Warner, J. (2000). *Green Chemistry: Theory and Practice*. Oxford, New York: Oxford University Press.
- Anchev, B. A., Tsekova, D. S., Mircheva, K. M., & Grozev, N. A. (2019). Monolayer formed by 1-Asp-based gemini surfactants self-assembled in 1D nanostructures. *RSC Adv.*, *9*(57), 33071–33079.
- Badgett, C. O., Provost, R. C., Ogg, C. L., & Woodward, C. F. (1945). Nicotinic Acid. Water-insoluble Esters and Amides. *Journal of the American Chemical Society*, *67*(7), 1135–1138.

- Bengt Kronberg (Ed.). (2014). Types of Surfactants, their Synthesis, and Applications. In *Surface Chemistry of Surfactants and Polymers* (pp. 1–47). John Wiley & Sons, Ltd.
- Bhadani, A., & Singh, S. (2009). Novel Gemini Pyridinium Surfactants: Synthesis and Study of Their Surface Activity, DNA Binding, and Cytotoxicity. *Langmuir*, 25(19), 11703–11712.
- Bhadani, A., & Singh, S. (2011). Synthesis and Properties of Thioether Spacer Containing Gemini Imidazolium Surfactants. *Langmuir*, 27(23), 14033–14044.
- Bora, D., Deb, B., Fuller, A. L., Slawin, A. M. Z., Derek Woollins, J., & Dutta, D. K. (2010). Dicarboxyliridium(I) complexes of pyridine ester ligands and their reactivity towards various electrophiles. *Inorganica Chimica Acta*, 363(7), 1539–1546.
- Britannica encyclopedia. (2017). Retrieved April 2, 2022, from <https://www.britannica.com/science/niacin>
- Britannica encyclopedia. (2018). Retrieved April 2, 2022, from <https://www.britannica.com/science/pyridine>
- Bunton, C. A., Robinson, L. B., Schaak, J., & Stam, M. F. (1971). Catalysis of nucleophilic substitutions by micelles of dicationic detergents. *The Journal of Organic Chemistry*, 36(16), 2346–2350.
- Butt, H.-J. (2010). Introduction. In *Surface and Interfacial Forces* (pp. 1–4). John Wiley & Sons, Ltd.
- Carta, G., Murru, E., Banni, S., & Manca, C. (2017). Palmitic Acid: Physiological Role, Metabolism and Nutritional Implications. *Frontiers in Physiology*, 8.
- Casal-Dujat, L., Rodrigues, M., Yagüe, A., Calpena, A. C., Amabilino, D. B., González-Linares, J., Borràs, M., & Pérez-García, L. (2012). Gemini Imidazolium Amphiphiles for the Synthesis, Stabilization, and Drug Delivery from Gold Nanoparticles. *Langmuir*, 28(5), 2368–2381.
- Chen, S., Hanning, S., Falconer, J., Locke, M., & Wen, J. (2019). Recent advances in non-ionic surfactant vesicles (niosomes): Fabrication, characterization, pharmaceutical and cosmetic applications. *European Journal of Pharmaceutics and Biopharmaceutics*, 144, 18–39.
- Chi, L. F., Dhathathreyan, A., & Moebius, D. (1990). Investigation of protonation equilibria and spectroscopic properties of the (aminostyryl)pyridinium chromophore in solution, spread monolayers, and Langmuir-Blodgett films. *Langmuir*, 6(8), 1360–1363.
- Costa, C., Oliveira, I. S., Silva, J. P. N., Silva, S. G., Botelho, C., do Vale, M. L. C., Real Oliveira, M. E. C. D., Gomes, A. C., & Marques, E. F. (2021). Effective cytocompatible nanovectors based on serine-derived gemini surfactants and monoolein for small interfering RNA delivery. *Journal of Colloid and Interface Science*, 584, 34–44.

- Datta, S., Biswas, J., & Bhattacharya, S. (2014a). How does spacer length of imidazolium gemini surfactants control the fabrication of 2D-Langmuir films of silver-nanoparticles at the air–water interface? *Journal of Colloid and Interface Science*, *430*, 85–92.
- Datta, S., Biswas, J., & Bhattacharya, S. (2014b). How does spacer length of imidazolium gemini surfactants control the fabrication of 2D-Langmuir films of silver-nanoparticles at the air–water interface? *Journal of Colloid and Interface Science*, *430*, 85–92.
- de Oliveira, R. F., de Barros, A., & Ferreira, M. (2017). 4 - Nanostructured Films: Langmuir–Blodgett (LB) and Layer-by-Layer (LbL) Techniques. In A. L. Da Róz, M. Ferreira, F. de Lima Leite, & O. N. Oliveira (Eds.), *Nanostructures* (pp. 105–123). William Andrew Publishing.
- Dewick, P. M. (2013). *Essentials of Organic Chemistry: For Students of Pharmacy, Medicinal Chemistry and Biological Chemistry*. Wiley.
- Ding, Y.-S., Zha, M., Zhang, J., & Wang, S.-S. (2007). Synthesis, characterization and properties of geminal imidazolium ionic liquids. *Colloids and Surfaces A: Physicochemical and Engineering Aspects*, *298*(3), 201–205.
- Dressler, D. H., Mastai, Y., Rosenbluh, M., & Fleger, Y. (2009). Surface-enhanced Raman spectroscopy as a probe for orientation of pyridine compounds on colloidal surfaces. *Journal of Molecular Structure*, *935*(1), 92–96.
- Du, X., Lu, Y., Li, L., Wang, J., & Yang, Z. (2006). Synthesis and unusual properties of novel alkylbenzene sulfonate gemini surfactants. *Colloids and Surfaces A: Physicochemical and Engineering Aspects*, *290*(1), 132–137.
- Dynarowicz-Łątka, P., & Kita, K. (1999). Molecular interaction in mixed monolayers at the air/water interface. *Advances in Colloid and Interface Science*, *79*(1), 1–17.
- Eaton, peter. (2014). Atomic Force Microscopy. *MRS Bulletin*, *39*(4), 379–379.
- Eftaiha, A., Brunet, S., & Paige, M. (2012). *A comparison of atomic force microscopy, confocal fluorescence microscopy and brewster angle microscopy for characterizing mixed monolayer surfactant films*.
- Eftaiha, A. F., Qaroush, A. K., Kayed, G. G., Abdel Rahman, A. R. K., Assaf, K. I., & Paige, M. F. (2020a). Morphological and Interaction Characteristics of Surface-Active Ionic Liquids and Palmitic Acid in Mixed Monolayers. *ChemPhysChem*, *21*(16), 1858–1865.

- Eftaiha, A. F., Qaroush, A. K., Kayed, G. G., Abdel Rahman, A. R. K., Assaf, K. I., & Paige, M. F. (2020b). Morphological and Interaction Characteristics of Surface-Active Ionic Liquids and Palmitic Acid in Mixed Monolayers. *ChemPhysChem*, *21*(16), 1858–1865.
- Eftaiha, Ala'a F., Brunet, S. M. K., & Paige, M. F. (2012a). A comparison of atomic force microscopy, confocal fluorescence microscopy and Brewster angle microscopy for characterizing mixed monolayer surfactant films. In *Microscopy Series: Vol. 5. Current Microscopy Contributions to Advances in Science and Technology* (Vol. 2, pp. 1438–1447). Spain: Formatex Research Center.
- Eftaiha, Ala'a F., Brunet, S. M. K., & Paige, M. F. (2012b). Influence of Film Composition on the Morphology, Mechanical Properties, and Surfactant Recovery of Phase-Separated Phospholipid-Perfluorinated Fatty Acid Mixed Monolayers. *Langmuir*, *28*(43), 15150–15159.
- Eftaiha, Ala'a F., Brunet, S. M. K., & Paige, M. F. (2012c). Thermodynamic and structural characterization of a mixed perfluorocarbon-phospholipid ternary monolayer surfactant system. *Journal of Colloid and Interface Science*, *368*, 356–365.
- Eftaiha, Ala'a F., & Paige, M. F. (2011). The influence of salinity on surfactant miscibility in mixed dipalmitoylphosphatidylcholine—Perfluorooctadecanoic acid monolayer films. *Journal of Colloid and Interface Science*, *353*(1), 210–219.
- Eftaiha, Ala'a F., & Paige, M. F. (2012). Phase-separation of mixed surfactant monolayers: A comparison of film morphology at the solid-air and liquid-air interfaces. *Journal of Colloid and Interface Science*, *380*, 105–112.
- Eftaiha, Ala'a F., Tremblay, M.-L., Rainey, J. K., & Paige, M. F. (2015). The effect of perfluorooctadecanoic acid on a model phosphatidylcholine-peptide pulmonary lung surfactant mixture. *Journal of Fluorine Chemistry*, *177*(SI), 55–61.
- Franke, Maximilian E., & Rehage, H. (2019). Effects of Chirality on the Aggregation Properties of Amide-Bonded Pyridinium Gemini Surfactants. *Langmuir*, *35*(27), 8968–8976.
- Franke, Maximilian Eberhard, & Rehage, H. (2022). Synthesis and characterisation of carboxy amide-bonded pyridinium Gemini surfactants: Influence of the nature of the spacer group and counterions on the aggregation behaviour. *Tenside Surfactants Detergents*, *59*(2), 111–121.
- Garcia, M. T., Ribosa, I., Perez, L., Manresa, A., & Comelles, F. (2013). Aggregation Behavior and Antimicrobial Activity of Ester-Functionalized Imidazolium- and Pyridinium-Based Ionic Liquids in Aqueous Solution. *Langmuir*, *29*(8), 2536–2545.

- Giner-Casares, J. J., Brezesinski, G., & Möhwald, H. (2014). Langmuir monolayers as unique physical models. *Current Opinion in Colloid & Interface Science*, *19*(3), 176–182.
- Girgis, A. S., Kalmouch, A., & Ellithey, M. (2006). Synthesis of novel vasodilatory active nicotinate esters with amino acid function. *Bioorganic & Medicinal Chemistry*, *14*(24), 8488–8494.
- Gunderson, F. L. (1943). Need for Water-Insoluble Forms of Water-Soluble Vitamins. *Science*, *98*(2543), 277–277.
- Hamano, H., & Hameka, H. F. (1962). On the dipole moments and chemical properties of pyrazole and imidazole. *Tetrahedron*, *18*(8), 985–990.
- Hameka, H. F., & Liquori, A. M. (1958). Some considerations on the dipole moments of azines. *Molecular Physics*, *1*(1), 9–13.
- Han, X., Xu, J., Liu, H., & Hu, Y. (2005). A New Approach to Thick Films of a Block Copolymer with Ordered Surface Structures. *Macromolecular Rapid Communications*, *26*(22), 1810–1813.
- Hann, R. A. (1990). Molecular Structure and Monolayer Properties. In G. Roberts (Ed.), *Langmuir-Blodgett Films* (pp. 17–92). Boston, MA: Springer US.
- Harjani, J. R., Singer, R. D., Garcia, M. T., & Scammells, P. J. (2008). The design and synthesis of biodegradable pyridinium ionic liquids. *Green Chem.*, *10*(4), 436–438.
- He, Y., He, L., Khoshaba, R., Lu, F., Cai, C., Zhou, F., Liao, D., & Cao, D. (2019). Curcumin Nicotinate Selectively Induces Cancer Cell Apoptosis and Cycle Arrest through a P53-Mediated Mechanism. *Molecules*, *24*(22).
- Hou, B., Jia, R., Fu, M., Wang, Y., Ma, C., Jiang, C., & Yang, B. (2019). A novel high temperature tolerant and high salinity resistant gemini surfactant for enhanced oil recovery. *Journal of Molecular Liquids*, *296*, 112114.
- Ibarguren, M., López, D. J., & Escribá, P. V. (2014). The effect of natural and synthetic fatty acids on membrane structure, microdomain organization, cellular functions and human health. *Membrane Structure and Function: Relevance in the Cell's Physiology, Pathology and Therapy*, *1838*(6), 1518–1528.
- IHS Markit. (2021). Retrieved March 29, 2022, from IHS Markit website: <https://ihsmarkit.com/products/chemical-surfactants-scup.html>
- Izmaylov, B., Di Gioia, D., Markova, G., Aloisio, I., Colonna, M., & Vasnev, V. (2015). Imidazolium salts grafted on cotton fibres for long-term antimicrobial activity. *Reactive and Functional Polymers*, *87*, 22–28.

- Johnsson, M., & Engberts, J. B. F. N. (2004). Novel sugar-based gemini surfactants: Aggregation properties in aqueous solution. *Journal of Physical Organic Chemistry*, *17*(11), 934–944.
- Joule, J. A. (John A., & Mills, K. (Keith). (2010). Heterocyclic chemistry John A. Joule, Keith Mills. In *Heterocyclic chemistry* (5th ed.). Chichester, West Sussex: Wiley.
- Kaercher, T., Hönig, D., & Möbius, D. (1993). Brewster angle microscopy. *International Ophthalmology*, *17*(6), 341–348.
- Kan, T., Jiang, X., Zhou, L., Yang, M., Duan, M., Liu, P., & Jiang, X. (2011). Removal of methyl orange from aqueous solutions using a bentonite modified with a new gemini surfactant. *Applied Clay Science*, *54*(2), 184–187.
- Kanicky, J. R., Poniatowski, A. F., Mehta, N. R., & Shah, D. O. (2000). Cooperativity among Molecules at Interfaces in Relation to Various Technological Processes: Effect of Chain Length on the pKa of Fatty Acid Salt Solutions. *Langmuir*, *16*(1), 172–177.
- Kaufman, J. G. (1945). Nicotinic Acid Esters. *Journal of the American Chemical Society*, *67*(3), 497–498.
- Keller, D. J., McConnell, H. M., & Moy, V. T. (1986). Theory of superstructures in lipid monolayer phase transitions. *The Journal of Physical Chemistry*, *90*(11), 2311–2315.
- Kobetić, R., & Sunko, D. E. (2008). Hydrolysis of Cyclopentenyl-alkyl-N-methyl Nicotines in Micelles and Cyclodextrines. *Supramolecular Chemistry*, *20*(4), 369–377.
- Kumar, N., & Tyagi, R. (2014). Industrial Applications of Dimeric Surfactants: A Review. *Journal of Dispersion Science and Technology*, *35*(2), 205–214.
- Kum-Tatt, L. (1958). Quantitative Separation of Nitrogenous Organic Bases using Ammonium Reineckate. *Nature*, *182*(4636), 655–656.
- Lee, D. K., Kim, Y. I., Kwon, Y. S., Kang, Y. S., & Kevan, L. (1997a). Electron Magnetic Resonance Study of the Photoreduction of Alkylviologens in Anionic Sodium Dodecyl Sulfate and Cationic Dodecyltrimethylammonium Bromide Micelles. *The Journal of Physical Chemistry B*, *101*(27), 5319–5323.
- Lee, D. K., Kim, Y. I., Kwon, Y. S., Kang, Y. S., & Kevan, L. (1997b). Electron Magnetic Resonance Study of the Photoreduction of Alkylviologens in Anionic Sodium Dodecyl Sulfate and Cationic Dodecyltrimethylammonium Bromide Micelles. *The Journal of Physical Chemistry B*, *101*(27), 5319–5323.
- Lee, K. Y. C., Gopal, A., von Nahmen, A., Zasadzinski, J. A., Majewski, J., Smith, G. S., Howes, P. B., & Kjaer, K. (2002). Influence of palmitic acid and hexadecanol on the phase transition temperature

and molecular packing of dipalmitoylphosphatidyl-choline monolayers at the air–water interface. *The Journal of Chemical Physics*, 116(2), 774–783.

- Lee, M., Choi, U. H., Wi, S., Slebodnick, C., Colby, R. H., & Gibson, H. W. (2011). 1,2-Bis[N-(N'-alkylimidazolium)]ethane salts: A new class of organic ionic plastic crystals. *Journal of Materials Chemistry*, 21(33), 12280–12287.
- Lehmler, H.-J., & Bummer, P. M. (2005). Interaction of a partially fluorinated long-chain nicotinate with dipalmitoylphosphatidylcholine. *Journal of Lipid Research*, 46(11), 2415–2422.
- Lehmler, H.-J., Fortis-Santiago, A., Nauduri, D., & Bummer, P. M. (2005a). Interaction of long-chain nico tinates with dipalmitoylphosphatidylcholine. *Journal of Lipid Research*, 46(3), 535–546.
- Lehmler, H.-J., Fortis-Santiago, A., Nauduri, D., & Bummer, P. M. (2005b). Interaction of long-chain nico tinates with dipalmitoylphosphatidylcholine. *Journal of Lipid Research*, 46(3), 535–546.
- Lehmler, H.-J., Xu, L., Vyas, S. M., Ojogun, V. A., Knutson, B. L., & Ludewig, G. (2008). Synthesis, physicochemical properties and in vitro cytotoxicity of nicotinic acid ester prodrugs intended for pulmonary delivery using perfluorooctyl bromide as vehicle. *International Journal of Pharmaceutics*, 353(1), 35–44.
- Lewandowski, W., Barańska, H., & Mościbroda, P. (1993). Vibrational study of nicotinic acid complexes with different central ions. *Journal of Raman Spectroscopy*, 24(12), 819–824.
- Li, M., Fu, H., Yang, M., Zheng, H., He, Y., Chen, H., & Li, X. (2005). Micellar effect of cationic gemini surfactants on organic/aqueous biphasic catalytic hydroformylation of 1-dodecene. *Journal of Molecular Catalysis A: Chemical*, 235(1), 130–136.
- Li, R., Chen, Q., Liu, H., & Hu, Y. (2010). Influence of Spacer of Gemini on the Interactions between Cationic Gemini Surfactant and Stearic Acid in Mixed Monolayers. *Langmuir*, 26(12), 9342–9350.
- Lim, Y. S., Baharudin, N. B., & Ung, Y. W. (2019). Methyl Ester Sulfonate: A High-Performance Surfactant Capable of Reducing Builders Dosage in Detergents. *Journal of Surfactants and Detergents*, 22(3), 549–558.
- Lisunova, M. O., Lebovka, N. I., Melezhyk, O. V., & Boiko, Y. P. (2006). Stability of the aqueous suspensions of nanotubes in the presence of nonionic surfactant. *Journal of Colloid and Interface Science*, 299(2), 740–746.

- Ma, J.-G., Boyd, B. J., & Drummond, C. J. (2006). Positional Isomers of Linear Sodium Dodecyl Benzene Sulfonate: Solubility, Self-Assembly, and Air/Water Interfacial Activity. *Langmuir*, 22(21), 8646–8654.
- McConnell, H M. (1991). Structures and Transitions in Lipid Monolayers at the Air-Water Interface. *Annual Review of Physical Chemistry*, 42(1), 171–195.
- McConnell, Harden M., & De Koker, R. (1992). Note on the theory of the sizes and shapes of lipid domains in monolayers. *The Journal of Physical Chemistry*, 96(17), 7101–7103.
- Menger, F. M., & Littau, C. A. (1991). Gemini-surfactants: Synthesis and properties. *Journal of the American Chemical Society*, 113(4), 1451–1452.
- Menger, F. M., & Littau, C. A. (1993). Gemini surfactants: A new class of self-assembling molecules. *Journal of the American Chemical Society*, 115(22), 10083–10090.
- Menger, Fredric M. (2002, May 1). The structure of micelles [Research-article].
- Mivehi, L., Bordes, R., & Holmberg, K. (2011). Adsorption of Cationic Gemini Surfactants at Solid Surfaces Studied by QCM-D and SPR: Effect of the Rigidity of the Spacer. *Langmuir*, 27(12), 7549–7557.
- Mou, J., Yang, J., & Shao, Z. (1994). Tris(hydroxymethyl)aminomethane (C<sub>4</sub>H<sub>11</sub>NO<sub>3</sub>) Induced a Ripple Phase in Supported Unilamellar Phospholipid Bilayers. *Biochemistry*, 33(15), 4439–4443.
- Murray, B. S., & Nelson, P. V. (1996). A Novel Langmuir Trough for Equilibrium and Dynamic Measurements on Air–Water and Oil–Water Monolayers. *Langmuir*, 12(25), 5973–5976.
- Nandi, N., & Vollhardt, D. (2003). Effect of Molecular Chirality on the Morphology of Biomimetic Langmuir Monolayers. *Chemical Reviews*, 103(10), 4033–4076.
- Nessim, M. I., Zaky, M. T., & Deyab, M. A. (2018). Three new gemini ionic liquids: Synthesis, characterizations and anticorrosion applications. *Journal of Molecular Liquids*, 266, 703–710.
- Neta, N. S., Teixeira, J. A., & Rodrigues, L. R. (2015). Sugar Ester Surfactants: Enzymatic Synthesis and Applications in Food Industry. *Critical Reviews in Food Science and Nutrition*, 55(5), 595–610.
- Ojogun, V., Knutson, B. L., Vyas, S., & Lehmler, H.-J. (2010). Fluorophilicity of alkyl and polyfluoroalkyl nicotinic acid ester prodrugs. *Journal of Fluorine Chemistry*, 131(7), 784–790.
- Ojogun, V., Vyas, S. M., Lehmler, H.-J., & Knutson, B. L. (2010). Partitioning of homologous nicotinic acid ester prodrugs (nicotines) into dipalmitoylphosphatidylcholine (DPPC) membrane bilayers. *Colloids and Surfaces B: Biointerfaces*, 78(1), 75–84.

- Oremusová, J. (2012). Micellization of Alkyl Trimethyl Ammonium Bromides in Aqueous Solutions—Part 1: Critical Micelle Concentration (CMC) and Ionization Degree. *Tenside Surfactants Detergents*, 49(3), 231–240.
- Paige, M. F., & Eftaiha, A. F. (2017). Phase-separated surfactant monolayers: Exploiting immiscibility of fluorocarbons and hydrocarbons to pattern interfaces. *Advances in Colloid and Interface Science*, 248(Supplement C), 129–146.
- Pakiet, M., Tedim, J., Kowalczyk, I., & Brycki, B. (2019). Functionalised novel gemini surfactants as corrosion inhibitors for mild steel in 50 mM NaCl: Experimental and theoretical insights. *Colloids and Surfaces A: Physicochemical and Engineering Aspects*, 580, 123699.
- Petty, M. C., & Barlow, W. A. (1990). Film Deposition. In G. Roberts (Ed.), *Langmuir-Blodgett Films* (pp. 93–132). Boston, MA: Springer US.
- Petty, Michael C. (1996). Monolayers: Two-dimensional phases. In *Langmuir-Blodgett Films: An Introduction* (pp. 12–38). Cambridge: Cambridge University Press.
- Pinazo, A., Manresa, M. A., Marques, A. M., Bustelo, M., Espuny, M. J., & Pérez, L. (2016). Amino acid-based surfactants: New antimicrobial agents. *Advances in Colloid and Interface Science*, 228, 17–39.
- Pinazo, Aurora, Pons, R., Bustelo, M., Manresa, M. Á., Morán, C., Raluy, M., & Pérez, L. (2019). Gemini histidine based surfactants: Characterization; surface properties and biological activity. *Journal of Molecular Liquids*, 289, 111156.
- Qaqish, S. E., Urquhart, S. G., Lanke, U., Brunet, S. M. K., & Paige, M. F. (2009). Phase Separation of Palmitic Acid and Perfluorooctadecanoic Acid in Mixed Langmuir–Blodgett Monolayer Films. *Langmuir*, 25(13), 7401–7409.
- Quagliotto, P., Viscardi, G., Barolo, C., Barni, E., Bellinvia, S., Fiscaro, E., & Compari, C. (2003). Gemini Pyridinium Surfactants: Synthesis and Conductometric Study of a Novel Class of Amphiphiles. *The Journal of Organic Chemistry*, 68(20), 7651–7660.
- Rajput, S. M., Mondal, K., Kuddushi, M., Jain, M., Ray, D., Aswal, V. K., & Malek, N. I. (2020). Formation of hydrotropic drug/gemini surfactant based catanionic vesicles as efficient nano drug delivery vehicles. *Colloid and Interface Science Communications*, 37, 100273.
- Razafindralambo, H., Blecker, C., Mezdoor, S., Deroanne, C., Crowet, J.-M., Brasseur, R., Lins, L., & Paquot, M. (2009). Impacts of the Carbonyl Group Location of Ester Bond on Interfacial Properties

- of Sugar-Based Surfactants: Experimental and Computational Evidences. *The Journal of Physical Chemistry B*, 113(26), 8872–8877.
- Ren, C., Wang, F., Zhang, Z., Nie, H., Li, N., & Cui, M. (2015). Synthesis, surface activity and aggregation behavior of Gemini imidazolium surfactants 1,3-bis(3-alkylimidazolium-1-yl) propane bromide. *Colloids and Surfaces A: Physicochemical and Engineering Aspects*, 467, 1–8.
- Sah, B. K., & Kundu, S. (2020). Collapse of Langmuir monolayer formed by the mixture of short- and long-tailed fatty acid molecules. *Colloid and Interface Science Communications*, 36, 100261.
- Sar, P., Ghosh, A., Scarso, A., & Saha, B. (2019). Surfactant for better tomorrow: Applied aspect of surfactant aggregates from laboratory to industry. *Research on Chemical Intermediates*, 45(12), 6021–6041.
- Saxena, N., Pal, N., Dey, S., & Mandal, A. (2017). Characterizations of surfactant synthesized from palm oil and its application in enhanced oil recovery. *Journal of the Taiwan Institute of Chemical Engineers*, 81, 343–355.
- Scarzello, M., Klijn, J. E., Wagenaar, A., Stuart, M. C. A., Hulst, R., & Engberts, J. B. F. N. (2006). PH-Dependent Aggregation Properties of Mixtures of Sugar-Based Gemini Surfactants with Phospholipids and Single-Tailed Surfactants. *Langmuir*, 22(6), 2558–2568.
- Senthil Kumar, S. M., & Chandrasekara Pillai, K. (2006). Cetyltrimethyl ammonium bromide surfactant-assisted morphological and electrochemical changes in electrochemically prepared nanoclustered iron(III) hexacyanoferrate. *Journal of Electroanalytical Chemistry*, 589(1), 167–175.
- Seul, M., & Andelman, D. (1995). Domain Shapes and Patterns: The Phenomenology of Modulated Phases. *Science*, 267(5197), 476–483.
- Shaheen, A., Mir, A. W., Arif, R., & Wani, A. L. (2020). Synthesis, micellization behaviour and cytotoxic properties of imidazolium-based gemini surfactants. *Colloid and Interface Science Communications*, 36, 100257.
- Shakil Hussain, S. M., Kamal, M. S., & Murtaza, M. (2019). Effect of aromatic spacer groups and counterions on aqueous micellar and thermal properties of the synthesized quaternary ammonium gemini surfactants. *Journal of Molecular Liquids*, 296, 111837.
- Sharma, R., Kamal, A., Abdinejad, M., Mahajan, R. K., & Kraatz, H.-B. (2017a). Advances in the synthesis, molecular architectures and potential applications of gemini surfactants. *Advances in Colloid and Interface Science*, 248, 35–68.

- Sharma, R., Kamal, A., Abdinejad, M., Mahajan, R. K., & Kraatz, H.-B. (2017b). Advances in the synthesis, molecular architectures and potential applications of gemini surfactants. *Advances in Colloid and Interface Science*, 248, 35–68.
- Silva, S. G., Alves, C., Cardoso, A. M. S., Jurado, A. S., Pedroso de Lima, M. C., Vale, M. L. C., & Marques, E. F. (2013). Synthesis of Gemini Surfactants and Evaluation of Their Interfacial and Cytotoxic Properties: Exploring the Multifunctionality of Serine as Headgroup: Gemini Surfactants and Their Interfacial and Cytotoxic Properties. *European Journal of Organic Chemistry*, 2013(9), 1758–1769.
- Sorrenti, A., Illa, O., & Ortuño, R. M. (2013). Amphiphiles in aqueous solution: Well beyond a soap bubble. *Chemical Society Reviews*, 42(21), 8200–8219.
- Souza, F. D., Souza, B. S., Tondo, D. W., Leopoldino, E. C., Fiedler, H. D., & Nome, F. (2015). Imidazolium-Based Zwitterionic Surfactants: Characterization of Normal and Reverse Micelles and Stabilization of Nanoparticles. *Langmuir*, 31(12), 3587–3595.
- Stoer, A., & Tyrode, E. (2019). Interactions of Na<sup>+</sup> Cations with a Highly Charged Fatty Acid Langmuir Monolayer: Molecular Description of the Phase Transition. *The Journal of Physical Chemistry C*, 123(37), 23037–23048.
- Stine, K. J. (2012). Brewster Angle Microscopy. In *Supramolecular Chemistry*. American Cancer Society.
- Sung, W., Krem, S., & Kim, D. (2018). Binding of trivalent ions on fatty acid Langmuir monolayer: Fe<sup>3+</sup> versus La<sup>3+</sup>. *The Journal of Chemical Physics*, 149(16), 163304.
- Takehara, K., Oozono, Y., Oda, S., Isomura, K., & Taniguchi, H. (1990). Amphiphilic Compounds Having Heterocycles. Effects of the Structure of Heterocycle on the Behavior of the Monolayer at the Air–Water Interface. *Chemistry Letters*, 19(1), 5–8.
- Taylor, L. D. (1962). The Infrared Spectrum of Nicotinic Acid. *The Journal of Organic Chemistry*, 27(11), 4064–4065.
- TCI Chemical. (2022). Nicotinic Acid. Retrieved from <https://www.tcichemicals.com/US/en/p/N0082>
- Tehrani-Bagha, A. R., Singh, R. G., & Holmberg, K. (2012). Solubilization of two organic dyes by cationic ester-containing gemini surfactants. *Journal of Colloid and Interface Science*, 376(1), 112–118.
- Thompson, D. H. P., Barrette, W. C., & Hurst, J. K. (1987). One-electron reduction of dihexadecyl phosphate vesicle-bound viologens by dithionite ion. *Journal of the American Chemical Society*, 109(7), 2003–2009.

- Tu, S., Jiang, X., Zhou, L., Yin, W., Wang, H., Duan, M., Liu, P., & Jiang, X. (2012). Study of the interaction of gemini surfactant NAE12-4-12 with bovine serum albumin. *Journal of Luminescence*, *132*(2), 381–385.
- Verdía, P., González, E. J., Rodríguez-Cabo, B., & Tojo, E. (2011). Synthesis and characterization of new polysubstituted pyridinium-based ionic liquids: Application as solvents on desulfurization of fuel oils. *Green Chemistry*, *13*(10), 2768–2776.
- Vermeulen, L. A., & Thompson, M. E. (1992). Stable photoinduced charge separation in layered viologen compounds. *Nature*, *358*(6388), 656–658.
- Voigtländer, B. (2019). *Atomic Force Microscopy* (2ed ed.). Springer. Retrieved from <https://link.springer.com/book/10.1007/978-3-030-13654-3>
- Wang, C., Jiang, X., Zhou, L., Xia, G., Chen, Z., Duan, M., & Jiang, X. (2013). The preparation of organo-bentonite by a new gemini and its monomer surfactants and the application in MO removal: A comparative study. *Chemical Engineering Journal*, *219*, 469–477.
- Wang, L., Liu, J., Huo, S., Deng, Q., Yan, T., Ding, L., Zhang, C., Meng, L., & Lu, Q. (2014). Synthesis and Surface Properties of Novel Gemini Imidazolium Surfactants. *Journal of Surfactants and Detergents*, *17*(6), 1107–1116.
- Wang, Ya, Jiang, X., Zhou, L., Yang, L., Xia, G., Chen, Z., & Duan, M. (2013). Synthesis and binding with BSA of a new gemini surfactant. *Colloids and Surfaces A: Physicochemical and Engineering Aspects*, *436*, 1159–1169.
- Wang, Yujie, Marques, E. F., & Pereira, C. M. (2008). Monolayers of gemini surfactants and their catanionic mixtures with sodium dodecyl sulfate at the air–water interface: Chain length and composition effects. *Thin Solid Films*, *516*(21), 7458–7466.
- Weidemann, G., Brezesinski, G., Vollhardt, D., Bringezu, F., de Meijere, K., & Möhwald, H. (1998). Comparing Molecular Packing and Textures of Langmuir Monolayers of Fatty Acids and Their Methyl and Ethyl Esters. *The Journal of Physical Chemistry B*, *102*(1), 148–153.
- Yoshimura, T., Ishihara, K., & Esumi, K. (2005). Sugar-Based Gemini Surfactants with Peptide Bonds Synthesis, Adsorption, Micellization, and Biodegradability. *Langmuir*, *21*(23), 10409–10415.
- Zhou, L., Jiang, X., Li, Y., Chen, Z., & Hu, X. (2007). Synthesis and Properties of a Novel Class of Gemini Pyridinium Surfactants. *Langmuir*, *23*(23), 11404–11408.

- Zhou, M., Liu, H. L., Yang, H. F., Liu, X. L., Zhang, Z. R., & Hu, Y. (2006). Spontaneous Crystallization at the Air–Water Interface: An Unusual Feature of Gemini Surfactant with a Rigid Spacer. *Langmuir*, 22(26), 10877–10879.
- Ziyatdinova, G., Ziganshina, E., & Budnikov, H. (2012). Surfactant media for constant-current coulometry. Application for the determination of antioxidants in pharmaceuticals. *Analytica Chimica Acta*, 744, 23–28.
- Zuo, Y. Y., Veldhuizen, R. A. W., Neumann, A. W., Petersen, N. O., & Possmayer, F. (2008). Current perspectives in pulmonary surfactant—Inhibition, enhancement and evaluation. *Biochimica et Biophysica Acta (BBA) - Biomembranes*, 1778(10), 1947–1977.

## Appendix

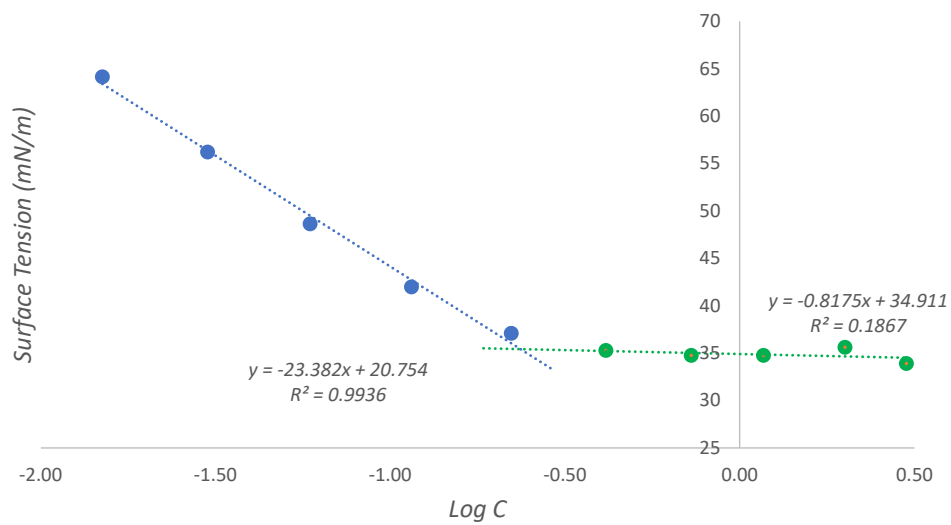


**Figure A.1.** Surface tension ( $\gamma$ , mN/m) versus log C of Et-NA<sup>+</sup>-C<sub>16</sub>•Br. The CMC was determined at the intersection of the linear regression fits. The applied concentrations were in the mM range.

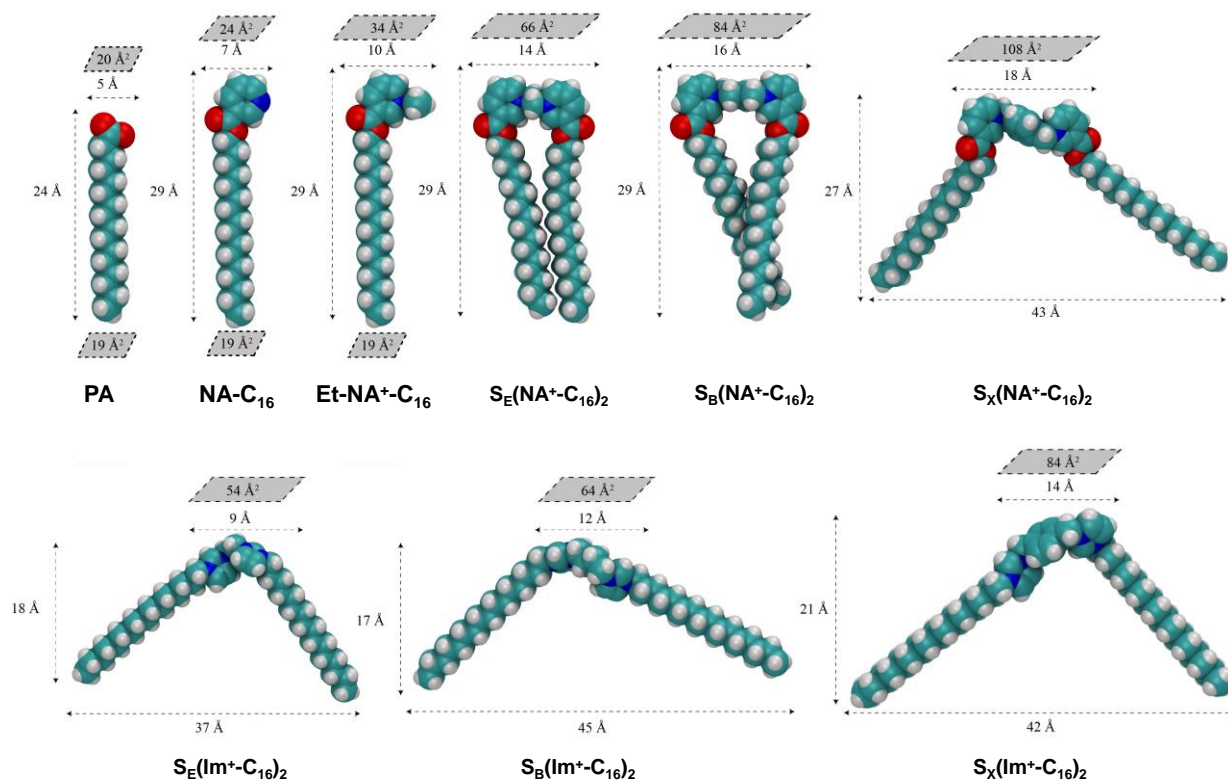


**Figure A.2.** DFT-optimized structures (in the gas phase) of PA, NA and Im<sup>+</sup>-based conventional and gemini surfactants including molecular height, length (Å) and cross-sectional area (Å<sup>2</sup>).

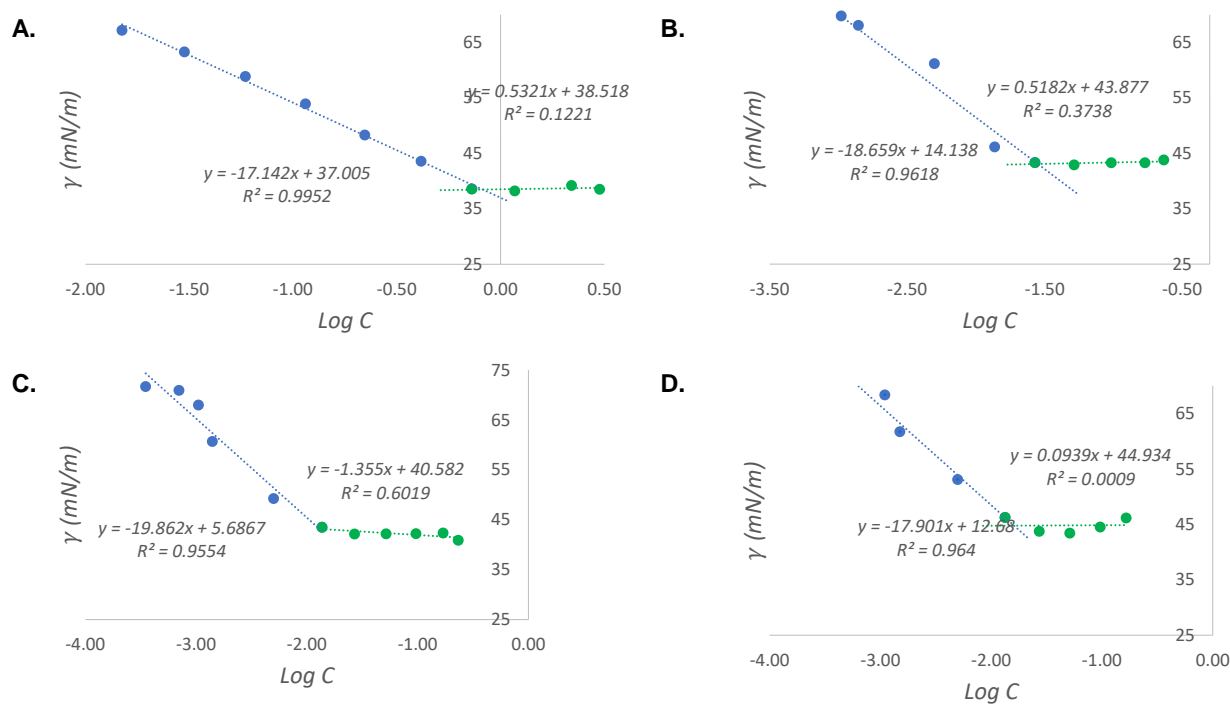


**Figure A.3.** Surface tension ( $\gamma$ , mN/m) versus  $\log C$  of: **A.**  $\text{Im}^+-\text{C}_{16}\cdot\text{Cl}$ , **B.**  $\text{S}_E(\text{Im}^+-\text{C}_{16})_2\cdot 2\text{Br}$ , **C.**  $\text{S}_B(\text{Im}^+-\text{C}_{16})_2\cdot 2\text{Br}$  and **D.**  $\text{S}_X(\text{Im}^+-\text{C}_{16})_2\cdot 2\text{Br}$ . The CMC was determined at the intersection of the linear regression fits. The applied concentrations were in the mM range.

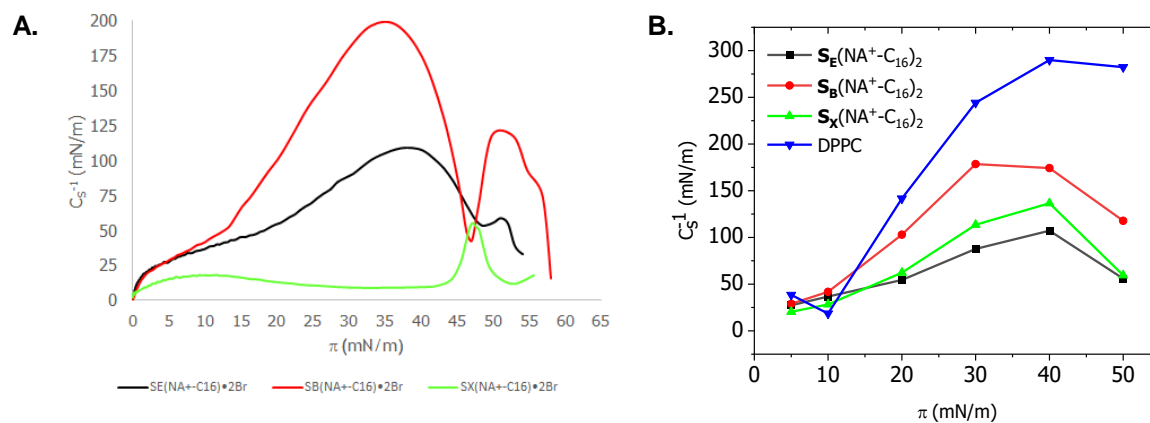


**Figure A.4.** **A.** Isothermal compressibility plots of  $\text{S}(\text{NA}^+-\text{C}_{16})_2\cdot 2\text{Br}$ , **B.** The isothermal compressional moduli of  $\text{S}(\text{NA}^+-\text{C}_{16})_2\cdot 2\text{Br}$  as a function of surface pressure in comparison with DPPC.

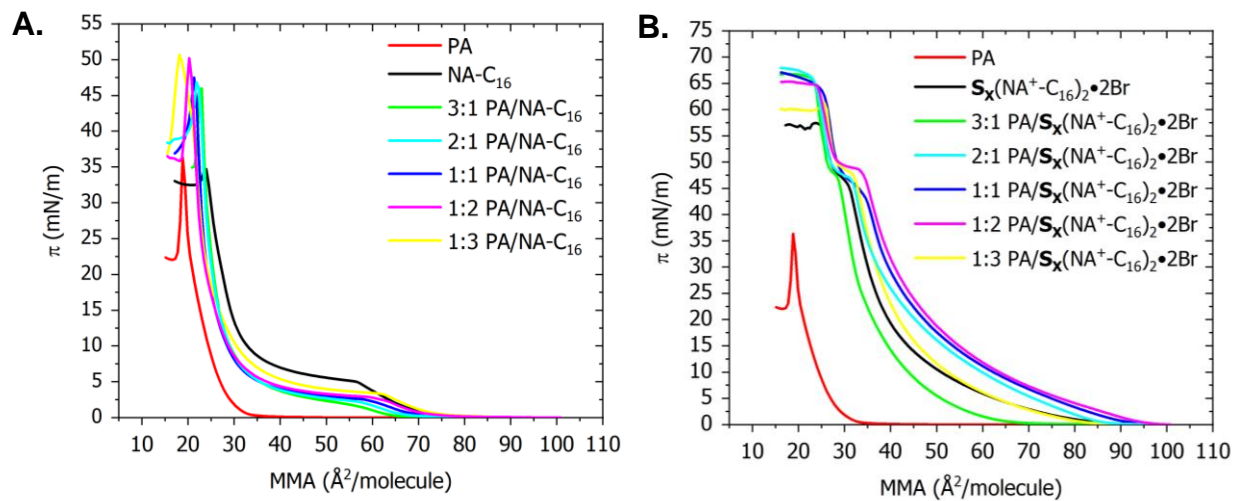


**Figure A.5.**  $\pi$ -A isotherms of: **A.** PA/NA-C<sub>16</sub>; **B.** PA/S<sub>x</sub>(NA<sup>+</sup>-C<sub>16</sub>)<sub>2</sub>•2Br mixed monolayers measured on Milli-Q water subphase at 25 °C